

INTERACTION OF FEMTOSECOND X-RAY PULSES WITH PERIODICAL MULTILAYER STRUCTURES

Dissertation

zur Erlangung des Grades eines Doktors
der Naturwissenschaften

vorgelegt von

D.P.

Dmitriy Ksenzov

geb. am 19.12.1977 in Zhodino (Belarus)

eingereicht beim Fachbereich -7, Physik

der Universität Siegen

Siegen 2010

1. Gutachter: Prof. Dr. Ullrich Pietsch
2. Gutachter: Prof. Dr. Ilya Feranchuk

Disputation:

Prüfer:

Abstract

The VUV Free Electron Laser FLASH operates in soft X-ray range and produces high-intensive pulse trains with few tens femtoseconds duration. The transversely fully coherent beam will open new experiments in solid state physics which can not be studied with present radiation sources.

The study of the time dependent response of the multilayer to the X-ray pulse can provide insights into the process of interaction of highly intense FEL radiation with matter. To test the influence of electron excitation on the optical properties of boron carbide, the refractive index of B_4C was measured near B K-edge by energy-resolved photon-in-photon-out method probing a Bragg reflection from periodical multilayers. The measured data clearly show that the variation of the fine structure of the K-absorption edges due to the chemical nature of the absorber element.

The knowledge obtained from experiments with continuous radiation was used to design the respective experiments with pulse from the FEL. In my thesis, it is proposed that the geometrical setup, where the incident pulse arrives from the FEL under the angle close to the 1st order ML Bragg peak, provides the most valuable information. Preliminary simulation considering form factors of neutral and ionized boron showed that due to ionization, pronounced changes in the reflectivity curve are expected. The proposed scheme can be the powerful tool to study the various processes within the electronic sub-system of the FEL pulse interaction with matter. This type of investigations gives a deep understanding of the nature of the electronic excitation and the recombination at the femtosecond scale.

Der VUV Freie-Elektronenlaser FLASH arbeitet im weichen Röntgenbereich und produziert Wellenpulse mit zum Teil weniger als 10 Femtosekunden Dauer. Der transversal vollständig kohärente Strahl eröffnet neue Experimente in der Festkörperphysik, die mit bis dato verfügbaren Strahlungsquellen nicht durchgeführt werden konnten.

Die Untersuchung der zeitabhängigen Antwort eines Multilayers auf einen Röntgenpuls gibt Aufschluss über die Interaktion der sehr intensiven FEL Strahlung mit der Materie. Dazu wurde der Brechungsindex von B_4C in der Nähe der K-Absorptionskante von Bor mit Hilfe einer energieaufgelösten photon-in-photon-out Methode gemessen. Dabei wurde die Braggbeugung eines periodischen Multilayers ausnutzt, um den Einfluss der Elektronenanregung auf die optischen Eigenschaften von B_4C zu untersuchen. Die gemessenen Daten zeigen eine klare Variation der Feinstruktur der K-Absorptionskante, die die unterschiedlichen chemischen Eigenschaften des Absorberelements Bor in verschiedenen Multilayern widerspiegelt.

Das Wissen aus dem Experiment mit kontinuierlicher Strahlung wurde genutzt, um ein entsprechendes Experiment mit dem FEL-Pulsen zu konzipieren. In meiner Arbeit schlage ich einen geometrischen Setup vor, bei welchem der einfallende Puls des FEL unter einem festen Winkel in der Nähe des Braggpeaks erster Ordnung des gekrümmten Multilayers einfällt, und die gestreute Intensität des gesamten Braggpeaks gleichzeitig gemessen werden kann. Vorläufige Simulationen, die Formfaktoren von neutralem und ionisiertem Bor berücksichtigen, zeigen, dass durch Ionisation klare Änderungen in der Reflektivitätskurve erwartet werden können. Das vorgeschlagene Schema kann ein kraftvolles Instrument sein, um verschiedene Prozesse innerhalb des elektronischen sub-Systems der Interaktion des FEL-Pulses mit Materie zu studieren. Diese Art von Untersuchung liefert ein tiefes Verständnis der Natur der elektronischen Anregung und der Rekombination auf der Femtosekundenskala.

Table of contents

Abstract	3
Motivation	6
1. Introduction	8
1.1. Synchrotron radiation sources.....	8
1.2. X-ray free electron lasers.....	11
2. FEL radiation properties	17
2.1. Statistical analysis of the chaotic optical field from a SASE FEL.....	17
2.1.1. <i>Analysis of the radiation properties in the frequency domain</i>	20
2.1.2. <i>Analysis of the radiation properties in the time domain</i>	22
2.2. First experimental results at X-ray free-electron laser.....	23
2.2.1. <i>Operation of a VUV FEL at 32 nm wavelength</i>	23
2.2.2. <i>Operation of a VUV FEL at 13.7 nm wavelength</i>	25
2.2.3. <i>Operation of a VUV FEL at 6.5 nm wavelength</i>	27
3. The present theory of the interaction soft X-ray radiation with medium	29
3.1. X-ray interactions and wave equations.....	29
3.2. Linear-optics reflection theory.....	32
3.2.1. <i>Time-dependent power spectrum</i>	36
3.2.2. <i>Bandwidth limited: Gaussian-shaped pulse</i>	37
3.3. Ultrafast processes.....	40
3.3.1. <i>Single atom scattering properties</i>	40
3.3.2. <i>Optical properties of solids</i>	41
4. Different approaches of X-ray reflectivity from multilayers	42
4.1. Methods of calculation of reflectivity.....	42
4.1.1. <i>Parratt's recursive method</i>	43
4.1.2. <i>Transfer matrix method</i>	46
4.1.3. <i>Finite Difference Time Domain (FDTD) method</i>	48
4.1.4. <i>Slowly varying amplitude approximation</i>	50
4.1.5. <i>Analytical method by eigenwaves</i>	52
4.2. Approach for Sliced Multilayer Gratings.....	53
5. Optical properties of boron carbide	57
5.1. Boron carbide (B ₄ C).....	57
5.1.1. <i>Structural properties</i>	59
5.1.2. <i>Energy-level diagrams for establishing the K-shell binding energy</i>	60

5.2. Near edge X-ray absorption.....	63
5.3. Refractive index of boron carbide.....	67
6. Resonant soft X-ray reflectivity of multilayers based on B₄C material.....	69
6.1. Mirror fabrication.....	69
6.2. Theoretical background.....	70
6.3. Experimental results.....	75
6.3.1. <i>Structural properties of multilayers</i>	75
6.3.2. <i>Results of soft X-ray measurements</i>	77
6.3.2.1. <i>Boron K-edge</i>	78
6.3.2.2. <i>Carbon K-edge</i>	86
6.3.2.3. <i>Nitrogen K-edge</i>	87
7. Reflection of Soft X-ray FEL pulses by periodical multilayers.....	90
7.1. Basic formalism.....	90
7.2. Numerical simulation of fs-pulse responses from multilayers.....	91
7.3. Space-time transformation.....	98
7.4. Reconstruction of energy distribution of incident pulse.....	100
7.5. Processes of the ionization: influence of ionization.....	104
7.5.1. <i>Calculation of Anomalous Scattering for Ions and Atoms</i>	105
7.5.2. <i>Temporal evolution of the optical properties of boron carbide</i>	108
7.6. Possible experimental setup of the experiment at FLASH.....	108
Summary.....	111
Appendix A Kramers-Kronig relations.....	114
Appendix B Fourier transform.....	115
Appendix C Z-transform.....	116
Appendix D Slater-type orbital expansions and expectation values boron.....	117
References.....	119
List of Publications.....	127
Acknowledgments.....	128
Curriculum vitae.....	129
Eidesstattliche Erklärung.....	130

Motivation

In 2014 the first light from European X-ray Free Electron Laser (XFEL) will be available for experiments. Right now the Linac Coherent Light Source (LCLS) at Stanford Linear Accelerator Center (SLAC), Stanford, USA has produced first light and has reached saturation at a wavelength of 1.5 Å. The advances in radiation characteristics, such as an extremely high power density of 10^{12} X-ray photons per pulse, a transversely fully coherent beam and a pulse duration of about 100 femtoseconds, open a new field for experiments on fs- time scale such as multiphoton processes in atoms, molecules and solids and the energy transfer between electrons and lattice which cannot be studied with present X-ray sources.

At femtosecond timescale, the main process of interaction consists of the massive excitation of electrons from the ground state into various excited states or vacuum. At the same time scale, the various recombination processes take place as well. On the other hand, the electron-phonon interaction takes place on the picosecond time scale and has no importance for the interpretation of scattering process. Therefore, the femtosecond FEL radiation mainly interacts with the fixed lattice (frozen atomic positions) and the scattering process is dominated by the time dependent population of electronic states which cannot be described in terms of current theories of X-ray diffraction.

Although recent experiments at VUV-FEL FLASH have demonstrated the feasibility of FELs for such kind of experiments, the major problems with the interpretation or theoretic prediction are unsolved or at least untouched. From first experiments with the FLASH one knows that direct illumination of a crystalline solid with a FEL pulse results in complete destruction of the material. On the other hand, there are interesting scientific questions in solid state physics and crystallography which can be elucidated by fs-diffraction only: for example, the investigation of the detailed temporal structure of the electron-phonon interaction in solids and the study of charge density of excited electronic states with short life time.

As long as the hard X-ray FEL sources are not available such type of interactions can be studied using quasi 1D crystals, i.e. short period multilayers (MLs) at VUV-FEL. Multilayers structures made for the use in the wavelength range near boron K-edge ($\sim 188\text{eV}$) are of great interest for X-ray fluorescence analysis of boron content doped semiconductors for plasma diagnostics, astronomy and lithography. Moreover, MLs composed by a metal and a low Z element like boron are used as optical elements in both the soft X-ray range as well as at higher photon energies on 3rd generation synchrotron beamlines. This also holds for application at FELs like FLASH. The shape and total scattering power of the fundamental Bragg reflection of the ML are determined by the numbers of periods and the differences in the optical refraction

indexes of the composed layer materials. For these Me/B_4C multilayers structures, the different ionic states of boron can be effectively observed by reflectivity measurements close to the K-edge.

The aim of my thesis is the experimental and theoretical analysis of X-ray diffraction patterns arising due to the interaction process of fs- FEL pulses with a crystalline matter, and the design of an experimental scheme for the FLASH experiment to test the general interaction phenomena of ultra short and high intense FEL pulses with solid matter using periodical multilayers structures.

The first part of the manuscript (Chapter 1) describes the main types of high-intensity sources of X-ray radiation. Based on the theory of X-ray FEL, the temporal and special properties of FEL radiation are described in Chapter 2. Using the obtained expressions we can modulate the incident single FEL pulse for simulation in following chapters. The theory of interaction of short pulses with a medium is developed in Chapter 3. Because of the limited information about the scattering properties of multilayers during the interaction with the short and intense pulses, at the first stage we probed the scattering properties of MLs using continuous VUV radiation. The different approaches of X-ray reflectivity from the multilayers are described in Chapter 4. For our investigations we used the multilayers containing two light elements such as boron and carbon. The structural and optical properties of boron carbide (B_4C) are presented in Chapter 5. To test the influence of electron excitation on the optical properties, the scattering properties of thin multilayers are studied using the continuous soft X-ray radiation at BESSY and presented in Chapter 6. Here we show that the energy-resolved reflectivity experiment to determine the degree of electronic excitations by scanning energy near the boron and carbon K-edges. Based on this knowledge, in Chapter 7 I propose the approach which enables to study the interaction of the FEL pulses with a periodical multilayer. The approach for the possible experimental realization of space-time transformation; the reconstruction of the energy distribution of the incident pulse; the influence of high intensity and the expected modifications of optical parameters and the reflectivity under the influence of electron excitation, are described. Finally, the scheme at FLASH experiments with multilayers to analyze the effects which are linked with the high intensity of FEL radiation is proposed.

Chapter 1

Introduction

The use of electromagnetic waves to study physical phenomena of crystalline matter and structure to properties-relations dates back to the beginning of the 20th century. There were a lot of achievements along the way, from atomic spectroscopy to X-ray crystallography. The various investigations required ever more brilliant sources to investigate the framework and underpinnings of the complex processes at the molecular and atomic levels on ultra short time scales. Currently, there is an intense drive to realize a radiation source capable to produce high peak power X-ray photons with the Angstrom wavelengths and pulses as short as tens of femtoseconds.

The range of photon energies comprised between 30 eV and 600 eV correspond to the wavelengths extending from about 2 nm to 40 nm is well-known as extreme ultraviolet (EUV)/soft X-rays or XUV radiation. This region is dominated by a large number of atomic resonances, leading to strong absorption of radiation and the wavelengths in soft x-ray range are too large to make it applicable for X-ray diffraction at natural crystal.

1.1 Synchrotron radiation sources

Synchrotron radiation spans over a wide spectral range, which runs continuously from the infrared to the hard X-rays, and the achieved *intensity* and *brilliance* (density of photons in phase space) are indeed high. This is particularly interesting for X-ray spectroscopy, because there is no other traditional source, which offers the same spectral properties. Polarization (linear in the plane of the electron orbit and circular above and below this plane) and temporal structure (due to the fact that the beam is not continuous but bunched) are two additional characteristics of the radiation emitted by electrons circulating within the storage ring. Furthermore the small diameters of the electron beam leads to a very small source size of the X-ray beam and the divergence of the emitted light.

According to the classical theory of electrodynamics, when a particle with an electric charge is accelerated, it emits electromagnetic wave [1]. Synchrotron radiation is generated when the relativistic electrons (or positrons) are accelerated in a magnetic field. In the storage ring of a synchrotron radiation facility, when charged particles are moving at relativistic velocities, this emission is quite particular. The radiation is concentrated in a narrow cone along the tangential direction to the particle trajectory. There are three types of magnetic structures commonly used to produce synchrotron radiation: *bending magnets*, *undulators* and *wigglers*.

When electrons are accelerated parallel to the direction of their motion, the radiation power is negligible. But the acceleration is perpendicular to the direction of motion in bending magnets can lead to a huge radiation power. Thus a bending magnet is a source of synchrotron radiation. The emitted power at a given bending radius depends on the parameter $\gamma=E/(mc^2)$ to the power of four. Due to low mass, only electrons (or positrons) are used for the production of synchrotron radiation, at typically $\gamma=10^4$. The emission is strongly peaked in the forward direction, i.e. tangential to the orbit (see Fig.1.1) with opening angle of the order γ^{-1} (see [2] for details). However, this single-electron emission angle must be convoluted with the angular distribution of electrons within one bunch. *The first generation of synchrotron radiation* sources consisted of machines built for particle physics experiments and the emission from the bending magnets was used in the so-called “parasitic mode”.

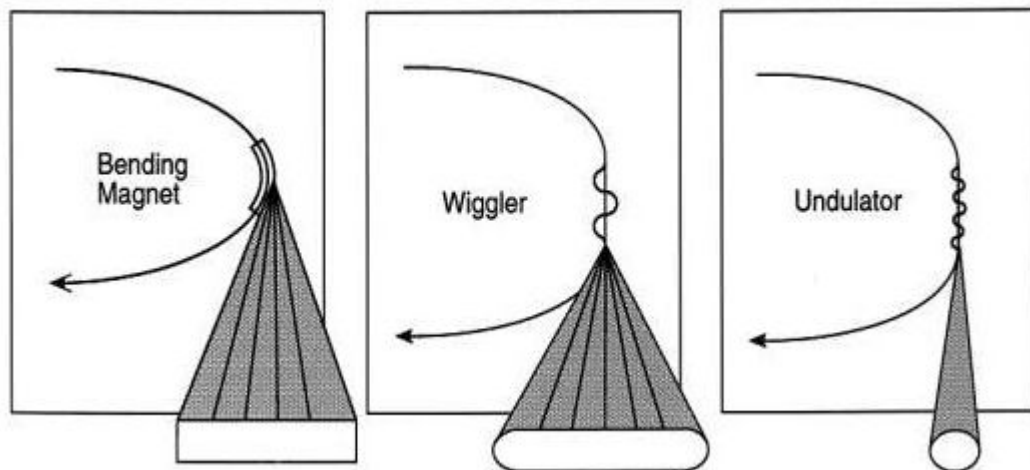


Fig. 1.1 Schematic of the three magnetic structures: bending magnet, wiggler, and undulator emission used for synchrotron light generation.

Historically, synchrotron radiation was observed as a loss of energy in the electron storage rings. Logically, the first synchrotron radiation sources for general scientific use were simple parasitic beam ports utilizing otherwise lost radiation at existing storage rings. Over the time, the sources have been constructed for a dedicated use as synchrotron radiation facilities (*second generation facilities*), for example, the 380 MeV SOR ring at the University of Tokyo that was started operation in the mid-1970. In general case these types of synchrotron sources have a large number of beam lines and experimental stations, where the photons are delivered from the bending magnets and serve many users simultaneous. In the second generation, special magnetic structures, called wigglers and undulates, were inserted into the storage ring. The generic name for both types is “insertion device” and both consist of alternatively poled magnets in a periodic array with a given period λ_u (*the undulator wavelength*).

Usually, scientists never have enough photons for their experiments and an asked for more intense beam. Wigglers are a neat way to increase the intensity of synchrotron radiation by

lining up the series of bending magnets which enhances the intensity simply by the number of magnet poles. The generated spectrum is that of a corresponding bending magnet. In order to add up the intensity of individual emission cones, the dipoles are arranged with alternating polarity so that the electrons are essentially move straight except for small “wiggles” where the radiation is emitted. The emission cones overlap and the intensity adds up. The advantage of a wiggler is that it emits intense radiation over a wide spectral range, very much like a bending magnet. At the same time, this is its major disadvantage because a lot of scientific experiments usually need only a very narrow range of wavelengths and therefore most of the wiggler radiation power remains unused leading to unwanted heat production within the optical devices.

Most modern machines preferentially use so-called undulators instead of wigglers. *Undulators* are the most powerful generators of synchrotron radiation at storage rings. Like wigglers, they consist of periodic arrangements of the dipole magnets generating an alternating static relatively weak magnetic field which deflects the electron beam sinusoidally. The weak magnetic fields cause the amplitude of this undulation to be small. Hence, the resultant radiation cone is narrow. In combination with a tightly confined electron beam, this leads to the radiation with small angular divergence and a relatively narrow spectral width, properties that we generally associate with the coherence properties of lasers.

The newest synchrotron facilities (*3rd generation facilities*) are composed of many straight sections (see Fig. 1.2) specially optimized to produce high brightness undulator and wiggler radiation. The lattice structures and the design philosophy of 3rd-generation X-ray sources were those introduced by Green and Chasman [3]. The use of the sufficiently high electron energy allows the undulator to deliver high brightness radiation at wavelengths at less than 1Å. In order to take all advantages of undulator's features, the third generation of synchrotron light sources (since the 90's and still operational) was designed with the long dedicated straight sections to incorporate these devices. Specific care was taken to optimize the synchrotron magnetic lattice in order to increase the brightness.

The production of high-energy photons is provided by machines with quite high electron beam energies as the ESRF (Grenoble), APS (Argonne) and SPring-8 (Japan). Sources are optimized to provide lower photon energies wavelengths at VUV-range to operate at electron-beam energies of several GeV. This is, for example, in the case of Elettra (Trieste), ALS (Berkeley) and BESSY II (Berlin). Most third-generation sources fall into two broad categories: (i) few GeV rings with 100 to 200 meters circumference designed primarily for the spectral region below about 2 keV (VUV and soft X-rays) and (ii) 6-8 GeV rings with a circumference of 800-1500 meters, designed primarily for the harder X-rays, above about 2 keV.

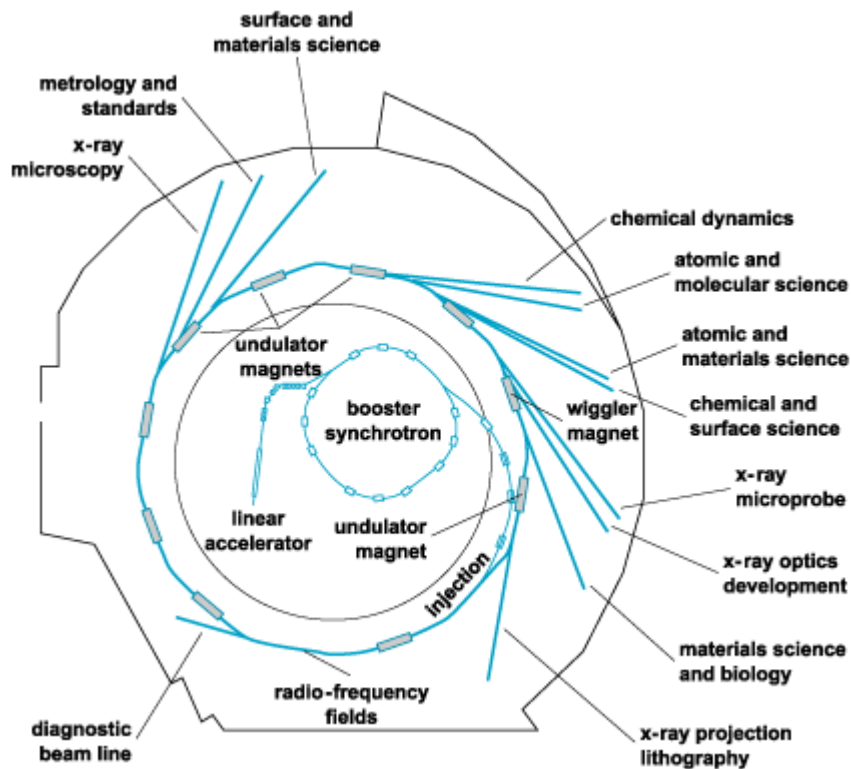


Fig. 1.2 Layout of the 1.5-GeV Advanced Light Source at Lawrence Berkeley National Laboratory, a low-energy, 3rd generation synchrotron radiation source.

The race to develop a new generation of synchrotron radiation sources with vastly enhanced performance has already begun, even as the third-generation facilities enter their prime, which takes us past the present into the future; namely, to *the fourth generation* [4-6]. The candidate with the best scientific case for a fourth-generation source is the hard X-ray (wavelength less than 1Å) FEL based on a very long undulator in a high-energy electron linear accelerator. Such a device would have a peak brightness many orders of magnitude beyond that of the third- generation sources, as well as the pulse lengths of 100 fs or shorter, and it will be fully coherent. Research and development on the many technical challenges that must be overcome are well under way at many laboratories around the world.

In the United States, effort is centering on the multi-institutional "Linac Coherent Light Source" (LCLS) project to use 15-GeV electrons from the SLAC linac as a source for a 1.5-Å FEL, which will lay the foundation for the later sub-angstrom X-ray FEL. In Europe, together with international partners, DESY is constructing a European XFEL facility. Electrons will be accelerated to energy of 17.5 GeV by a 2.1 km long superconducting linear accelerator. The European XFEL will provide radiation at 1.0-Å (12.4 keV) light.

1.2 Free Electron Lasers

In the middle of the 1970s Jonh Madey and his colleagues constructed the first FEL operating in the infrared wavelength range [7]. An externally applied electromagnetic wave which propagates parallel to the electrons will be amplified and, finally, the laser-like radiation

will be produced. Since the electrons are not bounded to any medium, Madey called such a device *free-electron laser* (FEL). As already mentioned above for synchrotron sources, FEL converts the kinetic energy of the relativistic electron beam into electromagnetic radiation [8-10]. When the electrons interact with the undulator field, their trajectories altered accordingly, and photons are emitted at a specific wavelength. The wavelength is defined by the energy of the electron beam and the physical parameters of the undulator:

$$\lambda = \frac{\lambda_u}{2\gamma^2} \left(1 + \frac{K^2}{2} \right). \quad (1.1)$$

Here, λ is the radiated wavelength; λ_u is the period of the undulator magnetic field, and K is the normalized magnetic deflection strength. This equation is strictly valid for the emission along the axis of undulator. If we observe the emission at an angle θ slightly off-axis, the wavelength charges with respect to the on-axis value.

There are a number of advantages that the FEL possesses compared to that of traditional lasers and other radiation sources. The radiated wavelength λ is a function of the electron beam energy. Hence, the FEL is a tunable source of radiation whereas the molecular lasers can emit only coherently at the specific wavelengths, which depend on the excitation levels. Indeed, the FEL is able to operate in the X-ray region of the electromagnetic spectrum. Also, since the source of the FEL is the electron beam in a vacuum, the FEL can operate at high power with no damage to the lasing medium in contrast to the traditional molecular lasers, where the maximum power is limited to the damage threshold of the medium [8-10].

The emission per period is broadband, however, since the electrons emit periodically over a long time interval, certain frequencies are enhanced through period-to-period interference effects. The wavelength of the enhanced radiation depends on the electron energy and the parameters of the employed magnetic structure. As the electrons travel collinearly with an electromagnetic wave, a component of the electron velocity is in the direction along the transverse electric field of the wave, which allows energy to exchange. As the energy is transferred from the electrons to the wave, the radiation field is amplified and the electrons are slowed down. The distribution of electron energy as a function of longitudinal position in the bunch is also modulated by the interaction of an electron with the radiation. As a result, the electrons tend to physically group into bunches, separated by the radiation wavelength. The radiation is greatly enhanced further by this process, which is called *microbunching*. In case when all the electrons are coherently emitting in phase, the maximal bunching is achieved and the FEL reaches saturation. At this point the energy gain of the field is not significantly enhanced by additional modulation. The closed loop process (oscillation, field enhancement, modulation)

is the basic operating mechanism of the free electron laser. The converse scenario is also a field under active study; if the energy is transferred from the electromagnetic wave to the electrons, the electrons are accelerated in a device referred to as *the inverse free electron laser* [11].

The X-ray FEL will not only extend the today's light sources by increasing the brilliance of radiation (Fig.1.3). Its sub-picosecond light pulses of very narrow bandwidth will enable scientists to perform experiments which have never been possible before. For example, the diffraction patterns of single molecules can be produced with a single light pulse from the X-ray FEL. This is of special interest in biology where molecules can often only be crystallized on a very small scale or even not at all. To study the dynamical processes on an atomic scale, up to 4000 light pulses with an rms length of 80 fs each can be produced within a bunch train 800 μ s long. The radiation wavelength will be tunable in the range of 0.1 - 6 nm.

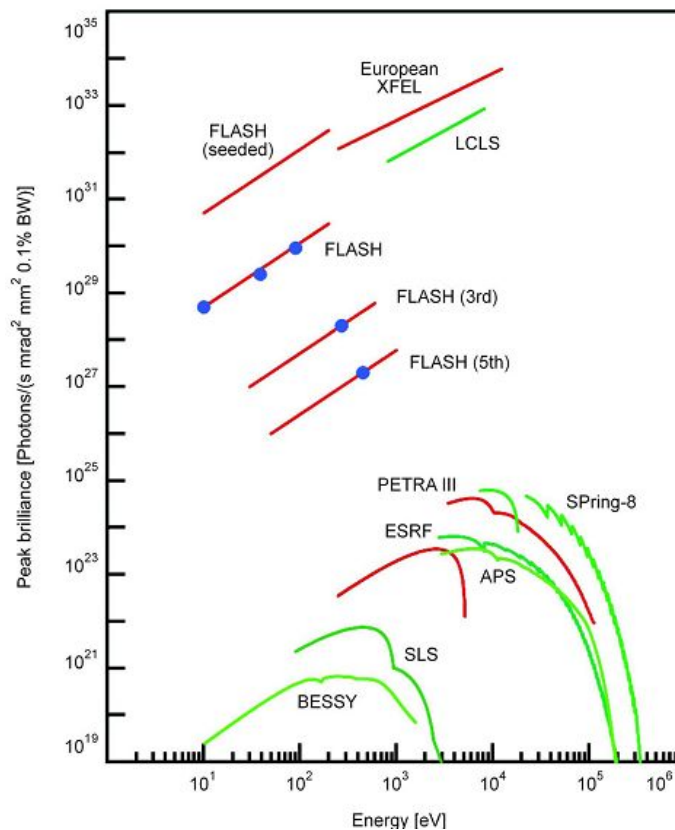


Fig. 1.3 The peak brilliance of the FELs will surpass today's synchrotron radiation sources by several orders of magnitude over a wide range of photon energies. (taken from [12])

The European X-ray FEL includes a photo-injector which produces electron bunches with a charge of 1nC. It will be located at DESY in Hamburg. The linac accelerates the electrons to energies up to 20 GeV. The experimental hall will be located about 3.3 km to the north-west of the DESY. In 2014 the first radiation is expected to be delivered for the experiments [12]. The X-ray FEL will not only extend today's light sources by increasing the brilliance of the radiation.

The FEL in Hamburg (FLASH) at DESY is a FEL based on the SASE principle and can deliver a very intense light in the wavelength range from 6.5 to 47 nm in the first harmonic [13-14]. Installation of further accelerating modules has been done to achieve higher electron energies and thereby achieve even shorter wavelengths as 6.5 nm in the first harmonic, providing a uniquely intense, short-pulsed radiation. Peak and average brilliance of this new FEL user facility exceeds both modern synchrotron facilities and laser plasma sources by many orders of magnitude. The soft X-ray output possesses unprecedented flux of about 10^{13} photons per pulse with durations of 10–50 fs, and hence, combined with appropriate focusing optics, the peak irradiance levels of more than 10^{16} Wcm⁻² can be achieved [15].

Since the first experiments in 2005, the soft X-ray FEL FLASH has reached the status of routine operation. The stability and reliability of the FEL have been significantly increased and FLASH recently achieved a world record peak and average coherent power at a wavelength of 13.7 nm in the fundamental [14]. The corresponding fifth harmonic wavelength (~2.7 nm) at power levels of about 0.03% is shorter than for any radiation produced so far by plasma-based X-ray lasers at a comparable levels of intensity and lies well within the ‘water window’, where the biological systems can be imaged and analyzed *in vitro*. Table 1.1 summarizes the performance of FLASH.

Table 1.1. Performance of FLASH.

Parameter of FLASH	
Wavelength range fundamental	6.9–47 nm
Higher harmonics	
3 rd	~2.3 nm
5 rd	~1.4 nm
Pulse energy average	10–50 μJ
Peak power	several GW
Pulse duration (full-width at half-maximum FWHM)	10–50 fs
Spectral width (FWHM)	0.5–1%
Spot size at the undulator exit (FWHM)	~160 μm
Angular divergence (FWHM)	90±10 μrad
Peak brilliance (photons s ⁻¹ mrad ⁻² mm ⁻² per 0.1%bw)	10 ²⁹ –10 ³⁰

The FLASH experimental hall is presently equipped with five experimental stations (Fig. 1.4). A variety of experiments in basic and applied research of multiple scientific fields, from life science, chemistry to physics are scheduled including pump-probe experiments. The experimental stations at the beamlines BL1, BL2 and BL3 utilize the direct FEL pulses. When entering the experimental hall, the FEL beam has a width of about 3 - 5 mm. To focus the beam, BL1 is equipped with a toroidal mirror, while the ellipsoidal mirrors are used at BL2 and BL3. Most users need highly focused and extremely bright FEL pulses, for example, for experiments

in plasma physics, cluster science, and materials research. The mirrors at BL1 and BL2 focus the beam down to spots of approximately 100 μm and 20 μm , respectively. At BL3 the beam can be focused down to a spot of 20 μm as well. However, this beam can also be used unfocused for experiments that do not require a high density of photon, or by research groups who prefer to install their own focusing optics. In the latter case, the spot size in the range of 1 - 2 μm is reachable with back-reflecting multilayer mirrors.

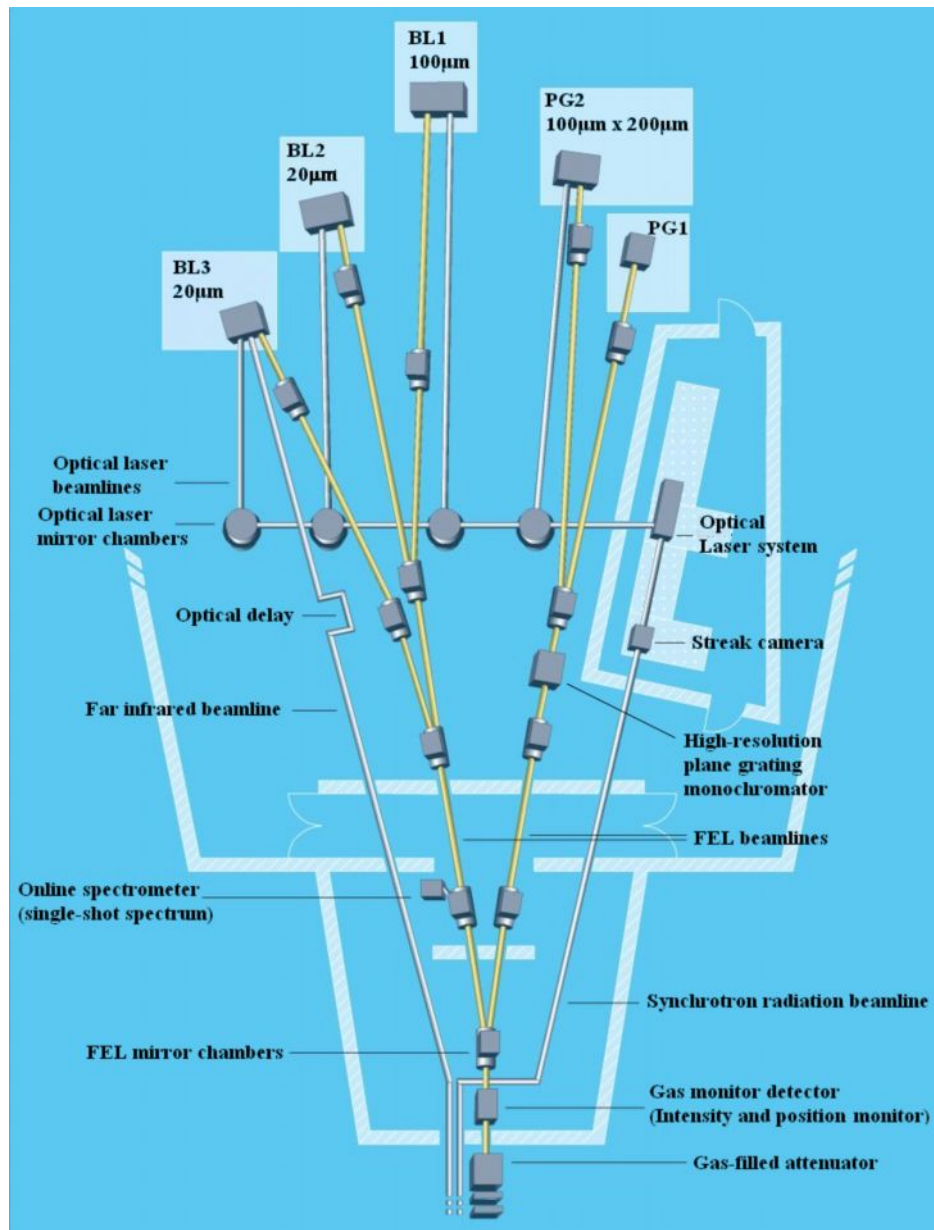


Fig.1.4 Schematic view of the FLASH experimental hall (from web-site www.desy.de)

The FLASH photon pulses have an inherent bandwidth of approximately 1 percent, but for many experiments, the monochromatic radiation is needed, for example, to study the excitation processes in molecules or atoms, and in some pump-and-probe experiments. Thus, a high-resolution plane grating monochromator has been developed to serve the beamlines PG1 and PG2 with FEL pulses of a narrower bandwidth. When the FEL beam hits the grating, a

selected wavelength passes through and proceeds to one of these beamlines, while optionally the 0th order including the higher harmonics is deflected to a special diagnostic port. The monochromator is tunable; by moving the grating and the plane mirror by remote control, different wavelengths can be picked out of the approximately 1-percent FEL bandwidth. An energy range from 20 eV to 1000 eV is covered. The spot size at PG2 is presently about 100 μm x 200 μm depending on the wavelength and monochromator settings.

The Linac Coherent Light Source (LCLS) is a SASE 1.5-15Å XFEL facility under construction at SLAC [16], and is now available to the first user experiments. The injector, linac, and new bunch compressors were commissioned in 2007 and 2008, establishing the necessary electron beam brightness at 14 GeV. The final phase of commissioning, including the FEL undulator and the long transport line from the linac, began in November 2008, with first 1.5-Å FEL light and the saturation observed in mid-April 2009. The LCLS has produced the first FEL light and saturation at a wavelength of 1.5 Å with a 3.3-m gain length and up to 1.1 mJ in the X-ray pulse (0.8×10^{12} photons/pulse). Table 1.2 summarizes the performance of LCLS facility.

Table 1.2. LCLS: FEL parameters

Wavelength	15	1.5	Å
FEL parameter	8.5	4.2	10^{-4}
Cooperation length	282	57	nm
Peak saturation power	4	8	GW
Average saturation power	0.23	0.23	W
Coherent photons/pulse	10.6	1.1	10^{12}
Peak photon flux	31	5.8	10^{24} Ph/s
Peak brightness*	0.28	15	10^{32}
Average brightness*	0.16	4.5	10^{22}
Instantaneous photon $\Delta E/E$	0.07	0.03	%
Beam radius, rms.	49	36	μm
Beam divergence, rms.	2.4	0.33	μrad
Pulse duration, rms.	70	70	fs
Pulse repetition rate	120	120	Hz
Single spike duration		1	fs
Number of spikes		~200	
Spike line width		3×10^{-4}	

*Ph./s/mm²/mrad²/.1%bw

In summary, the most of the X-ray FELs facilities have been developed or are in an advanced stage of development. These sources can produce coherent X-ray pulses with 10-100-fs temporal duration, the peak brilliance of which exceeds the existing synchrotron radiation facilities by 10 orders of magnitude. These high peak power X-rays will open the door to completely new scientific applications, such as structural studies on single molecules, nanoscale dynamics in condensed matter, femtochemistry and others.

Chapter 2

FEL radiation properties

In this chapter the temporal and spatial properties of the FEL radiation will be introduced. It starts with the description of the properties of the FLASH facility. The main aspects of the theory of FEL and the important issues will be discussed in detail. The radiation from the FEL has the spontaneous nature, and based on the Rice's theory [17]. In the case when the coherence time is smaller compared to the electron bunch distribution, the results of the FEL theory can be generalized in simple expressions.

In the second part of the chapter the first experimental data from FLASH will be presented. These results show good agreement with the theory and will be employed to modulate the incident single FEL pulses for our simulation in the following sections.

2.1. Statistical analysis of the chaotic optical field from a SASE FEL

The electron acceleration devices such as FELs utilize the distributed interaction between the electron beam and electromagnetic radiation. The random electron distribution in the beam of electron due to its corpuscular nature causes fluctuations in current density, identified as *the shot noise* in the beam current [18, 19]. The shot noise current is characterized by a “white” power spectrum whose density is proportional to the average electron flux of the beam. The electromagnetic fields are excited by each electron add incoherently, resulting in *spontaneous emission* noise in the radiation. If the electron beam is modulated, the fields excited by electrons become correlated, and coherent summation of radiation fields from individual particles occurs. In case where all electrons radiate in phase with each other, the generated radiation becomes coherent.

Electrons passing through a magnetic undulator emit a partially coherent radiation, which is called the undulator synchrotron radiation [20]. In the classical analysis [8, 9, 20], each wiggling electron is a point source, which can be treated as a moving radiating dipole. An individual electron moving in an undulator emits a wave packet of electromagnetic radiation which is in synchronism with the electron velocity. If the continuous electron beam advances through a periodic field of a wiggler, the radiation fields radiated by electrons, which enter the undulator at random, add up incoherently. Since the radiation process takes place in the absence of externally applied electromagnetic radiation, it is termed *spontaneous emission*. A number of approaches were employed for the analysis the FEL spontaneous emission [21, 22]. In the high-gain FELs, utilizing sufficiently long undulators, the spontaneous emission radiation excited in the first part of the undulator is amplified along the remainder of the interaction region [9, 10].

The FLASH is a single-pass FEL lasing in the soft X-ray regime based on a 1 GeV superconducting linear accelerator and described in detail in [21, 22] and references therein. A photoinjector generates very high-quality electron bunch trains that are accelerated to relativistic energies of up to 1 GeV and produce soft X-ray radiation during a single pass through a 30m long undulator. The generation of soft X-ray FEL radiation is based on the so-called *self-amplified spontaneous emission* (SASE) process.

As described above, in the undulator the electron bunches undergo a sinusoidal motion and emit synchrotron radiation. The radiation moves faster than the electron bunch and interacts with electrons further up leading to a charge density modulation within the bunch with a period corresponding to the fundamental in the wavelength spectrum of undulator. This well-defined periodicity in the emitting bunch enhances the power and coherence of the radiation field exponentially, whereas the electron and the resulting photon bunch travel once through a long undulator without the need for a resonator.

Since the exponential amplification process in the SASE FEL starts from spontaneous emission (shot noise) in the electron bunch, the SASE FEL radiation itself is of stochastic nature, meaning that the individual radiation pulses differ in their intensity, temporal structure and spectral distribution. Therefore, the exploitation of the unique properties of the FEL radiation requires the suitable pulse-resolved diagnostic tools. Furthermore, the online determination of the important photon beam parameters, such as intensity, spectral distribution and temporal structure, are mandatory for most user experiments. This requires diagnostics tools that operate in parallel to the user experiments and in a non-destructive way.

The gain in the FEL is based on the constructive growth of instability in the electron beam when it is propagating down a stream of undulators. The *microbunching instability* grows as a result of the interaction between the electron beam and electromagnetic wave it emits as it traverses the magnetic field of the undulator. The instability modulates the electron density on the scale of the radiation wavelength resulting in coherent radiation. Provided that the instability is strong enough, the radiation grows exponentially before reaching saturation. The wavelength of the FEL is determined by the resonance frequency (similar Eq. 1.1):

$$\omega_r = \frac{4\pi c\gamma^2}{\lambda_u (1 + K^2 / 2)}. \quad (2.1)$$

Here, γ is the relativistic factor of the beam, and λ_u and K are the undulator period and field strength parameter, respectively. For 1 Å operation, with $\lambda_u = 3.3\text{cm}$ and $K=3.1$, the relativistic parameter $\gamma \sim 30\,000$, corresponding to a beam energy of 15 GeV, accessible to modern accelerators.

As it was noted, the the SASE FEL starts up from the shot noise in the electron beam. The temporal behaviour of the system is that of a narrowband amplifier with a broad-band Poisson seed. Before saturation the output is a Gaussian random process and the radiated field is chaotic, quasi-monochromatic, polarized light. Near saturation, the transverse behaviour of the output is dominated by an intense, single spatial mode. Ignoring the transverse dependence, the radiated electric field can be expressed in the form

$$E(z, t) = A(z, t) \exp(ik_r r - i\omega_r t), \quad (2.2)$$

where z represents the location along the undulator at which the SASE is observed and t represents the temporal position in the radiation pulse.

The amplification process in the FEL amplifier passes two stages: linear and nonlinear. The linear stage lasts over significant fraction of the undulator length, and the main target for XFEL optimization is the field gain length. In the case of a cold electron beam with a long, flat-top electron bunch profile, the SASE field before saturation is the superposition of many electromagnetic wave packets emitted from randomly distributed, individual electrons. The spectrum of SASE FEL radiation has a Gaussian shape, and within the classical, one-dimensional theory [18-20, 22-26], the slowly varying envelope can be approximated [23] by

$$A(z, t) \cong A_0(z) \sum_{j=1}^{N_e} \exp \left(i\omega_r t_j - \frac{(t - t_j - z/v_g)^2}{4\sigma^2} \left(1 + \frac{i}{\sqrt{3}} \right) \right), \quad (2.3)$$

where N_e is the total number of electrons in the bunch, $A_0(z)$ contains the exponential growth factor, t_j is the random arrival time of the j^{th} electron at the undulator entrance, v_g is the group velocity of each wave packet, $\sigma = 1/(\sqrt{3}\sigma_\omega)$ is the characteristic wave packet width and $\sigma_\omega = \omega_r \sqrt{3\sqrt{3}\rho_p / k_u z}$ is rms SASE bandwidth, and ρ_p the FEL Pierce parameter.

The field amplitude Eq. (2.3) is expressed as a sum of independent random terms. Rice [27] has developed the comprehensive method to analyze such sums using *the central limit theorem (CLT)*. In probability theory, the CLT states the conditions under which the sum of a sufficiently large number of independent random variables, each with finite mean and variance, will be approximately normally distributed [28]. The CLT also requires the random variables to be identically distributed, unless certain conditions are met. The CLT also justifies the approximation of large-sample statistics to the normal distribution in controlled experiments.

Initially, the Rice's work has been motivated by the study of shot noise in electrical circuits - a type of *electronic noise* that occurs when the finite number of particles that carry energy is small enough to give rise to detectable statistical fluctuations in the measurement. At

present, his approach has important applications in statistical optics [29] and, in particular, in the description of the chaotic output of the SASE FEL. In result, the statistical description of the spikes at the output can be presented such in the frequency- and in the time-domain. The output intensity as a function of time exhibits spiking [22, 26], and the width of the intensity peaks is characterized by the coherence time T_{coh} . The spectral intensity also exhibits spikes, and the width of the spectral peaks is inversely proportional to the electron bunch duration T_b . At a fixed position z along the undulator, the energy in a single SASE pulse is

$$W(z) \propto \int_0^{T_b} |E(z,t)|^2 dt, \quad (2.4)$$

where T_b is the duration of an electron bunch having uniform average density. For z fixed, the pulse can be separated into M statistically independent time intervals of width T_{coh} . The energy fluctuation within a single coherent region is 100%, but the fluctuation of the energy in the entire pulse is reduced and given by [23, 25]

$$\frac{\sigma_W^2}{W^2} = \frac{\langle (W - \langle W \rangle)^2 \rangle}{\langle W \rangle^2} \equiv \frac{1}{M} \equiv \frac{T_{coh}}{T_b}. \quad (2.5)$$

Here, the parameter M can be interpreted as *the average number of degrees of freedom* (or *modes*) in the radiation pulse, and σ_w is the SASE gain bandwidth. Radiation of the SASE FEL operating in the linear regime is Gaussian random process, so probability distribution of the energy in the radiation pulse is gamma-distribution [13,14,18,19]. The radiation energy per pulse $p_w(W)$ should fluctuate according to a Gamma distribution

$$p_w(W) = \frac{M^M}{\Gamma(M)} \left(\frac{W}{\langle W \rangle} \right)^{M-1} \cdot \frac{1}{\langle W \rangle} \exp\left(-M \frac{W}{\langle W \rangle} \right), \quad (2.6)$$

provided the FEL gain process is in the regime of exponential growth [31]. The parameter M cannot be less than unity. When M tends to the unity, the gamma probability density function tends to the negative exponential distribution. For large values of M this distribution tends to a Gaussian distribution.

2.1.1. Analysis of the radiation properties in the frequency domain

For many practical application of the SASE FEL radiation, a monochromator has to be installed at the FEL amplifier exit with the transmission function $H_m(\omega)$. Thus, the Fourier harmonic of the electromagnetic field \vec{E} at the undulator exit and the Fourier harmonic of the input current \vec{I} are connected by the relation

$$\bar{E}(\omega) = H_m(\omega) H_A(\omega) \bar{I}(\omega), \quad (2.7)$$

where H_A is the spectral Green's function of the FEL amplifier. For a narrow-band monochromator (with resolution better than the typical width of the spike in the spectrum), the energy in the radiation pulse, W , after the monochromator is proportional to $|\bar{E}(\omega)|^2$. So, this energy fluctuates from pulse to pulse in accordance with the negative exponential probability distribution. It is worth mentioning that such a distribution is a feature of completely chaotic polarized radiation. The spectral interval of coherence can be defined as

$$\Delta\omega_c = \int_{-\infty}^{+\infty} |g_1(\omega - \omega')|^2 d(\omega - \omega'), \quad (2.8)$$

where *the first-order spectral correlation function $g_1(t)$* is

$$g_1(\omega, \omega') = \frac{\langle \bar{E}(\omega) \bar{E}^*(\omega') \rangle}{\sqrt{\langle |\bar{E}(\omega)|^2 \rangle \langle |\bar{E}(\omega')|^2 \rangle}}. \quad (2.9)$$

The value of the spectral coherence for case of a rectangular bunch with duration T is given by

$$\Delta\omega_c = \frac{2\pi}{T}. \quad (2.10)$$

Let the monochromator function $H_m(\omega)$ be symmetric with respect to the FEL resonance frequency ω_0 . Two case of the monochromator line profile can be considered: a Gaussian and a rectangular profile. The rectangular line of the monochromator is given by ($\omega > 0$)

$$|H(\omega)|^2 = 1 \quad , \text{for} \quad |\omega - \omega_0|^2 < \frac{\Delta\omega_m}{2} \quad (2.11a)$$

$$|H(\omega)|^2 = 0 \quad , \text{for} \quad |\omega - \omega_0|^2 > \frac{\Delta\omega_m}{2}, \quad (2.11b)$$

and the Gaussian line of the monochromator is defined as

$$|H(\omega)|^2 = \exp\left[-\frac{(\omega - \omega_0)^2}{2\sigma_m^2}\right]. \quad (2.12)$$

The normalized dispersion of the energy distribution is calculated as follows

$$\sigma_E^2 = \frac{\langle (W - \langle W \rangle)^2 \rangle}{\langle W \rangle^2} \dots \quad (2.13)$$

When the monochromator linewidth is much large than the interval of the spectral coherence and much less than the FEL amplifier bandwidth, the dispersion is inversely proportional to the monochromator linewidth

$$\begin{aligned}\sigma_E^2 &\approx 2\pi / (\Delta\omega_m T) \\ \sigma_E^2 &\approx \sqrt{\pi} / (\sigma_m T)\end{aligned}\tag{2.14}$$

for the rectangular and the Gaussian monochromator line, respectively. When the monochromator linewidth is much larger than the bandwidth of the FEL amplifier, the energy fluctuations are defined by the bandwidth of the FEL amplifier

$$\sigma_E^2 \approx \sqrt{\pi} / (\sigma_A T).\tag{2.15}$$

2.1.2. Analysis of the radiation properties in the time domain

When the coherence time T_{coh} is small than the duration of an electron bunch T_b , the coherence time can be expressed in terms of the first-order time correlation function $g(t)$ according to

$$T_{coh} = \int |g_1(t)|^2 dt,\tag{2.16}$$

where the first-order time correlation function $g_1(t)$ is

$$g_1(t_1 - t_2) = \frac{\langle A(t_1) A^*(t_2) \rangle}{\sqrt{\langle |A(t_1)|^2 |A(t_2)|^2 \rangle}}\tag{2.17}$$

and $A(t)$ is the amplitude of electromagnetic field defined in Eq. 2.2. Using an approximation for the field correlation function $g_1(t)$

$$g_1(t) = \exp\left(-\frac{\sigma_\omega^2 t^2}{2}\right).\tag{2.18}$$

When the SASE FEL operates in the high-gain linear regime, the explicit expression for the coherence time can be re-written as

$$T_{coh} = \frac{\sqrt{\pi}}{\sigma_\omega}.\tag{2.19}$$

Summarizing, in the case when the coherence time is small compared to the electron bunch distribution, the results of the free electron laser theory [19, 23, 24-26] are simplified and can be generalized as follows [26]:

<i>number of modes</i>	$M \cong 2\sigma_t\sigma_\omega$
<i>average temporal spike separation</i>	$\langle \Delta t \rangle \cong \frac{\sqrt{2\pi}}{\sigma_\omega}$
<i>average temporal spike width</i>	$\langle \delta t \rangle \cong \frac{1}{\sqrt{2}\sigma_\omega}$
<i>coherence time</i>	$T_{coh} \cong \frac{\sqrt{\pi}}{\sigma_\omega}$
<i>number of modes</i>	$M \cong \frac{2\sqrt{\pi}\sigma_t}{T_{coh}}$
<i>average frequency spike separation</i>	$\langle \Delta \omega \rangle \cong \frac{\sqrt{2\pi}}{\sigma_t}$
<i>average frequency spike width</i>	$\langle \delta \omega \rangle \cong \frac{1}{\sqrt{2}\sigma_t}$
<i>range of frequency coherence</i>	$\langle \delta \omega \rangle \cong \frac{1}{\sqrt{2}\sigma_t}$
<i>number of modes</i>	$M \cong \frac{2\sqrt{\pi}\sigma_\omega}{\Omega_{coh}}$

The SASE FEL is a filtered chaotic light source, possessing high intensity and relatively long coherence length. It was found that the SASE pulse energy is described by a gamma-distribution. This type of measurement is an example of the conventional photon counting statistics. The time- and frequency-domain results present a new class of experimental data on the behaviour of the SASE chaotic optical field. The analysis of random noise are presented in [22, 30] provides a good initial description of new experiments [13, 14]. It remains as a challenge for future theoretical work to include the effect of the dependence of gain on the local electron density and, in particular, to determine the temporal duration of the output radiation pulse as a function of the electron bunch length.

2.2. First experimental results of an X-ray free-electron laser

2.2.1. Operation of a VUV FEL at 32 nm wavelength

The properties of FEL radiation [22] have been calculated for 30 nm wavelength with the three-dimensional, time-dependent simulation code FAST [30], predicting an average energy in the radiation pulse of up to 100 μJ for a bunch charge of 1 nC. Figure 2.1 shows the measured energies of many successive radiation pulses [13]. A large fluctuation is seen which is to be expected since in a SASE FEL the gain process starts from shot noise. Theoretically, the

radiation pulse energy should fluctuate according to a gamma distribution (Eq. 2.6) provided the FEL gain process is in the regime of exponential growth.

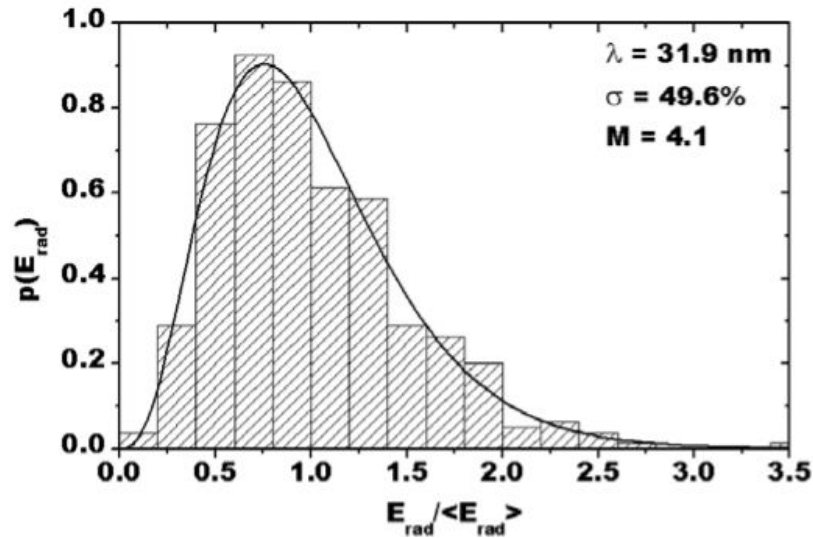


Fig. 2.1 Measured FEL-pulse energies for many successive pulses [13]: measured probability distribution of the radiation energy (histogram). The solid curve represents the Gamma distribution of equation (2.6) for $M=4.1$ which is calculated from the variance of pulse energy fluctuations. This is the expected distribution of a high-gain FEL operating in the exponential regime, with M being the total number of optical modes in the pulse.

It defines the number of optical modes in the radiation pulse and provides a relationship between the average number of spikes in the single-pulse wavelength spectra and the fluctuations of the pulse energy. The measured histogram in Figure 2.1 fits nicely the gamma distribution (Eq. (2.6)) with $M=4.1$. The statistical analysis can not distinguish between transverse and longitudinal modes. Since the high degree of transverse coherence has already been concluded from the observed angular divergence, the transverse mode number should be less than two. Consequently, we expect three to four longitudinal modes. According to statistical analysis and numerical simulation, this implies that, on average, two wave packages (or *spikes*) should be present in the time profile of each FEL radiation pulse.

While the ultra-short pulse duration has up to now precluded a direct measurement of the temporal structure of the FEL pulses, the single-pulse wavelength spectra are accessible and may be used to estimate the radiation pulse duration. A set of different spectra is presented in Figure 2.2. They were taken with a grating spectrometer equipped with an intensified CCD camera. The FWHM pulse duration is obtained from the typical width $\Delta\omega$ of the spikes in the single-pulse spectra using the relation $\tau_{rad}=2\pi/(\Delta\omega)$ fs. With average radiation pulse energy of 10 μJ , this correspond to an average power of 0.4 GW within the FEL pulse and approximate 1 GW inside the spikes. The average number of such spikes within the bandwidth of the FEL scales with the number of longitudinal modes.

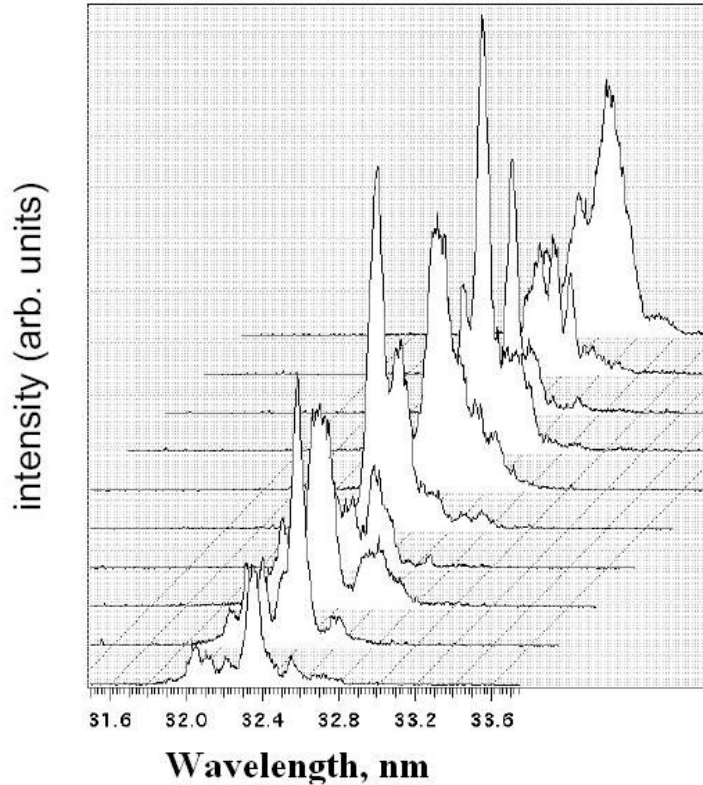


Fig. 2.2 Different single-shot wavelength spectra of FEL radiation pulses measured at the VUV-FEL operating in the exponential regime (*from work of R. Treusch, M.Kuhlmann (DESY News, 2005)*). The different shots are shown with different shapes. Note that the number of spikes in the spectrum is in average equal to the number of spikes (coherent wave packets) in the time domain.

The FWHM pulse duration of radiation pulses at the VUV-FEL in [13] has been determined at 25 fs in three entirely independent ways: *(i)* spectral analysis of a spiky structure of single-pulse wavelength spectra (i.e., see Fig. 2.2); *(ii)* statistical analysis of pulse-to-pulse intensity fluctuations; *(iii)* time-domain measurement of the longitudinal electron bunch profile corroborates the existing of such a short, leading spike. It is in qualitative agreement with the results of numerical beam dynamics simulation and the subsequent numerical simulation of the FEL process.

2.2.2. Operation of a VUV FEL at 13.7 nm wavelength

In the next step, the measurement and characterization of the properties of the FEL radiation at a wavelength of 13.7 nm will be introduced. The average energy of pulse at this wavelength was about 70 μ J [14]. The spatial profile of the FEL radiation was detected on a Ce:YAG screen located 23.5m downstream of the undulator exit. The spot size is 2.1 mm (FWHM), which corresponds to an angular divergence of 90+10 μ rad (FWHM). The radiation mode in the far-field is nearly axial symmetric.

The average FLASH pulse energy versus undulator length for the case of exponential growth can be seen in Fig. 2.3. The radiation energy was measured with a microchannel-plate-

(MCP-) based detector, which was operated with a 5-mm diameter aperture and was located 18.5m from the undulator. The interaction length in the undulator (and hence amplification) was changed by means of a transverse kick of the electron-beam trajectory between the undulator modules, which is strong enough to stop the FEL amplification process downstream of the orbit kick. With the FEL interaction suppressed along the whole length of the undulator chain, the residual spontaneous emission from the full undulator length and also the full electron bunch was measured. The FEL interaction was switched on gradually along the undulator, and the energy in the radiation pulse grew steadily. The measurement gives an estimate for the coherence time $\tau_c = 4.2 \pm 0.5$ fs. In this case, using the gamma-distribution (Eq. 2.6) and the value of $M=1.9$ (the average number of ‘degrees of freedom’ or ‘modes’ in the radiation pulse) and an estimate for the coherence time 4.2 ± 0.5 fs, the radiation pulse length at the end of the regime of exponential growth of about 8 ± 1 fs.

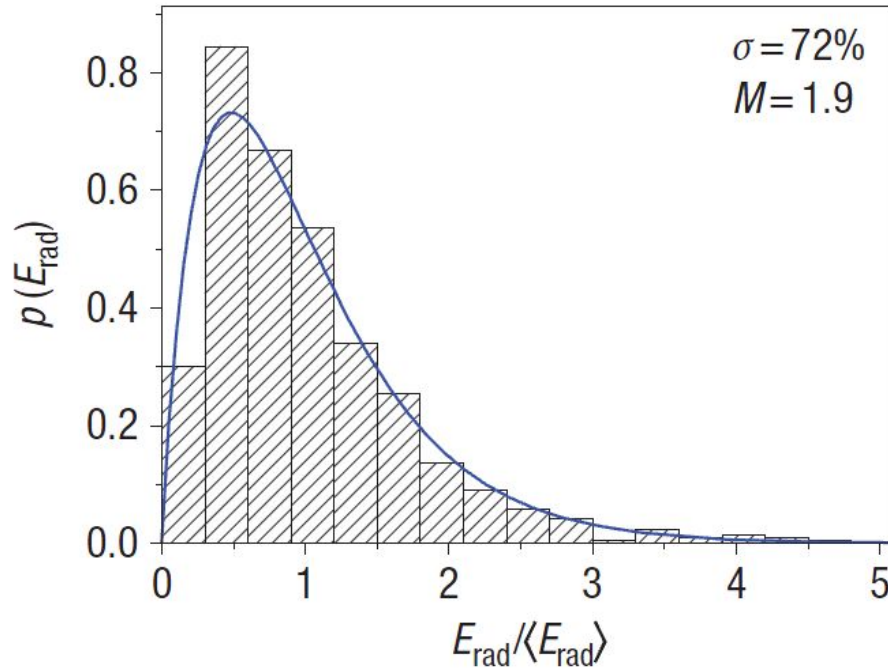


Fig. 2.3 Measured FEL-pulse energies for many successive pulses [14] measured probability distribution of the radiation energy (histogram). The solid curve represents the gamma distribution of equation (2.6) for $M= 1.9$ which is calculated from the variance of pulse energy fluctuations. This is the expected distribution of a high-gain FEL operating in the exponential regime, with M being the total number of optical modes in the pulse.

Also, it was obtaining [14], that the FLASH has produced unprecedented powers for EUV radiation at a fundamental wavelength of 13.7 nm, and harmonics with wavelengths as low as 2.75 nm (that is, in the range of a soft X-ray FEL). The experimental measurements show that FLASH operates now at its ultimate performance level, with a peak brilliance of $(6 \pm 3) \cdot 10^{29}$, $(2 \pm 1) \cdot 10^{28}$ and $(2 \pm 1) \cdot 10^{27}$ photons per (s mrad² mm² 0.1% bandwidth) at 13.7, 4.6 and 2.75 nm, respectively. At the 5th harmonic wavelength, FLASH is already approaching the wavelength

range of the European XFEL and LCLS, but with lower brilliance. However, it is still higher than the peak brilliance of the third-generation SR sources by few orders of magnitude.

2.2.3. Operation of a VUV FEL at 6.5 nm wavelength

In the autumn of 2007, the FLASH has been upgraded by installation of a 6th superconducting accelerator module to reach the electron energy of 1 GeV. User operation is regularly running at wavelengths down to 7 nm [31, 32]. Radiation pulse energies exceeding 40 μJ have been observed. Also the 2nd, 3rd, and 5th harmonics have been seen, and applied by users [31]. Figure 2.4 shows the spectrum of the SASE radiation peaking at 6.5 nm [32]. In these works, the preliminary analysis of the pulse length for observed wavelengths was carried out, and it was between 5 and 15 fs (FWHM).

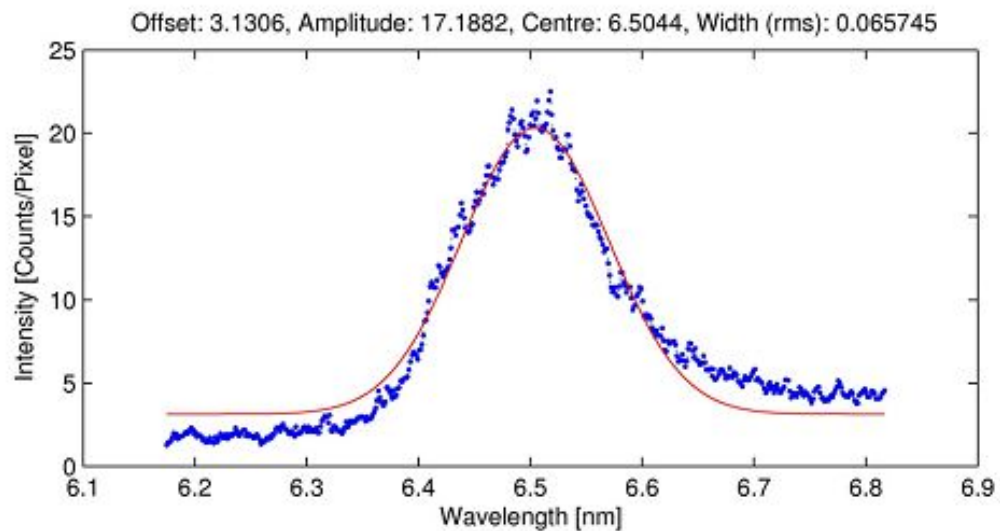


Fig. 2.4 Spectrum of the SASE FEL radiation peaking at 6.5 nm generated at FLASH [32]

In summary, the radiation from the SASE FEL operating in the linear regime possesses the typical properties of completely chaotic polarized light. Shot noise in the electron beam is a Gaussian random process; the FEL amplifier, operating in the linear regime, can be considered as a linear filter, which does not change statistics. As a result, the radiation is also a Gaussian random process. In this case, the probability distribution of the instantaneous radiation power should be the negative exponential distribution (the notion of instantaneous power refers to a certain moment of time and a point in space, considered over an ensemble of pulses). Also, the finite-time integrals of the instantaneous power (energy in the radiation pulse) and the integrated spectral density (measured after the monochromator) should fluctuate in accordance with the gamma distribution (Eq. 2.6). The parameter M can be interpreted as the average number of “degrees of freedom” or “modes” in the radiation pulse. Fluctuations reach a maximum value at the end of the linear regime.

When approaching a saturation point, the statistical properties of the radiation change drastically on a scale of one field gain length. One useful property of the non-linear regime is the reduction of the radiation energy fluctuations by approximately two times relative to the linear regime. Sensitivity of the radiation pulse energy with respect to jitters of machine parameters is reduced as well. Radiation power in the non-linear regime continues to grow due to the growth of sidebands in the non-linear media. As a result, there is a broadening of the spectrum. The spectral brightness and the degree of transverse coherence reduce as well. Maximum brightness of the radiation occurs at the undulator length of about ten field gain lengths.

Chapter 3

The present theory of the interaction soft X-ray radiation with medium

In this chapter we briefly reviewed some fundamentals of X-ray interaction with matter, since they will be used later in chapter 7 to carry out the theoretical and experimental analysis of the X-ray diffraction patterns arising due to the interaction process of fs- FEL pulses with periodical multilayers. It starts with a discussion of the refractive index of the materials for X-rays. In the second part of this chapter, the basic formalism of the interaction of ultra short pulses with the media is demonstrated by linear optics reflection theory (LORT).

3.1. X-ray interactions and wave equations

X-rays are electromagnetic radiation and their propagation can be described by the *Maxwell equations* (similarly to the visible optics [1]):

$$\begin{aligned}\nabla \times \vec{H} &= \frac{\partial \vec{D}}{\partial t} + \vec{J} \\ \nabla \times \vec{E} &= -\frac{\partial \vec{B}}{\partial t} \\ \nabla \cdot \vec{B} &= 0 \\ \nabla \cdot \vec{D} &= \rho\end{aligned}\tag{3.1}$$

where \vec{E} is the electric field vector, \vec{H} is the magnetic field vector, \vec{D} is the electric displacement, \vec{B} is the magnetic density or magnetic induction, \vec{J} is the current density, ρ is the charge density, ϵ_0 is the permittivity (dielectric constant) of free space, and μ_0 is the magnetic permeability. In free space (vacuum), the constitutive relations take the form

$$\begin{aligned}\vec{D} &= \epsilon_0 \vec{E} \\ \vec{B} &= \mu_0 \vec{H}.\end{aligned}\tag{3.2}$$

These equations can be combined to form a *vector wave equation* describing the propagation of electromagnetic waves. The mathematical description covers electromagnetic phenomena extending from very long wavelength, to radiowaves, microwaves, infrared, visible, ultraviolet, and x-rays and beyond. The vector wave equation can be obtained from Maxwell's equation by taking $\nabla \times$ (Eq.3.1) and using the vector identity $\nabla \times (\nabla \times \vec{A}) = \nabla(\nabla \cdot \vec{A}) - \nabla^2 \vec{A}$ to obtain

$$\nabla \times (\nabla \times \vec{E}) = \nabla \times \left(-\frac{\partial \vec{B}}{\partial t} \right).\tag{3.3}$$

After calculation, the vector wave equation can be written:

$$\left(\frac{\partial^2}{\partial t^2} - c^2 \nabla^2\right) \mathbf{E}(r, t) = \frac{1}{\epsilon_0} \left(\frac{\partial J(r, t)}{\partial t} + c^2 \nabla \rho(r, t)\right). \quad (3.4)$$

Eq. 3.4 is the key equation in the considering radiation, scattering and refractive index in situations including free and bound electrons, single atoms and the various distributions of atoms, for example, in our case, the multilayer structures. Here the topic of interest is the X-ray scattering by multi-electron atoms near an absorption edge.

From the vector wave equation (Eq. 3.4), in the case of the propagation of transverse waves inside the multilayer structure, the $\nabla \rho$ term does not contribute, nor does the longitudinal component of \vec{J} . Thus, for the transverse electromagnetic waves in the form $\exp[-i(\omega t - \mathbf{k} \cdot \mathbf{r})]$, propagating in the vector \mathbf{k} -direction, only the field components transverse to \mathbf{k} need to be considered, so the transverse wave equation is

$$\left(\frac{\partial^2}{\partial t^2} - c^2 \nabla^2\right) \mathbf{E}_T(r, t) = \frac{1}{\epsilon_0} \left(\frac{\partial \mathbf{J}_T(r, t)}{\partial t}\right). \quad (3.5)$$

For the special case of forward scattering, the positions of the electrons within the atom ($\Delta \mathbf{k} \cdot \Delta \mathbf{r}_s$) are irrelevant, as are the positions of the atoms themselves. The contributing current density is then

$$\mathbf{J}_0(r, t) = -en_a \sum_s \mathbf{g}_s \mathbf{v}_s(r, t), \quad (3.6)$$

where n_a is the average number density of atoms, and $\sum_s \mathbf{g}_s = Z$. The oscillating electron velocities

$$\mathbf{v}(r, t) = \frac{e}{m} \frac{1}{(\omega^2 - \omega_s^2) + i\gamma\omega} \frac{\partial \mathbf{E}(r, t)}{\partial t} \quad (3.7)$$

are driven by the incident field \mathbf{E} such that the contributing current density is

$$\mathbf{J}_0(r, t) = \frac{en_a}{m} \sum_s \frac{\mathbf{g}_s}{(\omega^2 - \omega_s^2) + i\gamma\omega} \frac{\partial \mathbf{E}(r, t)}{\partial t}, \quad (3.8)$$

where g_s are the *oscillator strengths*, which are integers in semi-classical model that indicate the number of electrons associated with a given resonance frequency ω_s . In the quantum mechanic description, these oscillator strengths arise naturally as non-integer transition probabilities between stationary states. The sum of g_s is equal to the total number of electrons Z . Substituting this into the transverse wave equation (Eq. 3.5), one obtains

$$\left(\frac{\partial^2}{\partial t^2} - c^2 \nabla^2\right) E_T(r, t) = \frac{en_a}{\epsilon_0 m} \sum_s \frac{g_s}{(\omega^2 - \omega_s^2) + i\gamma\omega} \frac{\partial^2 E(r, t)}{\partial t^2}. \quad (3.9)$$

Combining terms with similar operators

$$\left\{ \frac{\partial^2}{\partial t^2} \left(1 - \frac{en_a}{\epsilon_0 m} \sum_s \frac{g_s}{(\omega^2 - \omega_s^2) + i\gamma\omega} - c^2 \nabla^2 \right) \right\} E_T(r, t) = 0 \quad (3.10)$$

written in the standard form of the wave equation as

$$\left\{ \frac{\partial^2}{\partial t^2} - \frac{c^2}{n^2(\omega)} \nabla^2 \right\} E_T(r, t) = 0. \quad (3.11)$$

The frequency dependent *index of refraction* $n(\omega)$ is identified as

$$n(\omega) \equiv \left\{ 1 - \frac{en_a}{\epsilon_0 m} \sum_s \frac{g_s}{(\omega^2 - \omega_s^2) + i\gamma\omega} \right\}^{1/2}. \quad (3.12)$$

For soft X-ray radiation, the term ω^2 is very large compared to the quantity $e^2 n_a / \epsilon_0 m$, so that to a high degree of accuracy, the index of refraction can be written as

$$n(\omega) \equiv 1 - \frac{1}{2} \frac{en_a}{\epsilon_0 m} \sum_s \frac{g_s}{(\omega^2 - \omega_s^2) + i\gamma\omega}. \quad (3.13)$$

The refractive index can then be re-written as

$$n(\omega) \equiv 1 - \frac{n_a r_e \lambda^2}{2\pi} [f_1^0(\omega) - if_2^0(\omega)] \quad (3.14)$$

where r_e is the classical electron radius, f_1 and f_2 are real and imaginary parts of the atomic scattering factor, which can be written as

$$f^0(\omega) = f_1^0(\omega) - if_2^0(\omega) = \sum_s \frac{g_s \omega^2}{\omega^2 - \omega_s^2 + i\gamma\omega}. \quad (3.15)$$

In X-ray diffraction the refractive index is written in the simplified form

$$n(\omega) = 1 - \delta + i\beta \quad (3.16)$$

where

$$\begin{aligned} \delta &= \frac{n_a r_e \lambda^2}{2\pi} f_1^0(\omega) \\ \beta &= \frac{n_a r_e \lambda^2}{2\pi} f_2^0(\omega) \end{aligned} \quad (3.17)$$

Thus, the complex refractive index containing the atomic form factors, which may obtain as a result of relativistic quantum theory of dispersion Kramers-Kronig relations (see *Appendix A*), can be calculated or determined by measurements.

The absorption coefficient β links with *the linear absorption coefficient* α as

$$\alpha = \frac{4\pi\beta}{\lambda}. \quad (3.18)$$

The refractive index at soft X-ray range deviates only by a small amount from unity, and the expression $n=1-\delta-i\beta$ is a standard notation. Typical values are $\delta\sim 10^{-5}$ and $\beta\sim 10^{-6}$. The transmitted intensity I through a layer of material with thickness x is related to the incident intensity I_0 according to the inverse exponential power law that is usually referred to as *Beer-Lambert law*:

$$I = I_0 \exp(-\alpha x). \quad (3.19)$$

3.2. Linear-optics reflection theory

In the last decade, much interest has been developed in the study of the propagation of ultra short pulses in the resonant or non-resonant medium [33-38]. In this section we discussed the general aspects of the theory of the reflection of short pulses in linear optics known as *the linear-optics reflection theory* [33-34]. Let's start with the well-known equation for the reflection of a monochromatic beam of light falling on a linear dielectric medium. If the incident beam E_I has frequency ω , then the reflected beam has the same frequency; the amplitude is given by

$$E_R = J(\omega) E_I \quad (3.20)$$

where $J(\omega)$ is the response function of the system. For finite wave packets $E_I(ct-z)$ and $E_R(ct+z)$ with a spread of frequencies, Eq. (3.20) are generalized by integration over all frequencies:

$$\begin{aligned} E_R(\tau_+) &= (2\pi)^{-1/2} \int_{-\infty}^{+\infty} E_R(\omega) \exp(-i\omega\tau_+) d\omega = \\ &= (2\pi)^{-1/2} \int_{-\infty}^{+\infty} J(\omega) E_I(\omega) \exp(-i\omega\tau_+) d\omega \end{aligned} \quad (3.21)$$

where $\tau_{\pm}=ct\pm z$ and $E_I(\omega)$ and $E_R(\omega)$ are now the Fourier transforms (*Appendix B*) of the incoming and outgoing pulses $E_I(\tau_-)$ and $E_R(\tau_+)$, defined by

$$E(\omega) = (2\pi)^{-1/2} \int_{-\infty}^{+\infty} E(\tau) \exp(i\omega\tau) d\tau. \quad (3.22)$$

Unfortunately integral (3.21) cannot be solved analytical, because the response function, in general, is a complicated function of ω , except in the trivial monochromatic case. On other side,

we can solve this equation numerically using the calculated and/or the experimental obtained response function of our object.

The general relation between the electric field of incoming pulse $E_I(t)$ and $E_R(t)$ after interaction with the system is given by

$$E_R^+(t) = \int_0^{+\infty} J^+(\tau, t) E_I^+(t - \tau) d\tau . \quad (3.23)$$

Here $E_I^+(t)$ and $E_R^+(t)$ are the complex analytical signals assigned to the positive frequency part of the temporal Fourier-transform (Eq. 3.21). The functions $E_I^-(t)$, $E_R^-(t)$ and $J^-(\tau, t)$ assigned to the negative frequency part are the complex conjugate quantities of the functions involved in Eq. 3.23. Now we can demonstrate two limited cases: (i) ultra-short pulse with δ -function temporal profile and (ii) usual monochromatic beam.

If the electric field of incident pulse $E_I^+(t)$ is specified by the Dirac δ -function-like $A \cdot \delta(t - t_0)$, from Eq. 3.23 we obtain

$$E_R^+(t) = J^+(t - t_0, t) A \quad (3.24)$$

where A is the amplitude of incident pulse. Eq. 3.23 suggests a function with two variables $J(\tau, t)$ which is to be called *the time-dependent pulse response function* (PRF) of the system.

If monochromatic light with amplitude $A \cdot \exp(i\omega t)$ is incident on the system, Eq. 3.24 takes on the form

$$E_R^+(t) = \tilde{J}^+(\omega, t) A \exp(i\omega t) \quad (3.25)$$

where $\tilde{J}^+(\omega, t)$ is the Fourier transform

$$\tilde{J}^+(\omega, t) = \int_0^{+\infty} J^+(\tau, t) \exp(-i\omega\tau) d\tau \quad (3.26)$$

$\tilde{J}^+(\omega, t)$ is called the *time-dependent frequency response function* (FRF) of the system.

In the special case of a stationary system, which means that $J(\tau, t)$ and $\tilde{J}^+(\omega, t)$ are independent from the temporal variable t , Eq. (3.25) transforms to Eq. (3.20) and describes a monochromatic wave.

In principle, it is possible to determine the response functions of the generally non-stationary system in two ways: (i) the system is irradiated by monochromatic light with frequency ω and the reflected signal is measured as a function of t and ω ; (ii) sending δ -pulses at various times t_0 onto the system, the electric field of scattering signal is measured as a function of t and t_0 .

As shown in Fig. 3.1, the measured reflectivity of a Si/C multilayer during the low-intensity FLASH pulse is in agreement with that measured with synchrotron radiation, if the flux is substantially below the damage [39, 40].

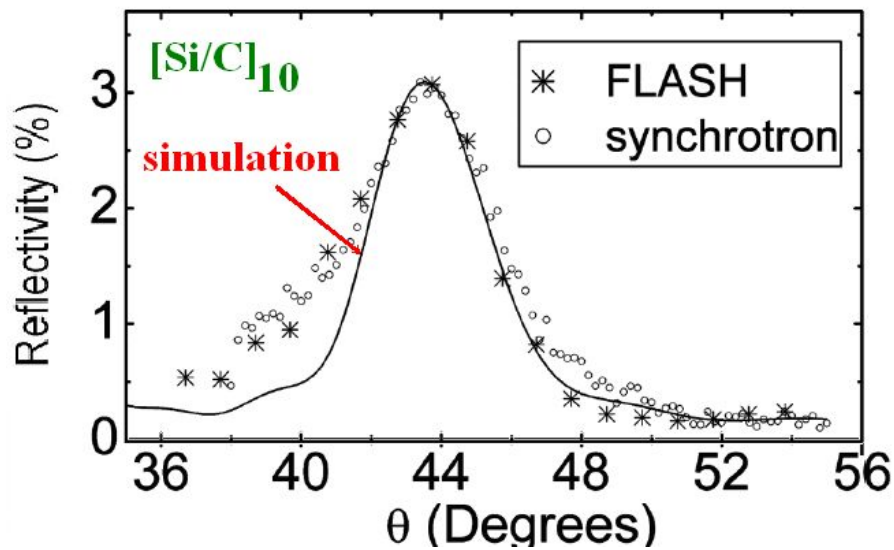


Fig. 3.1 Low-fluence reflectivity as a function of the off-normal angle of incidence measured at FLASH. Overlaid is the data measured at the synchrotron [39, 40].

Thus, in the case of low-intensive ultra short FEL pulse, the FRF function demonstrates the time-independent behavior and can be pre-determined by the synchrotron radiation. The increase of flux above the critical value (in this case, $0.1\text{J}/\text{cm}^2$ [39]), lead to an increase of the role of different excitation processes inside materials and the FRF function will change during the interaction (Fig. 3.2).

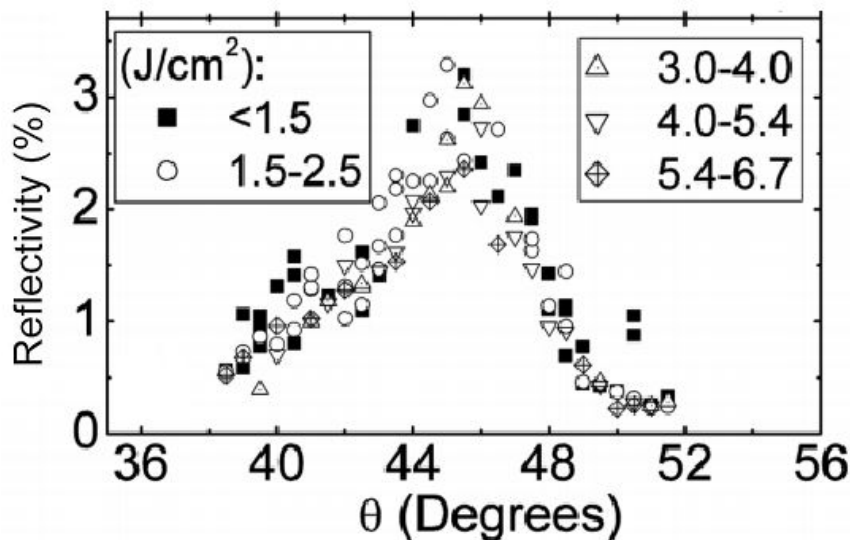


Fig. 3.2 Reflectivity as a function of the off-normal angle of incidence θ at higher fluences [39]

The change of maximum reflectivity for a larger range of fluence is shown in Fig. 3.3 The reflectivity of the Si/C multilayer decreases somewhat with increasing fluence. The calculations

in [39] show that the opacity of silicon increases with temperature due to enhanced two-photon absorption, leading to a reduced penetration length of the light into the multilayer and a reduced reflectivity. It was obtained that the reflectivity drops by a factor of about 0.5 at the end of the pulse. The pulse-averaged reflectivity drops by a factor of 0.2 only, as indicated in Fig. 3.3.

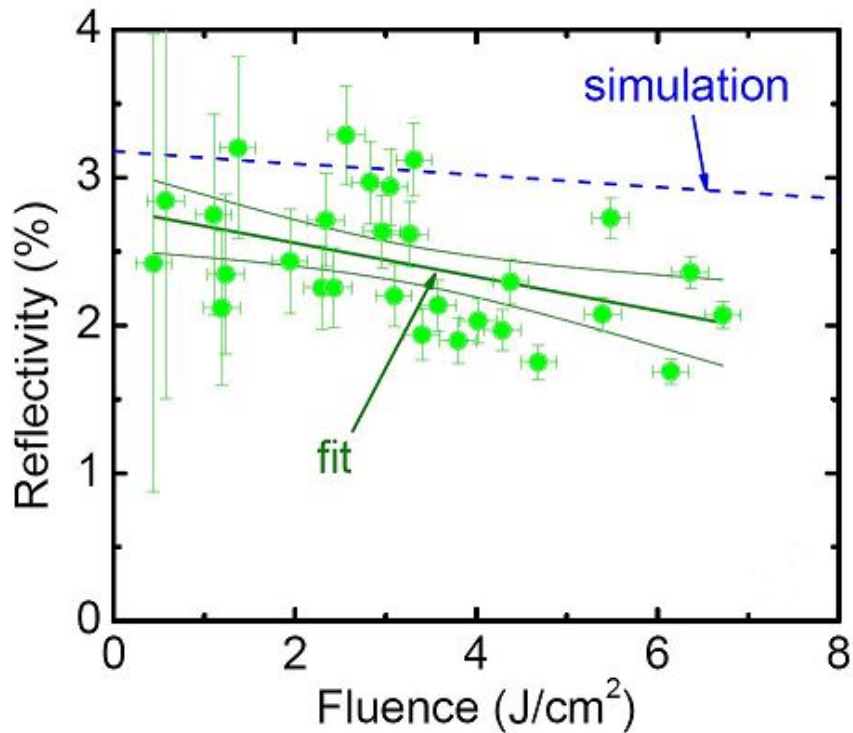


Fig. 3.3 Reflectivity of Si/C multilayer over angles between 44 and 47 degrees as a function of pulse fluence measured at FLASH for 32 nm wavelength [39].

In this work [39], the authors measured the fluence dependent damage of the multilayer by numerical simulations in terms of a hot dense plasma model. Since the sample enters in the state of warm-dense matter (WDM), which is generally not very well understood, the physical models originally developed for hot dense plasmas needed to be extended into the WDM regime.

The standing-wave intensity distribution inside the multilayer structure could be calculated using standard methods for continuous radiation based on the Fresnel equations (see, Chapter 4). These time-independent models are applicable as long as the time for the light to propagate a few attenuation lengths (~ 2 fs) is much shorter than the pulse length (~ 25 fs). Hau-Riege S.P. *et. al.* [39] applied multiplicative correction factors to the opacities based on the XSN opacity model—an *average-ion screened-hydrogen model* [41]. The correction factors were calculated from the ratio of the XSN opacity at a given temperature and density relative to the XSN opacity at room-temperature and solid density. The index of refraction was obtained from the opacities using the Kramers-Kronig dispersion formula.

From this paper one can conclude, that in case of low-intensive FEL pulses, the scattering properties of periodical multilayer are similar to the case of continuous radiation. On other the side, in case of the high-intensive FEL pulse, the scattering properties of periodical multilayer are time-dependent functions and depend on the parameters of incident pulse, such as the temporal and spectral structures, and the fluence. This behavior cannot be described in terms of existing theories.

3.2.1. The time-dependent power spectrum

The spectral and temporal properties of a non-stationary light signal are adequately described by *the time-dependent power spectrum* (TDS) which was first introduced by Page [42]. Alternatively, the Wigner distribution function is used to represent the propagation of light in media [38, 43].

The time-dependent power spectrum is related to the time-dependent correlation function $R(t, t-\tau)$ by

$$B(\omega, t) = \int_0^{+\infty} R(t, t-\tau) \exp(-i\omega\tau) d\tau + c.c. \quad (3.27)$$

where c.c. is complex conjugate and $R(t, t-\tau)$ is given by

$$R(t, t-\tau) = \langle E^+(t) E^-(t-\tau) \rangle. \quad (3.28)$$

The brackets indicate an ensemble average. Because $B(\omega, t)$ is an even function, the “+” or “-” symbol of $B(\omega, t)$ is omitted. From $B(\omega, t)$ we can derive the intensity $I(t)$ and the time-dependent energy spectrum $S(\omega, t)$ by integration

$$I(t) = \frac{1}{2\pi} \int_0^{\infty} B(\omega, t) d\omega \quad (3.29)$$

$$S(\omega, t) = \int_{-\infty}^t B(\omega, t) d\tau$$

Starting from Eq. 3.23, after interaction with the system, $B_R(\omega, t)$ is found to be

$$B_R(\omega, t) = (\pi/2) \int_{-\infty}^{+\infty} d\omega' \int_{-\infty}^t dt' J_B(\omega - \omega', t - t', \omega, t) B(\omega', t') \quad (3.30)$$

with

$$J_B(\omega - \omega', t - t', \omega, t) = \int d\tau \int d\tau' J^+(t - t', t) J^-(t - t' + \tau - \tau', t - \tau) \times \exp(-i[(\omega - \omega')\tau' + \omega(\tau - \tau')]) + c.c. \quad (3.31)$$

In the general case of a full non-stationary system, it must be described by the TDS response function $J_B(\omega - \omega', t - t', \omega, t) + c.c.$, which is a function of four variables. In the general case, this function can not be determined experimentally if, instead of the field strength amplitude, only the TDS in connection with a detector can be measured. For instance, applying a δ -function at time t_0 , Eq. 3.30 leads to

$$B_R(\omega, t) = \int_0^{\infty} J^+(t - t_0, t) J^-(t - t_0 - \tau, t - \tau) \exp(-i\omega\tau) |A|^2 d\tau + c.c. \quad (3.32)$$

In the case of a monochromatic wave, $B_R(\omega, t)$ is

$$B_R(\omega, t) = \int_0^{\infty} \tilde{J}^+(\omega_0, t) \tilde{J}^-(\omega_0, t - \tau) \exp(-i(\omega_0 - \omega)\tau) |A|^2 d\tau + c.c. \quad (3.33)$$

Nevertheless, if both the TDS and the PRF or the FRF are “quasi-stationary” (these functions must not change during a time interval of the order of the greater correlation length of the functions) [36, 37], the Eq. 3.30 takes on the simple form

$$B_R(\omega, t) = |\tilde{J}^+(\omega, t)|^2 B(\omega, t) \quad (3.34)$$

The function

$$\mathcal{G}(\omega, t) = |\tilde{J}^+(\omega, t)|^2, \quad (3.35)$$

describes the time- and frequency-dependent reflectivity (or transmittance) under quasi-stationary conditions.

3.2.2. Bandwidth limited Gaussian-shaped pulse

In this section we deal with an example that is important for spectroscopy with ultra short-time pulse. A single pulse with analytical signal of the following form

$$E^-(t) = A_0 \exp\left[-(t/T_A)^2\right] \exp(-i\omega_0 t) \quad (3.36)$$

In this case, the TDS and the correlation function R can be calculated numerically from Eqs. 3.27 and 3.28, respectively. In Fig. 3.4 the time-dependent spectrum $B(\omega, t)$ is shown as a two-dimensional function of time and energy. It can be seen that for $t > t_{max}$, negative values of $B(\omega, t)$ are possible (*dark blue fields* on Fig. 3.4) and the maximum of the function is shifted to $t = T_A/\pi$ (in our case ~ 2 fs).

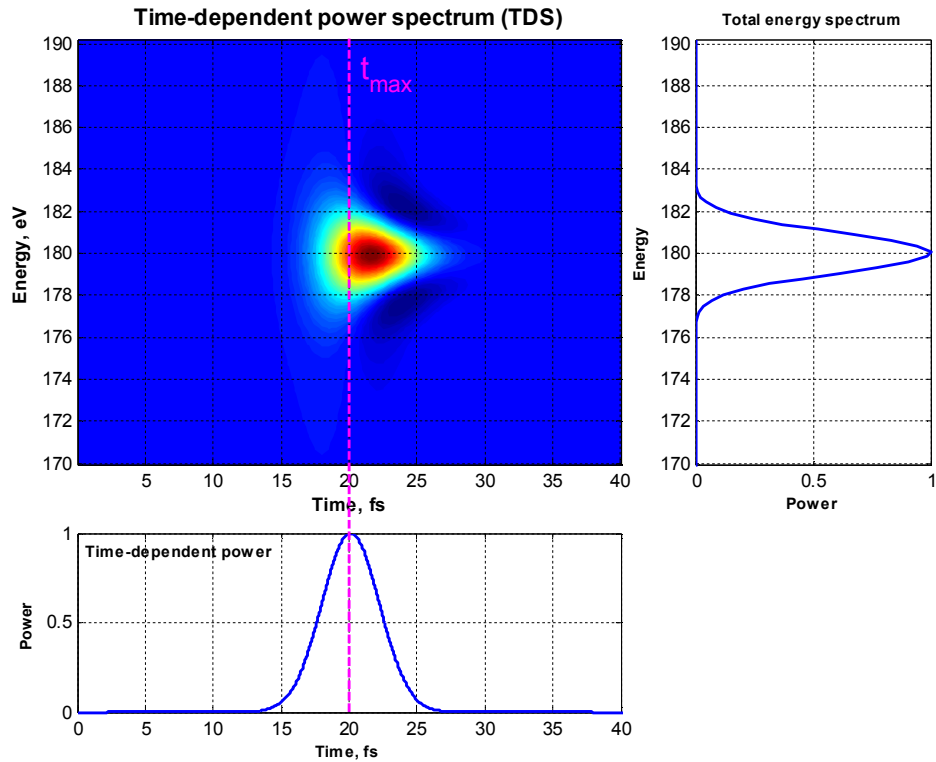


Fig. 3.4 The time-dependent spectrum of the a Gaussian bandwidth-limited pulse

In the second example, a train of two spikes with Gaussian profile was investigated. Both spikes have the same central frequency and are separated in time by 10 fs. In this case the TDS profile for 1st peak doesn't change, but the profile of the TDS function of 2nd peak changes due to the interaction from side of 1st spike (Fig. 3.5). If the distance between the peaks becomes large, the two independent profiles of the TDS function with temporal shift will be obtained where such of is similar to Fig. 3.4.

In the last example of the two spikes with the slightly different central frequencies and a small temporal shift is considered. This situation corresponds to a FLASH pulse which consists of few sub-pulses ("spikes") with slightly different frequencies. In this case, the TDS function shows a more featured profile (Fig. 3.6). The TDS function consists of two peaks (1 and 2 in Fig 3.6) with respect to two incident Gaussian spikes, and the profiles of both peaks are similar to profile of single spike (Fig. 3.4). Additionally there are special areas close to these peaks (*red* and *blue spots* on Fig. 3.5) describing the interaction between these pulses.

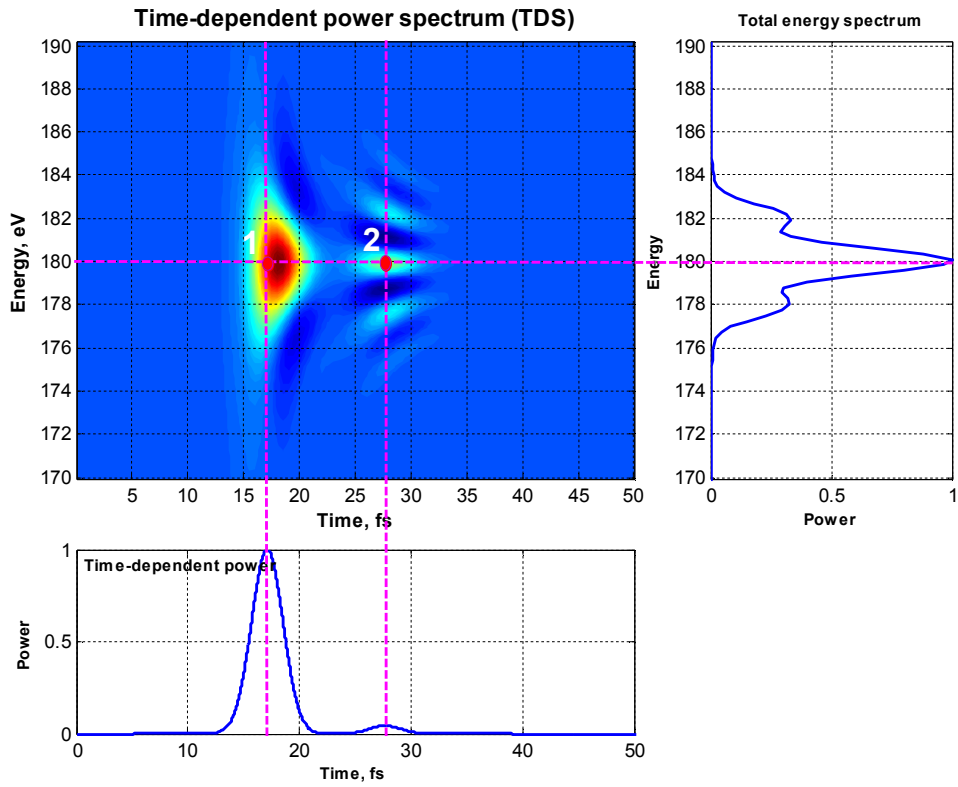


Fig. 3.5 The time-dependent spectrum of the combination of two Gaussian pulses with equal central frequency.

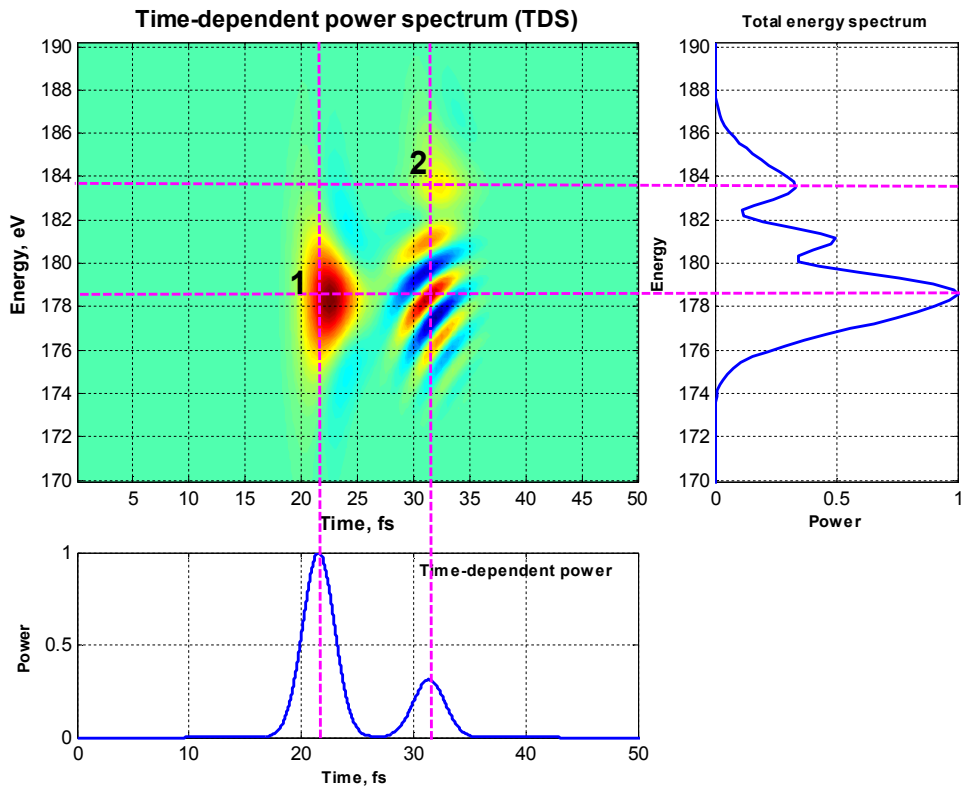


Fig.3.6 The time-dependent spectrum of the combination of two Gaussian pulses with different central frequencies.

3.3. Ultrafast processes

The extremely high photon densities of FEL radiation modify the scattering properties drastically, down to complete destruction [15, 40]. Significant changes may take place also during the pulse propagation. The FEL pulse is diffracted in an alternating media, due to the action of FEL radiation itself. Therefore, the situation can be described as an *intrinsic pump-probe* experiment since the same pulse serves as the pump and probe simultaneously.

Some understanding of the processes under investigation can be gained from fs- optical laser pump – fs X-ray probe experiments. Such experiments were performed intensively during last decade and provided unique information about atomic dynamic on natural atomic time scale [44, 45]. In work [45], the authors used the correlated and synchronized FEL pulses with separate optical lasers, to obtain the changes of the optical reflectivity in GaAs induced by femtosecond X-ray excitation

It is expected that induced by a FEL pulse a large number of core electrons become excited from the electronic ground state into excited states or vacuum. This instantaneous redistribution changes the optical properties of the material during the interaction with the FEL pulse due to the change of the (elastic) atomic form factors and (inelastic) X-ray absorption. A time depended X-ray atomic form factor within single and multiple electronic excitations followed by description of a highly ionized crystalline matter state within few femtoseconds are necessary to consider as well. At the same time, several kinds of fast electronic redistribution processes, such as Auger recombination and photoelectron excitations will appear within a time scale similar to the length of the FEL pulse. These processes will change the scattering behaviour of the matter without the change of the atomic sub-structure and will play an important role for description of FEL intensities below or close to the threshold of matter destruction.

3.3.1 Single atom scattering properties

In contrast to the optical range of wavelength, the energy of X-ray photon is high enough to perform one-photon ionization process producing ions in the core-hole state. The excited ions relax *via* Auger decay within tens of fs, the time comparable to the FEL pulse duration. The scattering properties of the atom depend on its state, which can be calculated on the basis of perturbation theory utilizing the corresponding cross-sections. The reason to use the perturbation theory is a minimization of the ponderomotive energy [46], which is inversely proportional to the square of the radiation frequency. The perturbation theory can be applied in the form of rate equations connecting the occupancies of atomic states under interest, the transition rates being dependent on the external field intensity and corresponding cross-sections [15, 47, and 48]. This approach described successfully the observed highly ionized states of the atom of xenon [46],

and on its basis several problems concerning FEL radiation were considered theoretically [47, 49].

3.3.2 Optical properties of solids

The interaction of the FEL pulse with solids is a complicated phenomenon [39, 51, 52]. The absorption of X-ray field takes place mainly due to bound-free (photoionization) and free-free transitions. At high fluencies almost all atoms become ionized with a core hole [50], and the photoelectrons together with valence electron form plasma with temperature up to tens of eV. The excited hollow ions recombine mainly *via* Auger process during time comparable with the pulse length, the yielding electrons with energies up to hundred of eV, leading the solid in the extreme regime of warm dense matter (WDM). After approximately a picosecond time, the electrons and ions start to thermalise. The opacities during the pulse propagation were calculated in [51, 39] based on plasma approach, the consequences of the calculation were in agreement with the experimental data. In [50] it was shown on the example of aluminum under 92.5 eV irradiation that for high fluencies, the saturable absorption takes place. After the electron is ejected from the L shell, the L edge is increased due to reduced screening and the absorption coefficient is heavily reduced. The theoretical calculations based on this scenario provided excellent agreement with the experiment.

In a series of works [53, 54], the problem of intense x-ray pulse propagation in the amorphous and periodic media was considered on the basis of two-level atom concept adopted from quantum optics and radiofrequency spin transitions [55, 56]. In this approach, the atom is considered to have two discrete levels with known transverse and longitudinal lifetimes and is described by the Bloch equations for the density matrix; the field is treated classically. The resultant so-called Maxwell-Bloch system of equations can be integrated analytically in some cases. In particular, the soliton-like solution is obtained for the Laue diffraction [53], Green function is found for small-area pulse propagation in a homogeneous media and self-induced transparency is predicted [54]. The application of such approach is strongly restricted to frequencies close to the transition to a discrete energy state, but in the X-ray domain the transitions to continuum take place, as a rule, and the two-level atom concept hardly can be generalized to deal with this case except for some exotic phenomena like resonant Auger effect [57]. In contrast to the optical properties (transmission and absorption) the behavior of coherent properties, leading to the Bragg diffraction, has not been considered and needs further investigations.

Chapter 4

Different approaches of X-ray reflection from multilayers

In last Chapter, I have demonstrated that the scattering properties of multilayer expected for low-intensive FLASH pulses can be compared with the ML reflectivity obtained with continuous radiation. Both can be described by the traditional methods. In this Chapter, several approaches of the calculation of reflectivity from the multilayer structures will be presented. All methods are based on the electromagnetic theory and Maxwell's equations, and present the solution of the wave equation.

By these methods one can solve these equations for different problems: for example, the calculation of reflectivity of MLs (*Parratt recursive method*, *slowly varying amplitude approximation*), the reconstruction of the electron profile of ML (*transfer matrix and the eigenwave methods*) and the interaction of time-dependent incident radiation with ML (*FDTD method*). In the latter case, the problem is partly discussed in the previous Chapter. All these methods are widely applied in practice and demonstrate good agreement with experiment using the continuous synchrotron radiation.

In the second part of this Chapter, a specific type of the multilayer structure will be described. Special attention will be paid on sliced multilayer grating structures (SMG), which combine the properties of a usual periodical multilayer with a grating structure. This structure has a high dispersion and light diffraction efficiency.

4.1. Reflectivity properties of the periodical multilayer X-ray mirrors

The reflection of the incident radiation at the boundary of two optically inhomogeneous media is the most widely used effect in optics. Various polarizers, focusing lenses, the interference instruments and coatings are applied in different field of science [58]. One of the widely used optical elements is the periodical multilayers. A ML (Fig. 4.1) is a stack of layers of (at least) two alternating materials of which one material has a low refractive index (high δ , *dark layers*) and the other material has a high refractive index (low δ , *white layers*).

From Fig. 4.1, the basic principles are evident: at each interface between the two materials a (small) part of the incoming radiation with wave vector \mathbf{k}_i is reflected in direction of wave vector \mathbf{k}_s , and the remaining part is transmitted. At the first interface (vacuum/ surface) *internal* reflection occurs. This is due to the fact that the refractive indices for X-rays of nearly all materials are below unity, which is in contrast to visible light. At the next interface (high δ / low δ) *external* reflection occurs. This also adds an additional phase shift of 180° to the reflected

radiation. By carefully the layer thicknesses selection of all the reflected radiation will add up in phase.

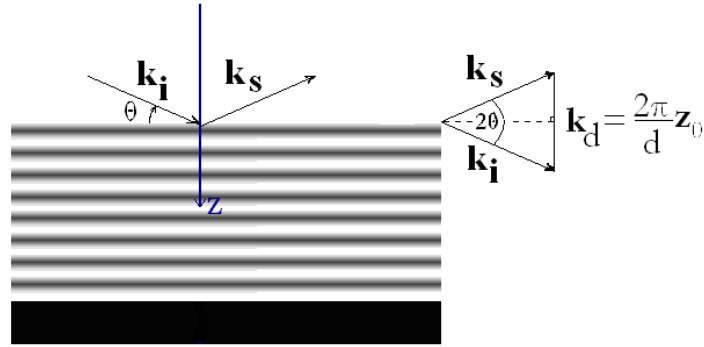


Fig. 4.1. Diffraction from a multilayer structure.

This is accomplished when the thickness d of each period (the combination of two layers) satisfies the Bragg equation:

$$m\lambda = 2dn_{eff} \sin \theta \quad (4.1)$$

where m is integer number representing the Bragg order.

From the Bragg equation it is also evident that a ML is a dispersive element: each wavelength is reflected at one particular angle only, for each Bragg order. However, this assumes an infinite number of periods, which is practically not feasible. As consequence of the limited number of periods, a specific wavelength is reflected within the small angular range $\Delta\theta$. Therefore, each mirror can be characterized using its reflectivity R and the angular selectivity $\theta/\Delta\theta$. Alternatively, one might also select a fixed angle, and look at the wavelength range $\Delta\lambda$ reflected at this angle. Then it can be expressed as a wavelength selectivity $\lambda/\Delta\lambda$. The reflectivity of a multilayer structure can be calculated using several theoretical models.

We will consider the structure of the multilayer composed on N repetitions of a single bilayer of thickness d formed from one layer of material A followed by another material B , as shown in Fig. 4.1. The layers are assumed be infinity perpendicular to the positive z axis. No assumption is made about the crystallographic detailed structure of A and B , so that the formulas are equal for both amorphous and crystalline materials: only matters of electron density contrast between the materials A and B .

4.1.1. Parratt recursive method

Let a plane monochromatic wave of X-rays be incident on the multilayer from vacuum (θ is the grazing angle, λ is the wavelength in vacuum) and has a wave vector \mathbf{k} in the plane (x, z) with positive k_x and k_z components (see Fig. 4.2). At the boundaries the plane wave is refracted and reflected. As a result two plane waves exit in each layer, a refracted and a reflected one. These waves have just the same k_x components of the wave vector in all the layers but the k_z components

have opposite signs in the two waves and, moreover, they differ from one layer to another. Thus, the vector of electric field in the layer with number j has the form:

$$E_j(x, z, t) = E(x, t) \left[E_j^i \exp(ik_j^z z) + E_j^r \exp(-ik_j^z z) \right] \quad (4.2)$$

where $E(x, t) = \exp(ik_x x - i\omega t)$, E_n^i and E_n^r are the amplitudes of refracted and reflected waves for the j^{th} layer (Fig. 4.2).

Each of them is the solution of the Maxwell's equations in a homogeneous medium with the refractive index $n_j = 1 - \delta_j + i\beta_j$. This equation determines the value of k_z as:

$$: \quad (k_j^z)^2 = (n_j k)^2 - k_x^2 = (1 - \delta_j + i\beta_j)^2 k^2 - k_x^2 \cong k_z^2 - 2\delta_j k^2 + i2\beta_j k^2 \quad (4.3)$$

where $k = \omega/c = 2\pi/\lambda$ is wave vector in vacuum. As follows from Eq. 4.3., k_z differs in various layers due to values of refractive index n_j .

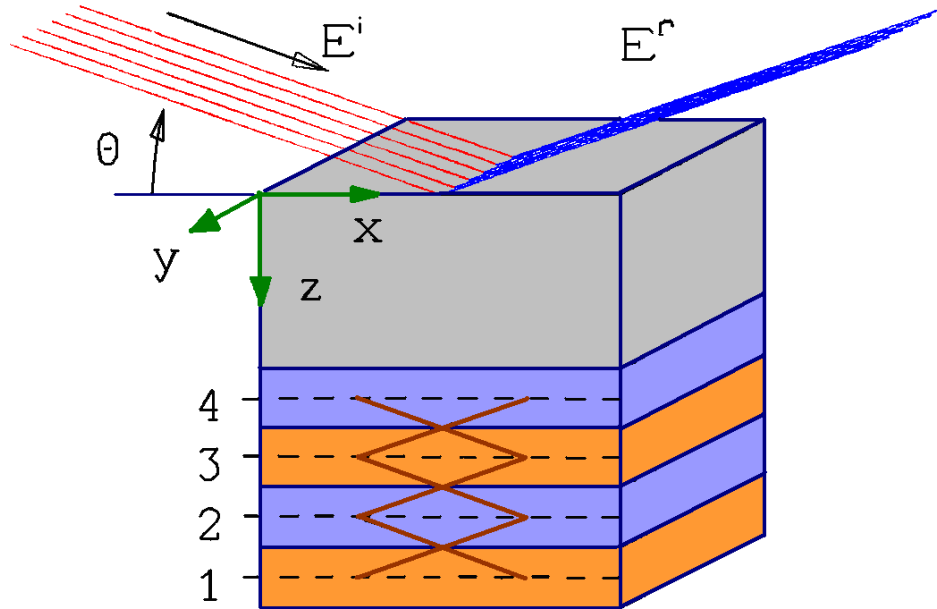


Fig. 4.2. Schematic of a multilayer which here is a stack of bilayer.

Maxwell's equation determines the wave vector only but not the wave amplitudes. They are determined by boundary conditions. In case of s -polarization the amplitudes E_n^i and E_n^r have only a y -component perpendicular to the scattering plane. The layers below will be numbered from the bottom of the structure to the top in the direction of the reflected wave (Fig. 4.2). The conditions of continuity for the electric and magnetic fields at the boundary between the layers with numbers 1 and 2 can be written as

$$\begin{aligned} E_2^i \exp\left(ik_2^z \frac{d_2}{2}\right) + E_2^r \exp\left(-ik_2^z \frac{d_2}{2}\right) &= E_1^i \exp\left(-ik_1^z \frac{d_1}{2}\right) + E_1^r \exp\left(ik_1^z \frac{d_1}{2}\right) \\ k_2^z \left\{ E_2^i \exp\left(ik_2^z \frac{d_2}{2}\right) - E_2^r \exp\left(-ik_2^z \frac{d_2}{2}\right) \right\} &= k_1^z \left\{ E_1^i \exp\left(-ik_1^z \frac{d_1}{2}\right) - E_1^r \exp\left(-ik_1^z \frac{d_1}{2}\right) \right\} \end{aligned} \quad (4.4)$$

where d_j are the thickness of the j -th layer, and the amplitudes in each layer are determined for the middle line of the layer. If the amplitudes E_2^i and E_1^r are known, the amplitudes E_1^i and E_2^r can be derived. The solution of this problem can be written in the form

$$\begin{aligned} E_2^r &= r_{22}^{(1)} E_2^i + t_{21} E_1^r \\ E_1^i &= t_{12} E_2^i + r_{11}^{(2)} E_1^r \end{aligned} \quad (4.5)$$

where

$$\begin{cases} r_{22}^{(1)} = \frac{k_2^z - k_1^z}{k_2^z + k_1^z} \left[\exp\left(ik_2^z \frac{d_2}{2}\right) \right]^2 \\ r_{11}^{(2)} = \frac{k_1^z - k_2^z}{k_2^z + k_1^z} \left[\exp\left(ik_1^z \frac{d_1}{2}\right) \right]^2 \\ t_{12} = \frac{2k_2^z}{k_2^z + k_1^z} \left[\exp\left(ik_2^z \frac{d_2}{2}\right) \right] \left[\exp\left(ik_1^z \frac{d_1}{2}\right) \right] \\ t_{21} = \frac{2k_1^z}{k_2^z + k_1^z} \left[\exp\left(ik_2^z \frac{d_2}{2}\right) \right] \left[\exp\left(ik_1^z \frac{d_1}{2}\right) \right] \end{cases} \quad (4.6)$$

The wave propagation in the substrate ($j=0$) can also be presented in such a form by setting $d_0=0$ and $E_0^r=0$. It means that in the substrate there are only inward-propagating waves. Now this approach should be expanded to any layer to obtain the recurrence relations:

$$\begin{cases} E_j^i + E_j^r & E_{j-1}^i \exp(-ik_{j-1}^z d_{j-1}) + E_{j-1}^r \exp(ik_{j-1}^z d_{j-1}) \\ k_j^z (E_j^i - E_j^r) & k_{j-1}^z [E_{j-1}^i \exp(-ik_{j-1}^z d_{j-1}) - E_{j-1}^r \exp(ik_{j-1}^z d_{j-1})] \\ E_0^r & = 0 \end{cases} \quad (4.7)$$

The recurrence relations describe completely the process of the electromagnetic wave reflection and transmission from multilayer structures. The relations (4.7) can be expressed using the reflection and transmission factors r_j and t_j :

$$r_j = \frac{E_j^r}{E_j^i}; \quad t_j = \frac{E_{j-1}^i}{E_j^i} \quad (4.8)$$

The recursive relations for r_j and t_j are derived directly from (4.7) and (4.8)

$$\begin{cases} r_j = \frac{r_j^F + r_{j-1} \exp(2ik_{j-1}^z d_{j-1})}{1 + r_j^F r_{j-1} \exp(2ik_{j-1}^z d_{j-1})} \\ r_0 = 0 \\ t_j = \frac{t_j^F t_{j-1} \exp(ik_{j-1}^z d_{j-1})}{1 + r_j^F r_{j-1} \exp(2ik_{j-1}^z d_{j-1})} \\ t_0 = 1 \end{cases} \quad (4.9)$$

The quantities r_j^F and t_j^F in (4.9) are the amplitudes of the reflection and transmission factors at the j -th interface defined by the Fresnel formulas:

$$\begin{cases} r_j^F = \frac{k_j^z - k_{j-1}^z}{k_j^z + k_{j-1}^z} \\ t_j^F = \frac{2k_j^z}{k_j^z + k_{j-1}^z} \end{cases} \quad (4.10)$$

If the structure consists of one layer, the Eq. (4.9) transform into the well-known expressions for the single-film reflectivity and transmittance [2, 58]. In the case of π -polarization radiation it is convenient to consider the magnetic field instead of the electric one.

The recurrence procedure (4.9) starts from the substrate side ($j=0$), the values of r_0 and t_0 at the interfaces are calculated consecutively, and the reflectivity R and transmissivity T for the entire multilayer are, evidently, equal to

$$\begin{cases} R = |r_N|^2 \\ T = |t_N|^2 \operatorname{Re} \left\{ \frac{k_0^z}{k_0^z \sin \theta} \right\} \end{cases} \quad (4.11)$$

Thus, Eqs. 4.9-4.11 allow solve numerically the problem of reflection of an electromagnetic wave from an arbitrary multilayer structure (including non-periodic structures) for any wavelength λ of the incident radiation and any incident angle θ .

4.1.2. Transfer matrix method

The transfer-matrix method (TMM) is a method used in optics to analyze the propagation of the electromagnetic field through a stratified layered medium. This is, for example, relevant for the design of anti-reflective coatings and dielectric mirrors. For structures not consisting of discrete layers (e.g. diffuse boundaries) exact solutions cannot be calculated and the structures have to be approximated by a series of small layers having sharp boundaries. A good approximation might require more than one hundred layers per period, which makes the calculation much complex time consuming. In this case, the TMM [58], a variant on the recursive method, has proven to be much easier to use, because it takes full advantage of the periodic structure of a multilayer.

The reflection of light from a single interface between two media is described by the Fresnel equations. The TMM is based on the fact that, according to Maxwell's equations, there are simple continuity conditions for the electric field across the boundaries from one medium to the next one. If the field is known at the beginning of the layer, the field at the end of the layer can be derived from a simple matrix operation. Then a stack of layers can be represented as a

system matrix, which is the product of a individual layer matrices. The final step of the method involves converting the system matrix back into the reflection and transmission coefficients.

Eqs. 4.7 constitute a linear transformation of discrete variables, i.e., the amplitudes E_j^i and E_j^r may be rewritten in the form of an equivalent matrix expression:

$$\begin{pmatrix} E_j^i \\ E_j^r \end{pmatrix} = a_j S_j \begin{pmatrix} E_{j-1}^i \\ E_{j-1}^r \end{pmatrix}. \quad (4.12)$$

Here S_j is a 2x2 *transfer* matrix with $\det S=1$ and a_j is a scalar

$$S_j = \begin{vmatrix} \left(1 - (r_j^F)^2\right)^{-1/2} \exp(ik_j^z d_j) & r_j^F \left(1 - (r_j^F)^2\right)^{-1/2} \exp(-ik_j^z d_j) \\ r_j^F \left(1 - (r_j^F)^2\right)^{-1/2} \exp(-ik_j^z d_j) & \left(1 - (r_j^F)^2\right)^{-1/2} \exp(ik_j^z d_j) \end{vmatrix} \quad (4.13)$$

$$a_j = \frac{\left(1 - (r_j^F)^2\right)^{-1/2}}{t_j^F} = \sqrt{\frac{k_{j-1}^z}{k_j^z}}$$

By consecutively application of expression (4.12), the relation between the amplitudes of incident wave reflected from the multilayer and the wave that travel into substance are

$$\begin{pmatrix} E_N^i \\ E_N^r \end{pmatrix} = \left\{ \prod_{j=0}^N a_j \right\} \left\{ \prod_{j=0}^N S_j \right\} \begin{pmatrix} E_0^i \\ 0 \end{pmatrix}. \quad (4.14)$$

In terms of the elements of the transfer matrix S (see Eq. 4.13) and using Eq. 4.14, the reflectivity and transmittivity can be written in the following form:

$$R = \left| \frac{s_{21}}{s_{11}} \right|^2, \quad T = \frac{1}{|s_{11}|^2} \operatorname{Re}(k_0^z) |k_0^z|^{-1}. \quad (4.15)$$

Eqs. 4.13-4.15 are completely equivalent to the Eqs. 4.9-4.11. The TMM is a very useful algorithm and appropriate for reflectivity and transmission calculations of any multilayer structures. This method is applicable for either real or complex refractive index and can handle a large number of layers in a multilayer structure. In addition, these layers can be ordered in arbitrary manner and there is no requirement that they should be periodic. Even if they are periodic, the repetition unit must not be composed of two layers only, but of any number of layers. There is also no restriction on the thickness of any layer. The thickness and the refractive index of each layer can be defined independently. This makes the TMM most suitable for modelling structures formed by different periodic multilayers stacked together, even if they are not fully periodic. This approach can handle structures having a high index contrast between

their two composite materials. This makes the TMM suitable for modelling multilayer structures, which usually have a high index contrast between their composite materials.

The TMM has also some drawbacks. For example, it assumes that a plane perpendicular to the direction of propagation is infinite, meaning that each layer in a multilayer structure extends infinitely in both directions. Of course, this is unrealistic, so the layers of the sample have to be sufficiently wide to avoid errors from this assumption. The TMM calculates the field throughout the structure by propagating it from one layer to the other by matrix relations. The resolution depends greatly on the computational speed. A mathematical expression is missing that can relate the field between multiple layers, which would reduce the mathematical calculations required and, consequently, the computational time.

Another drawback of the TMM is that it is limited to continuous wave propagation and can not handle pulse propagation. To model pulses, the TMM must be combined with the Fourier Transform. Therefore, modelling of a pulse structure of incident beam requires other techniques such as the Finite Difference Time Domain (FDTD) method.

4.1.3. Finite Difference Time Domain method

The FDTD method is a popular technique for modelling problems of electrodynamics (see, for example, [59-61]). In general, this approach belongs to the class of *grid-based differential time-domain numerical modelling methods* and describes the interaction of different electromagnetic waves (such as a monochromatic plane wave or ultra-short pulse) with a frequency-dependent layered media. The time-dependent Maxwell's equations (in partial differential form) are discretized using the standard central-difference approximations to the space and time partial derivatives:

$$\begin{aligned} \frac{E_x^{n+1/2}(k) - E_x^{n-1/2}(k)}{\Delta t} &= -\frac{1}{\epsilon_0} \frac{H_y^{n+1}(k+1/2) - H_y^n(k-1/2)}{\Delta x} \\ \frac{H_y^{n+1}(k+1/2) - H_y^n(k+1/2)}{\Delta t} &= -\frac{1}{\mu_0} \frac{E_x^{n+1/2}(k+1) - E_x^{n+1/2}(k)}{\Delta x} \end{aligned} \quad (4.16)$$

For simulation in one-dimensional free space case, the time is specified by the superscripts, i.e., “ n ” actually means a time $t = \Delta t \cdot n$. The term “ $n+1$ ” means one step later in time. The terms in parentheses represent a distance, i.e., “ k ” actually means the distance $z = \Delta x \cdot k$. The approach assumes that the \mathbf{E} and \mathbf{H} fields are interleaved in both space and time. For the \mathbf{H} field are use the arguments “ $k+1/2$ ” and “ $k-1/2$ ” to indicate that the \mathbf{H} field values are located between the \mathbf{E} field values. Similarly, the “ $n+1/2$ ” or “ $n-1/2$ ” superscript indicates that it occurs slightly after or before n , respectively.

Eq. (4.16) can be rearranged by an iterative algorithm

$$\begin{aligned}
E_x^{n+1/2}(k) &= E_x^{n-1/2}(k) - \frac{\Delta t}{\varepsilon_0 \Delta x} \left[H_y^{n+1}(k+1/2) - H_y^n(k-1/2) \right] \\
H_y^{n+1}(k+1/2) &= H_y^n(k+1/2) - \frac{\Delta t}{\mu_0 \Delta x} \left[E_x^{n+1/2}(k+1) - E_x^{n+1/2}(k) \right].
\end{aligned} \tag{4.17}$$

Notice that the calculations are interleaved in both space and time. In Eq. (4.17), for example, the new value of E_x is calculated from the previous of E_x and the most recent values of H_y . This is the fundamental paradigm of the FDTD method.

Now we can examine more complex case – the distribution EM wave inside the frequency-dependent materials. For example, many materials show a strong frequency-dependence of optical properties in soft X-ray range. Now we can write the Maxwell equations in more general form

$$\begin{aligned}
\frac{\partial D}{\partial t} &= \nabla \times H \\
D(\omega) &= \varepsilon_0 \varepsilon^*(\omega) E(\omega) \\
\frac{\partial H}{\partial t} &= -\frac{1}{\mu_0} \nabla \times E,
\end{aligned} \tag{4.18}$$

where D is the electric flux density. Notice that Eq. 4.18 is written in the frequency domain. The next step is to transform these equations and the frequency-dependent dielectrical constant of medium into the time domain using (i) inverse Fourier transform (inverse task of Eq 2.3) (ii) in case of complex form of dielectric constant, the *Z-transform* (a discrete equivalent of the *Laplace transform*, see *Appendix C*). About the first case, we can use the analogous approach described in the previous chapter, but transform to time domain. In second case, we transform into a complex frequency-domain (*Z-domain*). For example, we have the problem of calculating E in a resonant media described by Debye model:

$$D(\omega) = \left(\varepsilon_r + \frac{\sigma}{j\omega\varepsilon_0} + \frac{\chi_1}{1 + j\omega t_0} \right) E(\omega). \tag{4.19}$$

We use the *Z-domain* to avoid problems with the convolution integrals in the time domain:

$$D(z) = \varepsilon_r E(z) + \frac{\sigma \cdot \Delta t / \varepsilon_0}{1 - z^{-1}} E(z) + \frac{\chi_1 \cdot \Delta t / t_0}{1 + z^{-1}} E(z). \tag{4.20}$$

Other equations from Eq. 4.18 also should be transformed into the *Z domain*, and finally, we can describe the distribution of EM wave inside frequency-depend medium. Various types of frequency-depend media were described in literature (for example, [60]).

The basic FDTD space grid and time-stepping algorithm was developed by Kane Yee (1966) [62]. Since about 1990, FDTD techniques have emerged as a computational model for

many scientific and engineering problems dealing with the interactions of EM wave with various structures. Current FDTD modelling applications range from near-DC (ultralow-frequency geophysics involving the entire Earth-ionosphere waveguide) through microwaves (radar signature technology, antennas, wireless communications devices, digital interconnects, biomedical imaging/treatment) to visible and VUV range (photonic crystals, nanoplasmonics, solitons, and biophotonics). But, there is a limit of the simulation due to the interconnection relation of time- with space meshes, well-known as *the Courant–Friedrichs–Lewy (CFL) condition*:

$$\frac{c \cdot \Delta t}{\Delta x} \leq C, \quad (4.21)$$

where the constant C depends on the particular equation to be solved and not on Δt and Δx , and c is speed of light. From CFL condition (Eq. 4.21), for case the interaction of FLASH pulse with layered structures (the duration of pulse is ~ 10 fs, and the size of ML is ~ 100 nm), the mesh size Δx is chosen $\sim \text{\AA}$ and the time step, Δt must be few *as*. In result, the FDTD method can be applied to describe the interaction of fs pulses with nm-objects in 1D or 2D space, if we have information about time- and frequency dependent reflectivity of these objects.

4.1.4. Slowly varying amplitude approximation (SVA)

The propagation of incident plane wave in multilayer structure is based by the coupled-wave equations, derived from Maxwell's equations. The coupled-wave equations describing optical parametric amplification are usually solved in the slowly varying amplitude (SVA) approximation, in which the second-order derivatives of the amplitudes are ignored and the effects at the exit face of the medium are not considered.

In order to determine the EM wave within the ML and the reflectivity and transmittance, one should solve a wave equation which, in the case of *s*-polarization, has the form

$$\frac{d^2 E(z)}{dz^2} + k^2 (\varepsilon(z) - \sin^2 \varphi) E(z) = 0, \quad (4.22)$$

where $k = \omega/c = 2\pi/\lambda$ is the wave numbers in vacuum; $\varepsilon(z) = 1$ at $z < 0$; $\varepsilon(z)$ is permittivity and $\varepsilon(z) = \varepsilon_{sub}$ at $z > L$, where ε_{sub} is permittivity of the substrate; L is thickness of multilayer structure and is equal Nd ; N is the numbers periods of multilayer, d is the thickness of a period and φ is incident angle. The behaviour of permittivity $\varepsilon(z)$ at $0 \leq z \leq L$ is shown in Fig. 4.3.

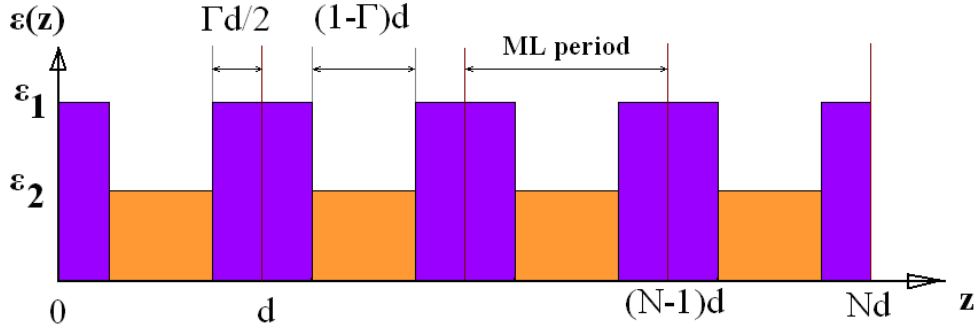


Fig. 4.3. A two-component periodical multilayer mirror with N periods. d and Γ are period and thickness ratio of multilayer, respectively.

In this approach the permittivity $\varepsilon(z)$ expands into a Fourier series. Expansion of the function $\varepsilon(z)$ into solely cosine terms implies that the function is even, i.e., one assumes that at the multilayer surface there is a material layer of half thickness compared to that in bulk as shown in Fig. 4.3.

$$\varepsilon(z) = \varepsilon_0 + \sum_{j=1}^{\infty} 2(\varepsilon_1 - \varepsilon_2) \frac{\sin(\pi j \Gamma)}{\pi j} \cos\left(\frac{2\pi j z}{d}\right), \quad 0 \leq z \leq L \quad (4.23)$$

where $\varepsilon_0 = \Gamma \varepsilon_1 + (1 - \Gamma) \varepsilon_2$ is the permittivity averaged over the period.

In general case, where the function $\varepsilon(z)$ contains sine and cosine terms the reflected and transmitted waves are changed by an additional phase shift amplitudes. However, the intensity of the reflection and transmission remain unchanged.

The wave field inside the multilayer can be presented in the form (the case of the two strong waves)

$$E(z) = f_0(z) \exp(i\pi j z / d) + f_m(z) \exp(-i\pi j z / d), \quad 0 \leq z \leq L. \quad (4.24)$$

The wave equation (4.22) can be rewritten to coupled equations using the Eqs. (4.23) and (4.24), for the amplitudes of electromagnetic waves f_0 and f_m as

$$\begin{cases} \left[\frac{d^2 f_0}{dz^2} + \frac{i2\pi j}{d} \frac{df_0}{dz} + k^2 \left(\varepsilon_0 - \sin^2 \varphi - \frac{\pi^2 j^2}{k^2 d^2} \right) \right] f_0 & -k^2 (\varepsilon_1 - \varepsilon_2) \frac{\sin(\pi j \Gamma)}{\pi j} f_m + \Delta F(z) \\ \left[\frac{d^2 f_m}{dz^2} + \frac{i2\pi j}{d} \frac{df_m}{dz} + k^2 \left(\varepsilon_0 - \sin^2 \varphi - \frac{\pi^2 j^2}{k^2 d^2} \right) \right] f_m & -k^2 (\varepsilon_1 - \varepsilon_2) \frac{\sin(\pi j \Gamma)}{\pi j} f_0 + \Delta F(z) \end{cases} \quad (4.25)$$

where $\Delta F(z)$ represents the sum of rapidly oscillating functions with periods d/l ($l=1,2,\dots$). In the case of resonant interaction of the incident wave with the multilayer, the amplitudes $f_{0,m}$ are slowly oscillating functions, and the second derivatives in the Eq. (4.25) can be ignored. Also, the rapidly oscillating term $\Delta F(z)$ on the right-side of these equations may be discarded (formally, these equations may be averaged over the period). Eq. (4.25) is rewritten using this approximation as

$$\begin{cases} \frac{i2\pi j}{d} \frac{df_0}{dz} + k^2 \left(\varepsilon_0 - \sin^2 \varphi - \frac{\pi^2 j^2}{k^2 d^2} \right) f_0 & -k^2 (\varepsilon_1 - \varepsilon_2) \frac{\sin(\pi j \Gamma)}{\pi j} f_m \\ \frac{i2\pi j}{d} \frac{df_m}{dz} + k^2 \left(\varepsilon_0 - \sin^2 \varphi - \frac{\pi^2 j^2}{k^2 d^2} \right) f_m & -k^2 (\varepsilon_1 - \varepsilon_2) \frac{\sin(\pi j \Gamma)}{\pi j} f_0. \end{cases} \quad (4.26)$$

The boundary conditions are

$$\begin{cases} f_0(0) = 1 \\ f_m(L) = 0 \end{cases} \quad (4.27)$$

The first condition of the Eq. (4.28) means that a wave with amplitude of unity incident on the multilayer; and a second condition shows that there is a reflected wave in the substrate propagating inward only. The reflectivity and transmittance are expressed in terms of solution of Eqs. (4.26) and (4.27) as

$$\begin{aligned} R &= |f_m(0)|^2 \\ T &= |f_0(L)|^2. \end{aligned} \quad (4.28)$$

The Eqs. (4.26) with boundary conditions Eq. (4.27) are a set of first-order differential equations with constant coefficients and can be solved by a conventional methods (see, *Finite Element Method*) [63, 64]. This approach is a numerical technique for finding approximate solutions of partial differential equations (PDE) as well as of integral equations. The solution approach is based either on eliminating the differential equation completely (steady state problems), or rendering the PDE into an approximating system of ordinary differential equations, which are then numerically integrated using standard techniques such as *Euler's method*, *Runge-Kutta*, etc [65].

4.1.5. Analytical method by eigenwaves

One of the methods of the calculation of the X-ray reflection and diffraction from periodical multilayers is based on the possibility to express the *Bloch eigenwaves* of one-dimensional periodical infinite ML through the solutions of X-ray scattering problem within the single basic element composing the ML period [66]. For ML with a limited number of periods, these Bloch eigenwaves can further be used along with the boundary conditions for the whole layer stack. This result can be presented by an analytical expression for the EM field and integral reflection coefficient at any point of the sample, without the need to address the recurrent equations. This approach was named as a ‘‘method of eigenwaves’’ (MEW). This approach develops the TMM expressing the total reflection coefficient in analytical form, and reduces the calculation time in comparison with the direct solution of Parratt’s recursive equations.

In the work of I. D. Feranchuk *et al* [66] the analytical solution for the reflectivity of a ML was proposed, which is the analytical solution of the recursive Parratt's equations (see, Eqs. 4.9-4.11). However, the computer time required for these both simulations are essentially different, especially when the number of multilayer periods is large. The numerical solution of the Parratt's equations involves $\approx 4^{N+1}$ operations, which increases the simulation time exponentially. On the other side, the time to calculate reflectivity using the MEW approach increases as a power law with increasing N. This advantage of MEW is even more pronounced for the experimental data fitting routines, which requires simulation of the X-ray reflectivity many times during the trial-and-error procedure.

This method also delivers the analytical expression for wave fields in all layers of the ML without solving of recurrent equations. This is essential in the cases when the wave fields are used to calculate the matrix elements of perturbation operator. For example, these wave fields can be used for simulation of diffusely scattered X-ray intensity by means of the distorted-wave Born approximation.

4.2. Approach for sliced multilayer gratings

One of the important applications of modern X-ray optics is X-ray spectroscopy, which requires spectral optical elements with high dispersion and high diffracting efficiency. In spite of the obvious progress in technology, the holographic and multilayer coated gratings are still restricted. One of the perspective multilayer structures, containing the properties of the grating and the periodical multilayer is *the sliced multilayer grating* (SMG) (Fig. 4.4), also known as a *lamellar multilayer amplitude grating* (LMAG), which can be fabricated by cutting the multilayer structures by a certain angle, as the solution of this problem [67-70].

From multilayers the SMG inherit the high diffraction efficiency in the resonant order and very short periods lead to a high angular dispersion. These remarkable dispersion properties of the SMG allow the development of compact spectrometers and polarimeters, which may be useful in plasma spectroscopy, astrophysics, material science and biology. These structures can be fabricated by polishing the MLs at an angle α (*sliced angle*). This has the additional advantage that the surface grating appears in addition to the strong Bragg reflection. Whereas the Bragg reflection probes the bulk scattering of the ML, the grating peaks are created by scattering at the surface relief.

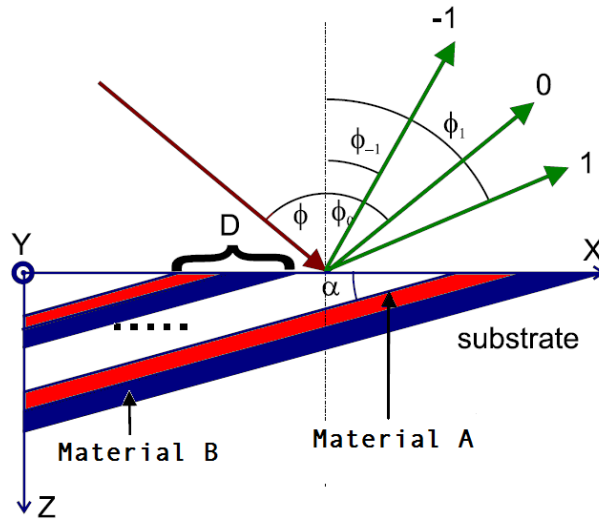


Fig 4.4. The scheme of a SMG, where α is slicing angle, D is grating period.

Any SMG obey the same general principles as usual grating. To determine the angles of diffraction orders, the usual grating equation [70, 71] can be used

$$D(\sin \varphi_n - \sin \varphi) = n\lambda, \quad n=0, \pm 1, \pm 2, \dots, \quad (4.29)$$

where λ is wavelength, φ is an incident angle to normal, φ_n are diffraction angles, and D is grating period. However, the SMG can be considered from different points of view. Since, the SMG is based on multilayer coatings one can expect that the maximum of diffraction efficiency should appear, when the resonant Bragg condition is satisfied. In terms of SMG (Fig. 4.4) it can be written as

$$2d \cos(\varphi - \alpha) = m\lambda, \quad m=0, \pm 1, \pm 2, \dots, \quad (4.30)$$

where d is the multilayer period and α is sliced angle. The beam specularly reflected from the layers has evidently the angle (“blaze condition”)

$$\varphi_m + \alpha = \varphi - \alpha. \quad (4.31)$$

In the work of A. Sammar *et. al.* [67], it was shown, that the scattering intensity of the these structures in so-called kinematical theory can be written as

$$I(\theta_z) = \left(\frac{\sin^2(N_g \theta_x D / 2)}{\sin^2(\theta_x D / 2)} \right) \left(\frac{\sin^2(\theta_x D / 2)}{(\theta_x D / 2)^2} \right) \left(\frac{\sin^2(N_{SML} \theta_z d / 2)}{\sin^2(\theta_z d / 2)} \right) |F_d(\theta_z)|^2 \quad (4.32)$$

with,

$$\theta_x = \frac{2\pi}{\lambda} (\sin \varphi_n - \sin \varphi) \quad (4.33)$$

and for the reflection case

$$\theta_z = \frac{2\pi}{\lambda} (\cos \varphi_n + \cos \varphi). \quad (4.34)$$

N_{SMG} is the number of bilayers in the stack, and N_g the number of illuminated grating periods.

If a multilayer consists from two materials: material A with dielectric constant ε_A and thickness d_A , and material B with dielectric constant ε_B and thickness d_B :

$$F_d(\theta_z) = k^2 \left[\varepsilon_A \frac{\exp(i\theta_z \gamma d) - 1}{i\theta_z} + \exp(i\theta_z \gamma d) \varepsilon_A \frac{\exp(i\theta_z (1-\gamma)d) - 1}{i\theta_z} \right] \quad (4.35)$$

where γ is the ratio of the thicknesses.

By combining Eqs. (4.29) and (4.30), it yields the Bragg condition for the SMG [67]:

$$m\lambda = d \sin \varphi \left[1 + \sqrt{1 - 2 \frac{\cos \varphi}{\sin^2 \varphi} \frac{\lambda n}{D} - \frac{1}{\sin^2 \varphi} \left(\frac{\lambda n}{D} \right)^2} \right] \quad (4.36)$$

For the accurate calculation of the diffraction pattern, and in particular for the diffraction efficiencies, the wave equation in SMG can be solved in the SVA approximation described above for usual periodical structures. The numerical solution in the multi-wave approximation was described in the work of R.M. Fechtchenko *et. al.* [69]. On the other hand, the theory of reflection and transmission of the SMGs in an approximation of two strong waves was considered in [70]. As a result, the amplitudes of reflected waves into the zero and m th orders can be obtained if the diffracted wave of the m th order was neglected that propagates into a multilayer

$$R_m \cong \frac{2 \cos \varphi \varepsilon_m}{(\kappa_0 + \cos \varphi) \left((\kappa_0 - \alpha)^2 - \kappa_m^2 \right)} \quad (4.37)$$

$$R_0 \cong -\frac{\kappa_0 - \cos \varphi}{\kappa_0 + \cos \varphi}$$

where

$$\kappa_m^2 = 1 - \left(\sin \varphi - \lambda m / d \right)^2 + \varepsilon_0(z). \quad (4.38)$$

In soft X-ray range, the dielectric constants can be described as $1 + \varepsilon_1$ and $1 + \varepsilon_2$, then each values may be expanded in a Fourier series, which inside SMG are:

$$\varepsilon(x, z) = \sum_{n=-\infty}^{+\infty} \{1 + \varepsilon_m(z)\} \exp(inx2\pi / D) \quad (4.39)$$

when

$$\begin{aligned} \epsilon_m(z) &= (\epsilon_1 - \epsilon_2) \frac{\sin(\pi\gamma n)}{\pi n} \exp(i z n 2\pi \cos \alpha), n \neq 0 \\ \epsilon_0(z) &= \gamma \epsilon_1 + (1 - \gamma) \epsilon_2 \end{aligned} \quad (4.40)$$

The theoretical and first experimental results [70-72] have shown that SMG can be used to construct the X-ray spectrometers with high dispersion and diffraction efficiency. In spite of relatively narrow spectral band SMG can be useful when one need to resolve many spectral lines crowded in a narrow spectral range. Such structures can be applied in a wide wavelength range.

Summarize, the application of multilayer structures for the construction of different components of the X-ray optical device has become more and more frequent. For the X-ray optics, these structures consist of alternating layers of high and low atomic number elements. There are different methods to calculate the various properties of such structures: the reflectivity and transmittance of MLs, the reconstruction of the electron profile, the interaction of time-dependent incident radiation with ML. These approaches are widely applied in practice and demonstrate good agreement with experiment using the continuous synchrotron radiation.

Chapter 5

Optical properties of boron carbide

Since, the changes in the optical properties of the material in the process of interaction with the high intensity ultra short FEL pulse easier to detect in the light elements, the boron carbide is a promising candidate for our investigations in the soft X-ray range. *Boron carbide* is the hexagonal phase of the composition $B_{15-x}C_x$, better known as the B_4C (other names: *tetrabor* or *black diamond*). This material contains two low Z-elements (boron ($Z=5$) and carbon ($Z=6$)).

In this Chapter, the optical properties of boron carbide material inside the periodical multilayer structure will be analyzed near the K-edges using the obtained experimental data for the continuous X-ray radiation.

5.1. Boron carbide

In the past 20 years, the B_4C films with thicknesses ranging from a fraction of a nanometer to several nanometers have been put into practice as the constituent layers and the interface barrier layers in reflective multilayer optics working at photon energies from a few tens of eV in the EUV region to hundreds of keV in the hard X-ray region. Such optical devices are used in various fields of physics, such as solar physics, synchrotron radiation, EUV lithography, and the X-ray astronomy. The use of single-layer B_4C films as reflective elements in the EUV region was first explored by Blumenstock *et al.* [73]. The B_4C is a perspective candidate to use in the manufacture of X-ray mirrors of the FEL facilities in range of less 2keV.

Boron carbide crystals are the phases of variable compositions, therefore, its properties depend on many respects on the component ratio. There are several known polymorphs of boron carbide. The *tetragonal* ($B_{50}C_2$, $B_{50}C$, $B_{48}C_3$, $B_{51}C$, and $B_{49}C_3$) and *orthorhombic* (B_8C) phases are metastable and are of no practical interest [74, 75]. The most stable and, therefore, widely used boron carbide polymorph is a *hexagonal phase* of composition $B_{15-x}C_x$, better known as B_4C at $x = 3$.

The chemical composition of the icosahedron and the linear group has been debated for many years. In earlier studies [76] the structure of boron carbide led to the proposal that carbon-rich compositions of the material are composed of B_{12} icosahedra linked together with C-C-C chains. Therefore, boron carbide crystals were assigned the composition $B_{12}C_3$ (or B_4C). An experimental determination of the atomic structure of B_4C is still lacking due to (i) neutron diffraction cannot distinguish B from C because their scattering lengths are too close; (ii) X-ray diffraction has allowed the identification of a C-B-C chain, but the location of the remaining C atom in the $B_{11}C$ icosahedron remains unsettled because the X-ray form factors of boron and carbon atoms are also too close.

Later, nuclear magnetic resonance (NMR) measurements showed that the linear group contains one or two boron atoms; i.e., its composition is B-B-C or C-B-C [77]. In this case, the carbon atoms should be incorporated in the icosahedra, and their composition can change from $B_{11}C$ to $B_{10}C_2$ [78, 79] (Fig. 5.1). Thus, the change in the structure of boron carbide crystals is accompanied by the substitution of carbon for boron in both linear chains and the icosahedra.

Although the stoichiometric compound is nominally B_4C , the boron to carbon ratio can vary over a broad range by partial substitution of B by C atoms both in the C-B-C chains and in the icosahedra. From the viewpoint of electronic structure (Fig. 5.2), boron carbide is a semiconductor with a gap dependent on the boron to carbon stoichiometry that can be modified continuously from ~ 0.8 eV (carbon-rich) to ~ 2 eV (boron-rich) [80, 81]. In the work [82] the authors shown that the two compounds $B_{12}(CBC)$ and $B_{11}C(CBC)$ with a C-B-C intericosahedral chain are more stable. Other B_{12} -based compounds have also attracted considerable interest because of their unique combination of structures and properties. The full structural formula of boron carbide is $(B_{12})_x(B_{11}C)_{1-x}(CBC)_m(CBB)_n(CCC)_o(B\Box B)_p$ (\Box -vacancy; $m+n+o+p = 1$; for $B_{4.3}C$, $o, p = 0$) [82, 83].

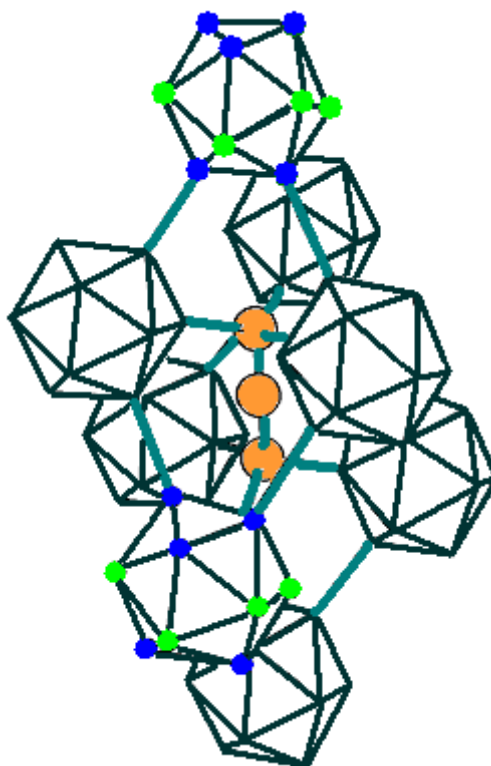


Fig.5.1 Atomic structure of boron carbide. The boron atoms (*green circles*) are the *equatorial sites*. The atoms (*blue circles*) are the *polar sites*, bonded to neighboring icosahedra. The orange atoms (*large circles*) form the chain. In $B_{12}C_3$ the atoms in the chain are C-B-C and the icosahedra are $B_{11}C$ with the carbon placed in a polar site.

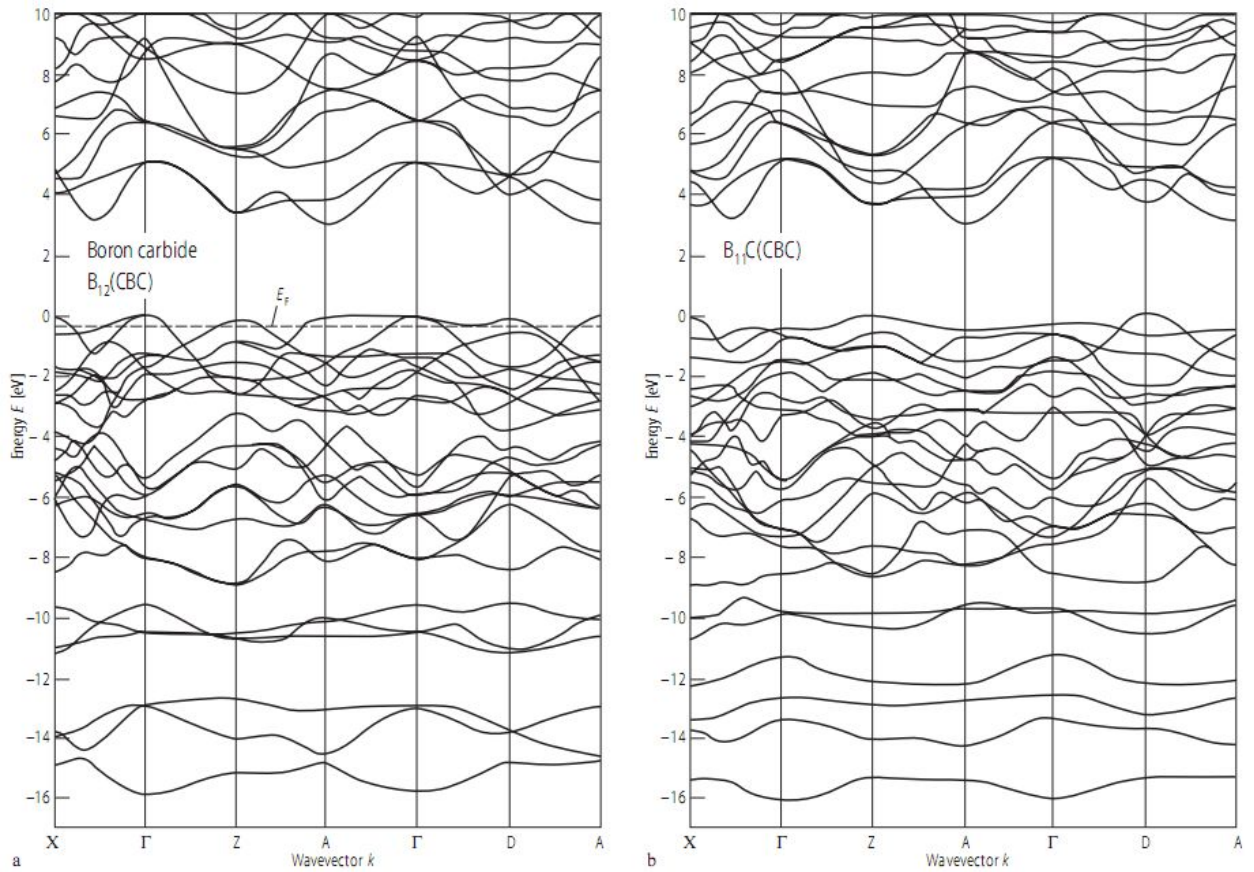


Fig. 5.2 Electron structure of boron carbide. Calculated energy bands of (a) hypothetical $B_{12}(CBC)$ and (b) hypothetical $B_{11}C(CBC)$ [81]. The zero of energy is at the top of the VB, and the dotted line shows the Fermi level.

The band structure calculations on boron carbide are based on the assumption of idealized structures for well-defined chemical compositions. That means that the specific hypothetical arrangement of atoms in a well-defined unit cell is occasionally assumed. However, the real structure consists of a statistical arrangement of differently structured elementary cells. In any case, their individual concentration is too high to allow the assumption of a small perturbation of one of them. For example, in the least-disturbed structure at the carbon-rich limit of the homogeneity range there are 100 % $B_{11}C$ icosahedra and 82% C-B-C and 18% C-B-B chains. The composition $B_{13}C_2$, which has often been assumed to be an ideal boron carbide, is in reality the mostly distorted structure in the whole homogeneity range and contains about 60% $B_{11}C$ icosahedra, 40% B_{12} icosahedra, 64% C-B-C chains, 18% C-B-B chains and 18% chain-less cells [83].

5.1.1. Structural properties

It is commonly accepted [80-85], that its structure consists of 12-atom icosahedral units placed at the vertices of a rhombohedral unit cell and a linear chain of three atoms along the crystallographic c axis. Boron carbide crystals are covalent bounded like diamond, graphite, and boron simple crystals. The structure of hexagonal boron carbide most closely resembles that of α -boron (hexagonal modification) [86, 87]. The α -boron structure is described as a somewhat

distorted cubic close packing of B_{12} icosahedra linked by six covalent B–B bonds (1.71Å) and six electron-deficient three-center B–B bonds (2.03Å) [86, 88, 89] (Fig. 5.1).

If the B–B bonds in the icosahedra are longer (1.72–1.84Å), the B_{12} icosahedron is a conventional structural unit of boron crystals. Upon the formation of boron carbide, the close packing of B_{12} icosahedra persists. An additional C-B-C group occupies octahedral cavities between the icosahedra, forming new covalent bonds between the carbon atoms of the C-B-C group and the boron atoms of the icosahedra. The introduction of the C-B-C group into the α -boron structure induces substantial deformation of the icosahedron, the a -axis of the unit cell increases from 4.91 to 5.60Å and the c -axis decreases from 12.57 to 12.10Å [79, 81]. Due to internal bonding constraints, no more than two carbon atoms present in any icosahedron. In the $B_{11}C(CBC)$, one C atom occupies the vertex position of the icosahedron and externally bonds to the B atom from another icosahedron. The unit cell volume increases from 262 to 330Å³ [90], and the density increases from 2.47 to 2.57 g/cm³. Boron carbide can be described as a layered structure: the distance between the layers of icosahedra in $B_{13}C_2$ is 4.03Å. The centres of icosahedra in the layer are at a distance of 5.58Å, and the centres of the polyhedra from the neighboring layers are 5.16Å apart. The energy of the three centre B–B bonds is lower than the energies of B–B and B–C bonds, which are substituted in the process of formation of boron carbide crystal [83, 91]. This fact is responsible for the higher stability of boron carbide crystals as compared with α -boron crystals.

In general, the most stoichiometric structure of boron carbide is supposed to be $B_{11}C(CBC)$. This means, that there is a carbon atom forming a $B_{11}C$ cluster with an unknown hybridization and two carbon atoms with a sp^3 -like hybridization at the extreme of a linear chain. There are 11 boron atoms forming an icosahedron and one boron atom in the centre of the linear chain, presumably with an sp^2 -like hybridization.

5.1.2. Energy-level diagrams for establishing the K-shell binding energy

Atomic and ionic boron have the valence electronic configuration $2s^2p^1$ and $1s^22s^22p^2$, respectively. The energy levels of the ground states for neutral atoms BI (2P_0) and ions BII ($^1S_{1/2}$) and BIII ($^2S_{1/2}$) and excited state of ion BII (3P_0) are shown on Fig 5.3. Also the energy levels of the ground states for neutral atoms CI (3P_0) and ions CII (2P_0) and CIII ($^1S_{1/2}$) and excited state of ion CII (4P_0) and CIII (3P_0).

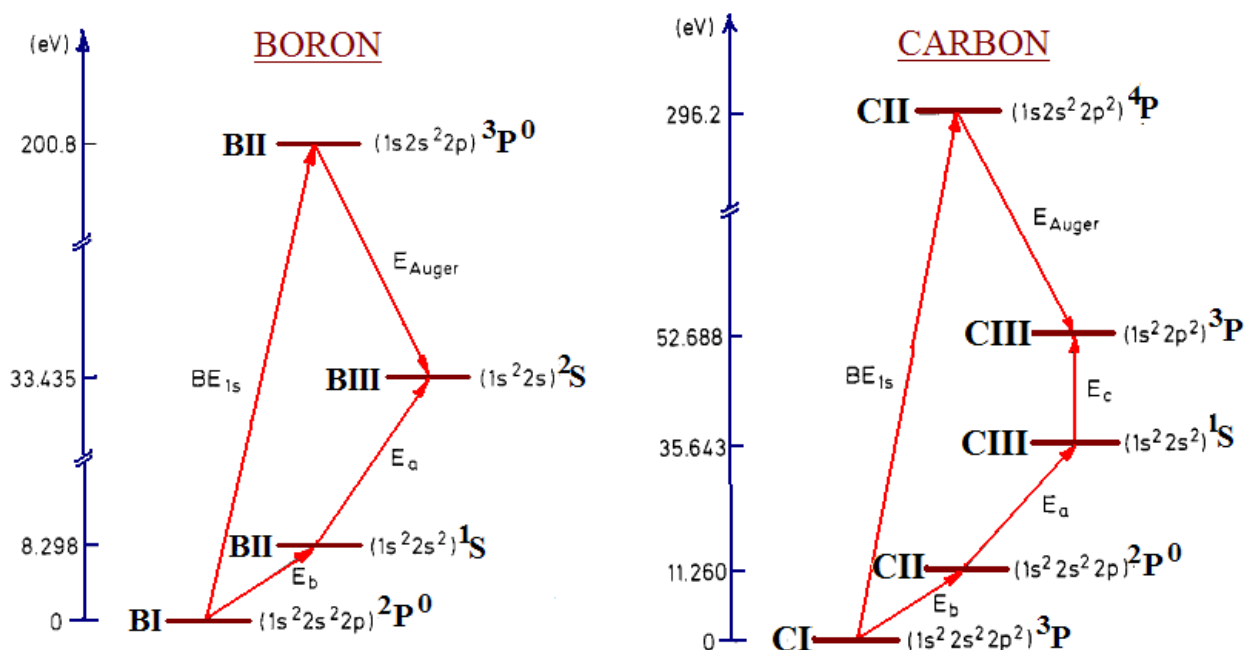


Fig. 5.3 Energy-level diagrams for atomic boron (left) and carbon (right) [92]

The electrons occupy atomic orbitals of different energy levels, such as $1s$, $2s$, $2p$, etc. These orbitals represent the probability distribution for finding an electron anywhere around the atom. But in our investigation, we deal with the molecular structure of boron carbide. Molecular orbital theory posits the notion that the electrons in the molecules likewise exist in different orbitals that give the probability of finding the electron at particular points around the molecule. Let's consider the bonding in homonuclear diatomic molecule of boron - molecule of the formula B_2 .

Before the diagram for B_2 will be drawn, we must first find the in-phase and out-of-phase overlap combinations for boron's atomic orbitals. Then, we rank them in order of increasing energy. Each boron atom has one $2s$ and three $2p$ valence orbitals. Due to the great difference in energy between the $2s$ and $2p$ orbitals, we can ignore the overlap of these orbitals with each other. All orbitals composed primarily of the $2s$ orbitals will be lower in energy than those comprised of the $2p$ orbitals. Fig 5.4 shows the process of creating molecular orbitals for diboron by combining the orbitals of atomic boron. For any atom with an atomic number greater than seven, the p bond is less stable and higher in energy than the s bond formed by the two end-on overlapping p orbitals.

The three dumbbell-shaped p -orbitals have equal energy and are oriented mutually perpendicular (or orthogonal). The p -orbitals oriented in the x -direction (p_x) can overlap end-on forming a molecular bonding (symmetrical) σ -orbital and an antibonding σ^* -orbital. In contrast to the σ $1s$ MO's, the σ $2p$ has some non-bonding electron density at either side of the nuclei and the σ^* $2p$ has some electron density between the nuclei.

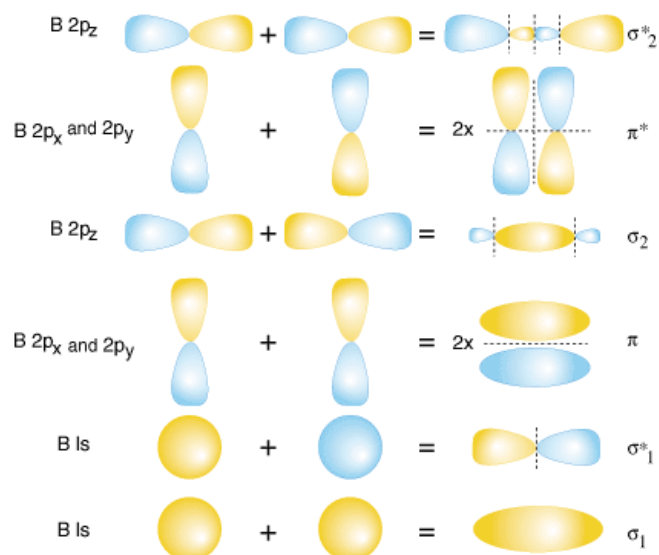


Fig. 5.4 The molecular orbitals of diboron (from web-site <http://www.sparknotes.com>)

The other two p -orbitals p_y and p_z can overlap side-on. The resulting bonding orbital has its electron density in the shape of two sausages above and below the plane of the molecule. The orbital is not symmetrical around the molecular axis and is therefore a π -orbital. The antibonding π^* orbital (also asymmetrical) has four lobes pointing away from the nuclei. Both p_y and p_z orbitals form a pair of π -orbitals equal in energy (degenerate) and can be higher or lower than that of the σ -orbital (Fig. 5.5.)

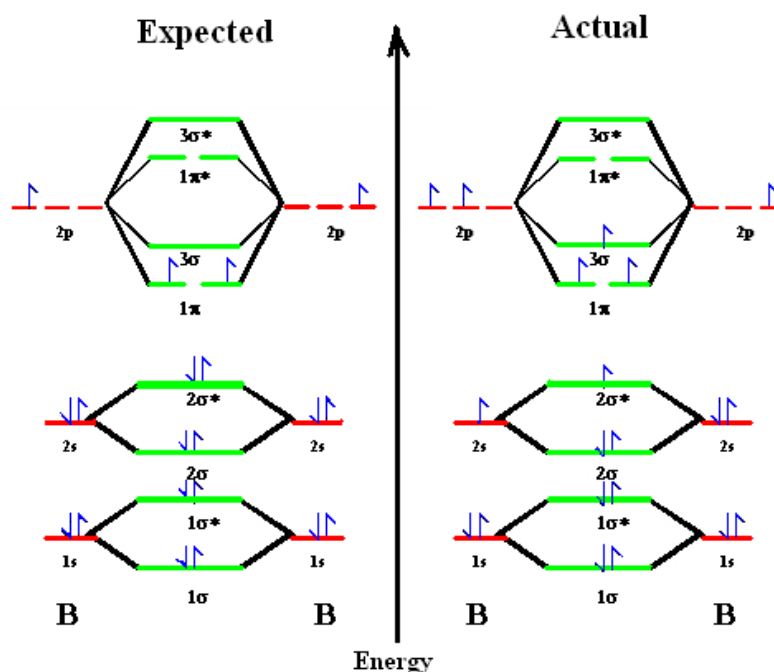


Fig. 5.5 Orbital expected (*left*) and actual (*right*) diagrams for diboron

In B₂ the 1s and 2s electrons do not participate in bonding but the single electrons in the 2p orbitals occupy the 2π_y and the 2π_x MO's resulting in bond order 1. Because the electrons have equal energy (they are degenerate) B₂ is a diradical and since the spins are parallel the compound is paramagnetic. The bonding orbitals of B₂ molecule are lower in energy than the atomic orbitals from which it is composed. On the other side, the antibonding orbitals are higher in energy (unstable) than the atomic orbitals from which it is composed.

5.2 Near edge X-ray absorption

When the X-rays hit a sample, the oscillating electric field of the electromagnetic radiation interacts with the electrons bound in an atom. Either the radiation will be scattered by these electrons or absorbed and excite the electrons.

A narrow parallel monochromatic x-ray beam of intensity I_0 passing through a sample of thickness x (Fig. 5.6) will get a reduced intensity I according to the expression:

$$\ln(I/I_0) = \mu x \quad (5.1)$$

where μ is the linear absorption coefficient, which depends on the types of atoms and the density ρ of the material.

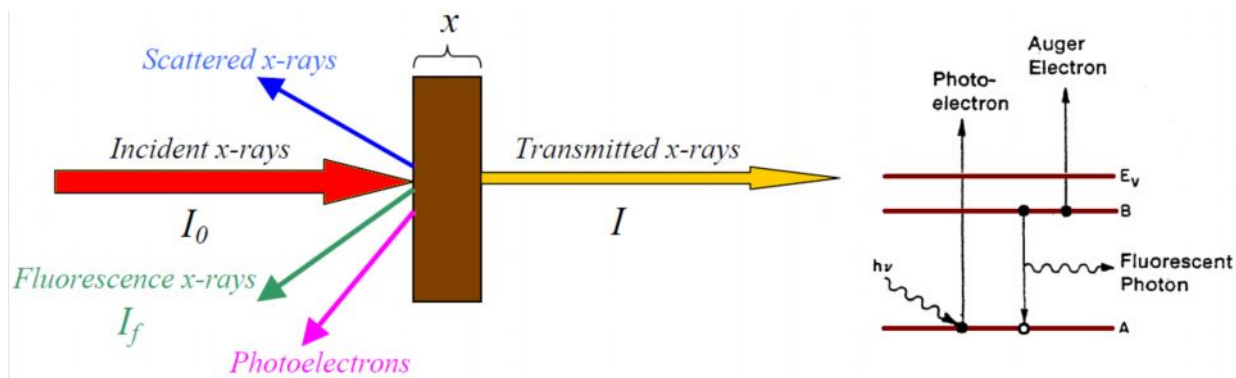


Fig. 5.6 Diagram of Beer–Lambert absorption of a beam of light as it travels through a sample of thickness x

At certain energies, where the absorption increases drastically and gives rise to an absorption edge. Each of such edges occur when the energy of the incident photons is just sufficient to cause excitation of a core electron of the absorbing atom into a continuum state, i.e. to produce a photoelectron. Thus, the energies of the absorbed radiation at these edges correspond to the binding energies of the electrons in the K, L, M, etc, shells of the absorbing elements. The absorption edges are labelled in the order of increasing energy, K, L_I, L_{II}, L_{III}, M_I, ..., corresponding to the excitation of an electron from the 1s (S^2), 2s (S^2), 2p (P^2), 2p ($P_{3/2}^2$), 3s (S^2), ... orbitals (states), respectively.

An X-ray absorption spectrum is generally divided into 4 sections: 1) *pre-edge* ($E < E_0$); 2) *X-ray absorption near edge structure* (XANES), where the energy of the incident x-ray beam is $E = E_0 \pm 10$ eV; 3) *near edge X-ray absorption fine structure* (NEXAFS), in the region between 10 eV up to 50 eV above the edge; and 4) *extended x-ray absorption fine structure* (EXAFS), which starts approximately from 50 eV and continues up to 1000 eV above the edge.

The minor features in the pre-edge region are usually due to the electron transitions from the core level to the higher unfilled or half-filled orbitals (e.g, $s \rightarrow p$, or $p \rightarrow d$). In the XANES region, transitions of core electrons to non-bound levels with close energy occur. Because of the high probability of such transition, a sudden raise of absorption is observed. In NEXAFS, the ejected photoelectrons have low kinetic energy ($E-E_0$ is small) and experience strong multiple scattering by the first and even higher coordinating shells. In the EXAFS region, the photoelectrons have high kinetic energy ($E-E_0$ is large), and single scattering by the nearest neighbouring atoms normally dominates.

Due to the fact that the concentration of boron in boron carbide exceeds 80 percent, we should pay attention to the experimental data of B_4C near B K-edge (~ 189 eV). The XANES spectra of six different B_xC_{1-x} compounds are depicted in Fig. 5.7. The B(1s) core level absorption edges are indicated together with the reference spectra of atomic boron, boron carbide B_4C and oxide boron B_2O_3 . The carbon content in atomic percentage of each sample is shown on the top of the spectrum. The B_4C reference spectra (*red line* in Fig. 5.7) show no clear separation between the π^* and σ^* regions, either in the B(1s) absorption edge. This feature reflects a complex state of hybridization. The Boron K-edge starts at 189.0 eV and presents a narrow fingerprint peak at 190.9 eV on top of a background assigned to π^* states. The origin of this transition is still unclear. Jimenez *et al.* [84, 94] suggested that this peak arises from the boron in the icosahedra bonded to a C-B-C carbon atom or from boron in the chain itself.

Furthermore, three additional peaks were reported in that work at 191.7 eV assigned to B-rich carbide, at 192.3 eV assigned to boron sub-oxide, and at 193.7 eV assigned to boron oxide. If we focus now on the co-evaporated boron carbide compounds, up to five different peaks can be distinguished in the B ($1s$ - π^*) region of the XANES spectra linked to resonant excitonic states. These peaks have been labeled as B_0 - B_4 and appear at photon energies of 189.7, 191.0, 191.8, 192.4, and 194.0 eV, respectively. By direct comparison with the spectra measured by Jimenez *et al.*[84], it was observed that B_1 and B_4 coincide in energy with the B_4C and B_2O_3 π^* states. While peaks B_1 , B_3 , and B_4 appear in all the samples with different relative intensities, B_2 is only detected for the sample with a 5 at. % of C, supporting the assignment done in for boron-

rich boron carbides [93]. Only peak B_0 does not correspond to any known BC-based reference material.

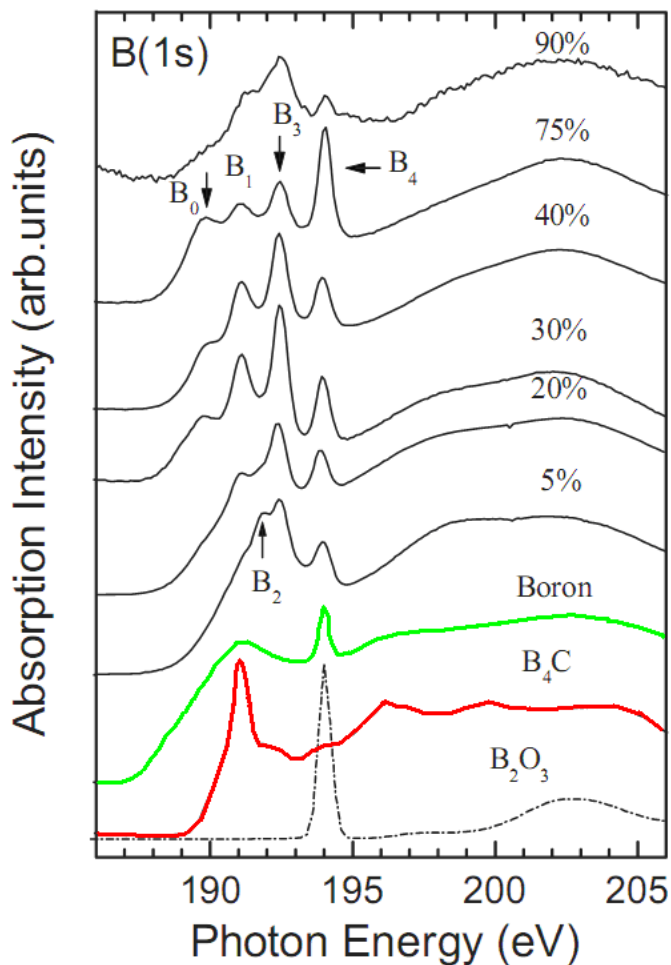


Fig.5.7 B(1s) core level photoabsorption spectra of B_xC_{1-x} compounds. The curves are labeled with the names of the reference compounds and the carbon at. % in each B_xC_{1-x} sample. Up to five different bonding environments are distinguished in the B(1s) edge [93].

Therefore, peaks B_0 , B_1 , B_3 , and B_4 have been attributed to B-C₃, B-C₂□, B-C□₂, and B-□₃ bonding environments in an sp^2 boron carbide structure, respectively. The symbol “□” is used to denote the C vacancy around the tricoordinated boron atom and a vacancy is decorated with superficial oxygen contamination. Besides, the reported electron energy-loss spectrum of a BC₃ film shows a very intense peak at 190.1 eV in the boron K edge, which is in agreement with the assignment of peak B_0 . Additionally, the relative intensity of B_0 is exactly maximum for the sample with a BC₃ composition.

The XANES results show that the icosahedral B₄C-like structure remains as long as C represents less than ~50% of the total atomic composition. For stoichiometries richer in C than B, the structure tends to *graphitize*. These results are in agreement with the explanation given for the resistivity experiments reported in [95]. Moreover, the B(1s) XANES spectra clearly prove

that C is incorporated in the B_xC_{1-x} structure and not merely forming isolated graphite-like domains. In fact, no elemental phase segregation has been detected for any of the samples studied.

In the works of Jimenez *et al* [84, 94], the X-ray absorption spectra at the B K-edge (Fig. 5.8) from: (a) a polycrystalline B_4C -bulk sample, (b) a B_4C powder, (c) a non-stoichiometric B_xC ($x>4$) thin film grown by sputtering, (d) a B_xC film grown by pulsed laser deposition, (e) an amorphous boron powder and (f) a crystalline boron powder were obtained. Curve Fig 5.8a was used as a reference for comparison purposes. The position of the absorption edge for stoichiometric B_4C is at 189eV and at 187 eV for boron and non-stoichiometric boron carbide. Also, there are additional peaks in the non-stoichiometric and boron samples compared to the B_4C sample, which cannot be assigned to B_2O_3 contamination.

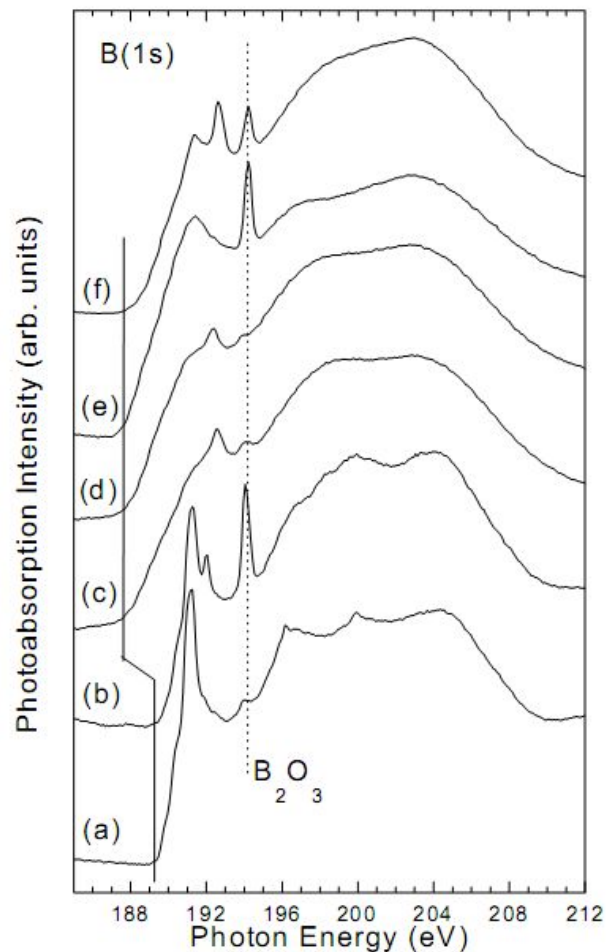


Fig.5.8 X-ray absorption spectra at the boron edge [84, 94] from: (a) B_4C -bulk sample, (b) B_4C -powder, (c) B_xC film grown by sputtering, (d) B_xC film grown by pulsed laser deposition, (e) amorphous B, and (f) crystalline B

The narrow edge peak (~ 192 eV) is assigned to the transition of B(1s) electrons to the unoccupied B(2p) states (π^*), and a wide peak (195...208eV) to the transition of B 1s electrons to the unoccupied B σ^* states for all cases. On the other side, the absorption spectrum of B_4C

sample prepared by magnetron sputtering (Fig. 5.8c) is very different from that of commercially obtained powder sample (Fig. 5.8b), which indicates a possible stoichiometric change during the sputtering process. In general, the spectral features in the gas phase are much sharper than in the solid state due to the influence of intericosahedral bonds in the solid. Also, the additional peak can be obtained corresponding to bonding between the boron icosahedra and the extreme carbon atom in the C-B-C chain or to bonding within the C-B-C chain. The onset of absorption from the B(*1s*) level shifts 2 eV depending on the icosahedra containing or not a carbon atom.

5.3. Refractive index of boron carbide

One of the main works of the determination of the experimental refractive index of boron carbide inside thin films is work of Soufli R. *et. al.* [96]. In this work the experimental determination of the optical constants (refractive index) of DC-magnetron-sputtered boron carbide films in the 30–770 eV photon energy range is presented using the transmittance measurements (Fig 5.9).

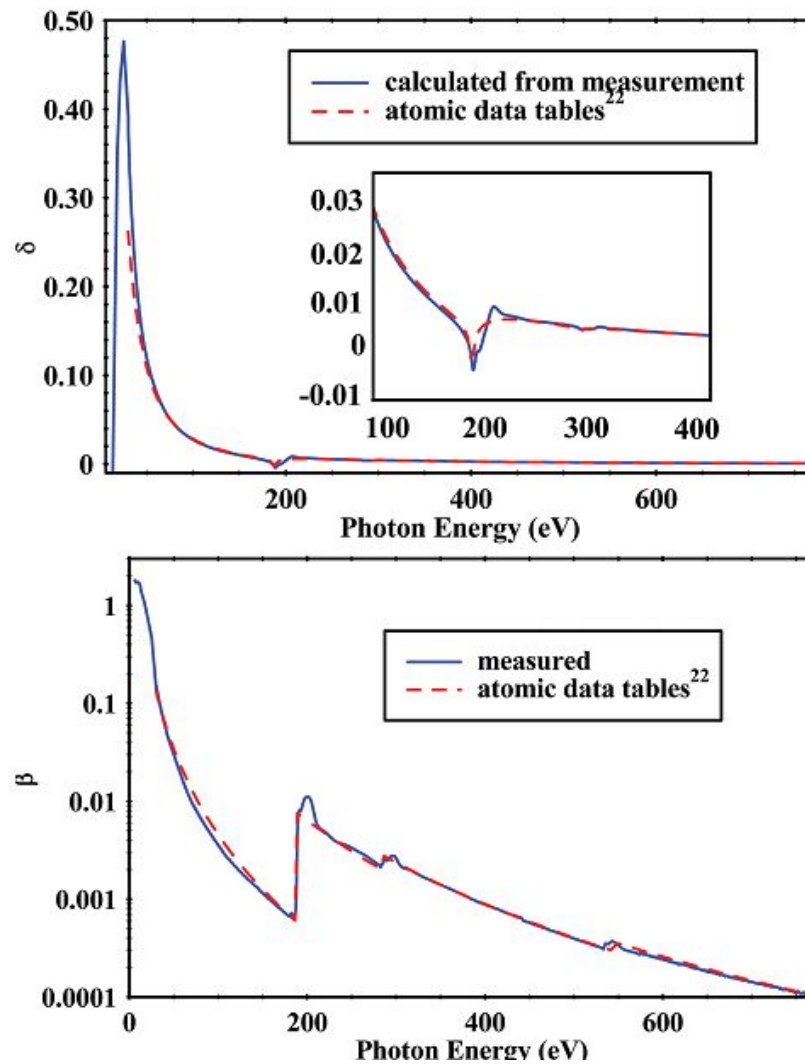


Fig. 5.9 Experimental (*blue*) and Henke’s tabulated (*red*) optical constants δ (*top*) and β (*bottom, log scale*) for sputtered boron carbide [96]. δ was calculated through the Kramers–Krönig relation, using a composite data set of β values. The inset (*top*) shows an expanded plot of δ in the energy region around the boron K edge.

Additionally, in this work, the density, composition, surface chemistry, and morphology of the films were also investigated using Rutherford backscattering (RBS), X-ray photoelectron spectroscopy (XPS), atomic force microscopy (AFM), scanning electron microscopy (SEM), and EUV reflectance measurements.

Figure 5.9 reveals significant differences between the experimental data and the tabulated values, especially and predictably in energy regions around the boron, carbon, and oxygen K absorption edges. The experimental absorption coefficient of the B₄C films in the region of the boron K edge displays a prominent NEXAFS feature centered near 200 eV that is a factor of 2 higher than the values derived from the atomic data tables. The feature around 200 eV is in qualitative agreement with the X-ray absorption spectra on the boron carbide films reported in [84, 85, 94, 97] and could be assigned to the σ^* -like states.

With the experimental data for optical constants of B₄C films in the photon energy range 30-770eV, including NEXAFS structures in the energy regions around the boron, carbon and oxygen K absorption edges [96], we have open questions concerning the behaviour of these constants for the B₄C material within the periodical multilayers.

Chapter 6

Resonant soft X-ray reflectivity of multilayers based on B₄C material

Multilayers composed by a metal and a low *Z* element like boron are used as optical elements in both the soft X-ray spectral range [98, 99] as well as at the higher photon energies on the 3rd generation synchrotron beamlines [100]. These also hold for application at Free-Electron lasers like FLASH [39]. The shape and total scattering power of a fundamental Bragg reflection of a ML are determined by the numbers of periods and the differences in the optical refraction indexes of the composed layer materials. Various techniques are reported to measure the optical properties of the material in the hard X-ray range, for instance, measurement of the integrated intensities of diffraction peaks [101, 102], interferometry [103] or measurements of the totally reflected intensities [104]. Although reflectometry measurements and also Faraday rotation experiments have been carried out in the soft X-ray range as well [105, 106], only a few measurements of the real part of the refractive index have been reported up to now because of the lack of single crystals with the lattice in 100 nm range. The imaginary part β of refraction index $n=1-\delta+i\beta$ is determined by X-ray absorption measurement over a wide range of energies [107-110]. Measurement of Total Electron Yield (TEY) suffers from the low penetration depth limiting the number of probed layers within a ML. Since, the top layers may be oxidized true “bulk” properties are not accessible. Another problem for the ML measurements is the strong re-absorption effects [111-113].

One can determine the degree of electronic excitations by scanning energy through the boron K-edge by energy-resolved reflectivity experiment at BESSY II. In this Chapter, the energy-resolved photon-in-photon-out method [114-116] is used to measure the dispersion and absorption of boron carbide separately by two independent methods in the soft X-ray range using Bragg reflection from the B₄C multilayer. This approach is an alternative to the commonly used soft X-ray absorption and transmission measurements, and provides complete information about the optical properties of the materials which compose the multilayer. Soft X-ray analysis of the energy-dependence of the optical properties near the boron K-edge and its deviation from the prediction made for free atoms [117, 118] provide information about the bonding state of the boron atoms inside ML.

6.1. Mirror fabrication

For our investigations, the three types of periodical multilayers have been selected: Ru/B₄C and Mo/B₄C, designed and fabricated at the ESRF Multilayer Laboratory and W/B₄C, designed and fabricated by the AXO Dresden GmbH by microwave assisted sputter deposition (for last

sample, in nitrogen gas). Two separate sputter targets one of the metal and one of boron carbide enable alternating film growth on up to 300 mm long on the super-polished Si substrates. The thickness uniformity is ensured by linear motion of the sputter sources in front of the substrate. The respective deposition rates were $R(\text{Me}) = 0.09\text{-}0.11$ nm/s and $R(\text{B}_4\text{C}) = 0.015\text{-}0.030$ nm/s. The thickness was controlled by numerical modeling combined with *ex situ* calibration coatings. We analyzed the next periodical MLs: Ru/ B_4C with 10, 17, 20, 60 and 63 periods, Mo/ B_4C with 20 period and W/ B_4C with 10 period; first two type of ML with a d-spacing of 5 nm and a thickness ratio, γ , of about 0.4, the sample from AXO Dresden GmbH with a d-spacing of 4.5 nm and a thickness ratio, γ , of about 0.47.

6.2. Theoretical background

The energy-resolved photon-in-photon-out method was used to measure the dispersion and the absorption coefficient of boron carbide separately by two independent methods in the soft X-ray range using Bragg reflection from periodical multilayers.

Peak positions. It is obvious that the effect of refraction and absorption of the incident X-ray beam is much stronger in the soft X-ray range compared to the hard X-rays. Now let's consider a periodical multilayer as a homogeneous material with an average refractive index $n_{\text{eff}} = 1 - \delta_{\text{eff}} + i\beta_{\text{eff}}$, where δ_{eff} is the dispersion, β_{eff} is the absorption coefficient of the materials assumed to be homogeneous over the whole sample volume. Due to refraction at the vacuum-sample interface the average dispersion parameter δ_{eff} of the ML can be obtained from the deviation of angular positions of the Bragg peak maximum compared to the prediction made for $n=1$. δ_{eff} can be decomposed into the contributions δ_{Me} and $\delta_{\text{B}_4\text{C}}$ of the individual layers both materials according to their relative contribution $\gamma = d_{\text{Me}} / (d_{\text{Me}} + d_{\text{B}_4\text{C}})$:

$$\delta_{\text{eff}} = \frac{d_{\text{Me}} \delta_{\text{Me}} + d_{\text{B}_4\text{C}} \delta_{\text{B}_4\text{C}}}{d_{\text{Me}} + d_{\text{B}_4\text{C}}}, \quad (6.1)$$

where d_{Me} and $d_{\text{B}_4\text{C}}$ are thicknesses of the Me and B_4C layers. Bragg reflection appears whenever the wavelength λ (or energy E) and the incidence angle θ_0 of the ML fulfils the Bragg equation

$$m\lambda = 2dn_{\text{eff}} \sin \theta_0, \quad (6.2)$$

where $d = d_{\text{Me}} + d_{\text{B}_4\text{C}}$ is the ML period. Using Snell's law, we obtain the first-order refractive corrected Bragg's law

$$\lambda = 2d \sin \theta_0 \left[1 - \left(2\delta_{\text{eff}} / \sin^2 \theta_0 \right) \right]^{1/2}. \quad (6.3)$$

Measuring the true angular position of the Bragg peak ($m=1$) for a given photon energy E at $\theta = \theta^{\text{Bragg}}$, δ_{eff} can be derived by:

$$\delta_{\text{eff}}(E) = \gamma\delta_{Me} + (1-\gamma)\delta_{B_4C} \cong \frac{1}{2} \left[\sin^2 \theta(E) - \left(\frac{\lambda}{2d} \right)^2 \right], \quad (6.4)$$

where $\theta(E)$ is the measured Bragg angle outside the ML. Equation (6.4) is the approximation, because terms proportional to δ^2 and β^2 are omitted. Using the measured values of q at given E the resonant contribution δ_{B_4C} can be determined by Eq. (6.4) using the structural parameters of the investigated multilayer and the non-resonant contribution δ_{Me} from Henke's table varying linear in the measured energy range [118].

On the other hand, the increasing absorption at the B K-edge shortens the penetration of the photons in the sample and reduces the number of planes capable of scattering in phase, resulting in broader and weaker peaks. A further correction term should be introduced to account for the effect of absorption on the Bragg peak position. Following the model of Rosenbluth and Lee [119] one has

$$\delta_{B_4C} = \frac{\left[\frac{1}{2} \left[\sin^2 \theta(E) - \left(\frac{\lambda}{2d} \right)^2 \right] - \delta_{Me} \right]}{D} + \delta_{Me}, \quad (6.5)$$

where

$$D = \gamma - \frac{(\beta_{B_4C} - \beta_{Me}) \sin^2(\pi\gamma)}{\pi^2 [\gamma\beta_{B_4C} + (1-\gamma)\beta_{Me}]} \quad (6.6)$$

To determine δ from Eqs (6.5) and (6.6) we have scaled the experimental absorption spectra to the calculated values below and above K edge. Absorption correction is found to have little, but not negligible, effect on δ for B_4C .

Peak widths. The fit reflects the weighted average for the position of the reflection, even if there are some slight deviations due to the peak shape. Note that a more precise fit can be obtained by simulating the reflectivity spectra in the small-angle approximation or soft X-ray diffraction, where absorption is severe. The reflectivity curves exhibit a significant broadening of the Bragg peaks when the photon energy is set at and beyond the K-edge, because the absorption is the function of energy. Since the refractive index n_{eff} is a complex quantity, $n_{\text{eff}} = 1 - \delta_{\text{eff}} + i\beta_{\text{eff}}$, the electric field amplitude of wave propagating in the medium is proportional to $\exp(in_{\text{eff}}\mathbf{k}\mathbf{r}) = \exp(i(1-\delta_{\text{eff}})\mathbf{k}\mathbf{r})\exp(-\beta_{\text{eff}}\mathbf{k}\mathbf{r})$ with $|\mathbf{k}| = 2\pi/\lambda$. Therefore the reflected intensity is proportional to

$$I_{sc} \cong I_{inc} R \exp(-2\beta_{\text{eff}}kD_{\text{eff}}) \exp(-\sigma^2 q^2), \quad (6.7)$$

where R is the Fresnel reflectivity and $D_{\text{eff}} = N_{\text{eff}} d / \sin\theta$ is the effective absorption length scaled with N_{eff} as the effective number of absorbing ML periods. The second exponential considers the fact that the reflectivity is reduced also by the interface roughness, σ , within the ML. By

definition D_{eff} is the thickness where the ratio $I_{sc}/I_{inc}R$ is decreased to $1/e$. Subsequently D_{eff} and the absorption coefficient β_{eff} are related by

$$D_{eff} = \frac{1 + \sigma^2 q^2}{2\beta_{eff}k} \quad (6.8)$$

In the kinematical approximation, the peak shape of a ML reflection peak is described by the Laue function with peak width $\Delta q = 2\pi/D_{eff}$. Subsequently, the full width at half maximum (FWHM) Δq of the Bragg peak is

$$\Delta q = \frac{2\pi}{D_{eff}} = \frac{4\pi k}{1 + \sigma^2 q^2} \beta_{eff} \quad (6.9)$$

providing a linear relation to the effective absorption coefficient β_{eff} . β_{B4C} is derived via $\beta_{eff} = \gamma\beta_{Me} + (1 - \gamma)\beta_{B4C}$ taking into account the contribution of β_{Me} [120].

Peak intensities. The structure factor for a periodical multilayer with a compositional modulation profile $c(x)$ (one-dimensional projection of the concentration along the growth direction) is given by

$$F(Q) = (f_1 n_1 - f_2 n_2) \int_0^d c(x) \exp(iQx) dx \quad (6.10)$$

where d , F , n and Q are the period of multilayer, the complex X-ray atomic scattering factor, atom number density and the scattering vector, respectively. When the modulation profile is ideally stepwise at interfaces (*step model*)

$$c(x) = \begin{cases} 1 & 0 \leq x \leq d_1 \\ 0 & d_1 \leq x \leq d_1 + d_2 = d \end{cases} \quad (6.11)$$

where d_1 and d_2 are the individual layer thicknesses of 1 and 2 components, respectively. The structure factor can be written as

$$|F(m)|^2 = |f_1 n_1 - f_2 n_2|^2 \frac{\sin^2(\pi m d_1 / d)}{(\pi m / d)^2} \quad (6.12)$$

Thus, the Bragg peak of m th order intensity is proportional to $|f_1 n_1 - f_2 n_2|^2$.

From the works of Vinogradov & Zeldovich [120, 121], and Rosenbluth & Lee [119] the ratio of intensity of the reflected beam to the intensity of the incident beam can be written as

$$I(\theta)/I_0 = \left| \begin{array}{l} -2ir \exp(i\psi_2) \sin \psi_1 \sin(N \cos^{-1} x) \times \\ \left\{ \begin{array}{l} \exp(i\psi)(1-r^2 \exp(-2i\psi_1)) \sin(N \cos^{-1} x) - \\ -\sqrt{\Delta} \sin[(N-1) \cos^{-1} x] \end{array} \right\} \end{array} \right|^2, \quad (6.13)$$

where, ψ_k is the phase shift of the wave through the k th layer, r is Fresnel reflection coefficient, to first order in the unit decrement difference is

$$r = \frac{(\Delta\delta + i\Delta\beta)}{2 \sin^2 \theta} P(\theta), \quad (6.14)$$

Here $P(\theta)$ is a polarization factor equal to unity or $\cos 2\theta$ depending upon whether the incident beam is s -polarized or p -polarized. The optical phase thickness ψ of the ML period is

$$\psi \equiv \frac{2\pi}{\lambda} \int_{\text{period}} dz n(z) \left[\sqrt{1 - \cos^2 \theta / n^2(z)} \right] \cong \frac{2\pi d \sin \theta}{\lambda} \left(1 - \frac{\delta_{\text{eff}} + i\beta_{\text{eff}}}{\sin^2 \theta} \right), \quad (6.15)$$

and

$$\begin{aligned} \Delta &= 1 - 2r^2 + r^4 \\ x &= \left[\cos \psi - r^2 \cos(\psi_1 - \psi_2) \right] / \sqrt{\Delta}, \end{aligned} \quad (6.16)$$

Eqs. 6.13-6.16 are the exact dynamical formula valid to all orders of r . However, for most cases of interest, accuracy to first order in r is sufficient. Note, that for $N=1$, Eq 6.13 reduces to the exact reflection formula for two interference films [121].

For extremely weak reflection, or, as it is more often in the case in the soft X-ray region, when absorption loss in a substrate is much greater than reflection loss at interface, then $\cos^{-1} x \approx \psi$ in Eq. 6.16. The intensity ration for an polarized beam become

$$\begin{aligned} I(\theta)/I_0 &= (\Delta\delta^2 + \Delta\beta^2) \frac{|\sin \psi_1|^2}{4 \sin^4 \theta} \cdot \frac{1 + \cos^2(2\theta)}{2} \times \\ &\times \frac{(1 - \exp(-2N\psi_I))^2 + 4 \exp(-2N\psi_I) \sin^2(N\psi_R)}{\sinh^2 \psi_I + \sin^2 \psi_R}, \end{aligned} \quad (6.17)$$

with ψ_R is ψ_I the real and imaginary part of ψ (Eq. 5.16), respectively.

For extremely weak absorption, i.e., $2N \psi_I \ll 1$, the behaviour of Eq. 6.17 is essentially $(\sin N \psi_R / \sin \psi_R)^2 \approx N^2$, the result easily can be obtained from the kinematical theory (see, Eq. 6.12). On the opposite extreme, $2N \psi_I \gg 1$, Eq. 6.17 become Lorentzian and this result can be derived from the Darwin-Prins equation.

In order to obtain similar equations for real crystal, Eq. 6.16 can be re-written as

$$\Delta = (D + iB)^2$$

$$x = \cos \psi / \sqrt{\Delta} \quad , \quad (6.16')$$

In this case, the ratio of intensity of the reflected beam to the intensity of the incident beam for N periods is given by

$$I(\theta) / I_0 = \left| \frac{(D + iB) \sin(N \cos^{-1} x)}{\sin(N \cos^{-1} x) - \sqrt{\Delta} \exp(-i\psi) \sin[(N-1) \cos^{-1} x]} \right|^2 \quad , \quad (6.18)$$

The amplitude reflectivity of a single period $D+iB$ equals

$$D + iB = -(-1)^m 2r \sin(m\pi d_1 / d) \quad , \quad (6.19)$$

In order to show that Eq. 6.18 approaches the kinematical and dynamical theory for extreme values of N , first considers the case of weak reflecting power per plane, i.e., $x \approx \cos \psi$. Eq. 6.18 under this approximation can be simplified to

$$I(\theta) / I_0 = \left| (D + iB) \exp(-iN\psi) \frac{\sin(N\psi)}{\sin \psi} \right|^2 \quad , \quad (6.20)$$

For case of negligible absorption, Eq. 6.20 is exactly the kinematical equation with usual the $(\sin N \psi / \sin \psi)^2$ behaviour. When absorption cannot be ignored, the result can be rewritten in a form to Eq. 6.17. In the limit as N approaches infinity, the intensity profile is Lorentzian in nature.

Near the Bragg condition, $2d \sin \theta_0 = m\lambda$, the phase can be written as $\psi = m\pi + \xi$ with

$$\xi = \frac{kd}{\sin \theta} \left[(\sin \theta - \sin \theta_0) \sin \theta - (\delta_{\text{eff}} + i\beta_{\text{eff}}) \right] \quad , \quad (6.21)$$

Alternatively, Eq. 6.18 can be expressed, through simple algebraic manipulation, in the following form that is more convenient for comparison with the Darwin-Prins equation:

$$I(\theta) / I_0 = \left| \frac{(D + iB)}{\xi \pm \left(\xi^2 - (D + iB)^2 \right)^{1/2} i \cot(N \cos^{-1} x)} \right|^2 \quad , \quad (6.22)$$

In the limit of large N , the term $i \cot(N \cos^{-1} x)$ approaches unity, hence Eq. 6.22 reduces to the Darwin-Prins formula

$$I(\theta) / I_0 = \left| \frac{-(D + iB)}{\xi - \left(\xi^2 - (D + iB)^2 \right)^{1/2}} \right|^2 \quad , \quad (6.23)$$

6.3 Experimental results

Reflectivity measurements near the boron and carbon K-edge have been performed at the UHV triple axis soft X-ray reflectometer at BESSY II (Fig. 6.1). For the energy selection, the grating monochromator with 1228 lines/mm was used. The absolute energies were calibrated by measuring the binding energies of the Au $4f_{7/2}$ and $4f_{5/2}$ levels every 16 hours at the spectroscopy station located straight behind the reflectometer at the same monochromator. The accuracy of energy setting at the reflectometers was as good as 0.1 eV.

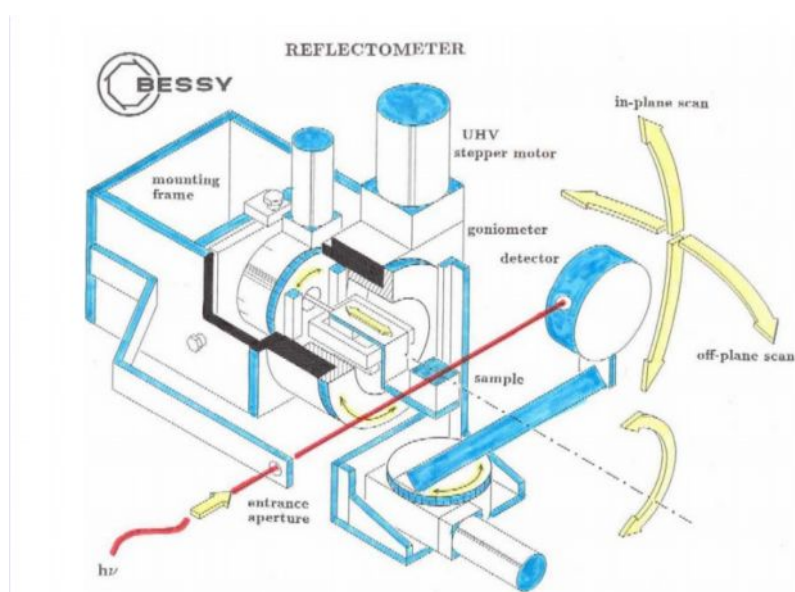


Fig. 6.1 Technical sketch of the UHV-triple axes configuration (from bessy.de)

6.3.1 Structural properties of multilayers

The multilayers were characterized at room temperature by X-ray reflectivity on a laboratory reflectometer operating at the Cu K_{α} (1.54\AA) line with subsequent modeling of X-ray reflectivity using the packages *Parratt32* [122] and *IMD* [123]. For simplicity, it is possible to demonstrate the Ru/B₄C ML reflectivity curves only with 10 periods at a wavelength $\lambda=1.54\text{\AA}$ (Fig. 6.2).

In the XRR simulation, it was assumed that the ML period is composed of two individual layers with sharp interfaces, and therefore the thickness ratio, Γ is defined as $\Gamma=d_1/(d_1+d_2)$, where d_1 and d_2 are the thicknesses of the first and second layer, respectively. In reality, the reflectivity is more sensitive to the imperfection of the interface between the two materials, such as roughness and intermixed area.

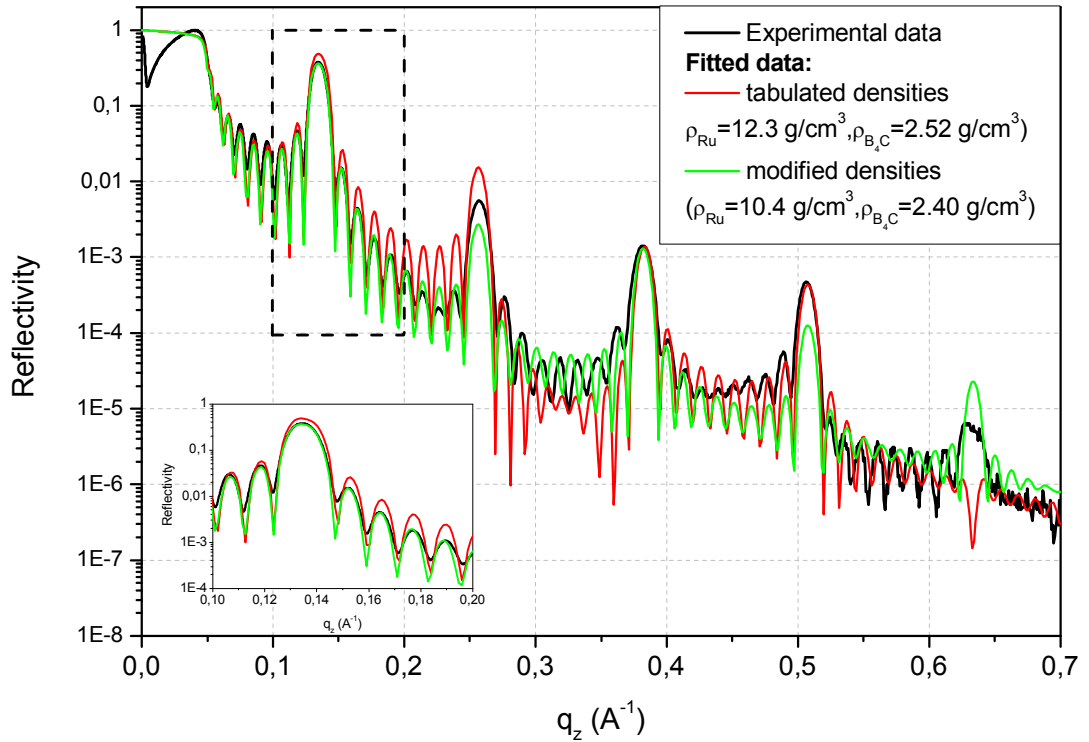


Fig.6.2 Experimental (*black line*) and fitted (*red and green lines*) reflectivity curves for Ru/B₄C multilayers with 10 periods at wavelengths $\lambda=1.54\text{\AA}$, using tabulated and modified densities of materials.

The major deviations weren't observed from the perfect periodicity or the appearance of an oxide surface layer for all samples. However, for the short period MLs, the interlayer-roughness (or *the interdiffusion layer*) has a strong influence on the reflection properties. In present case, the RMS roughness at the interfaces inside our MLs reaches from 10 to 18% of a single layer thickness. In addition, the densities of the composed materials depend on the deposition parameters and can vary in a wide range. Generally, the density can be determined from the angular position of the edge of total external reflection. As the critical angle for hard X-rays is very small, the sensitivity to small changes in the electron density is small as well. For example, the typical densities are taken from bulk material to be 12.3 g/cm^3 for Ru and 2.52 g/cm^3 for B₄C materials [124], corresponding to $\gamma=0.4$ were sufficient to verify the experimental data in the small angle range (respective fitting curves in Fig.6.2). However, the fit with reduced densities as suggested by the soft X-ray measurements and previous measurements at similar samples [125, 126] gave a tiny better agreement with experiment (see the respective curve and insets in Fig.6.2), although the respective changes in critical angle are within the experimental uncertainty. Calculated structural properties Ru/B₄C multilayers are demonstrated at Table 6.1.

Table 6.1. Calculated structural parameters of MLs deduced from GIXR measurements at 1.54Å (Cu K α), Ia and IIa consider the bulk densities of Ru and B4C, Ib and IIb refer to Ru and B4C densities reduced to 80% of bulk values.

Number of periods	d, Å	d _{Ru} , Å	d _{B4C} , Å	$\gamma=d_{Ru}/d$	σ_{Ru} , Å	σ_{B4C} , Å	$\rho(Ru)$, g/cm ³	$\rho(B_4C)$, g/cm ³
10	49,7	20,0	29,7	0,40	3,0	3,1	12,3	2,52
10	49,7	23,7	26,0	0,48	1,7	5,3	10,4	2,40
17	49,8	21,4	25,8	0,43	3,5	3,0	12,3	2,52
20	47,0	22,0	25,0	0,47	2	2	12,3	2,52
60	46,3	22,3	24,0	0,48	5,6	6,7	12,3	2,52
63	48,5	19,4	29,1	0,40	1,8	5,7	12,3	2,52
63	48,4	21,7	26,7	0,45	0,1	0,4	10,4	2,40

Fig 6.3 shows the measured and fitted W/B₄C ML reflectivity curves with 10 periods. This sample has the roughnesses between the various layers about 0.3nm, and a d-spacing of 4.5 nm and a thickness ratio, γ , of 0.47.

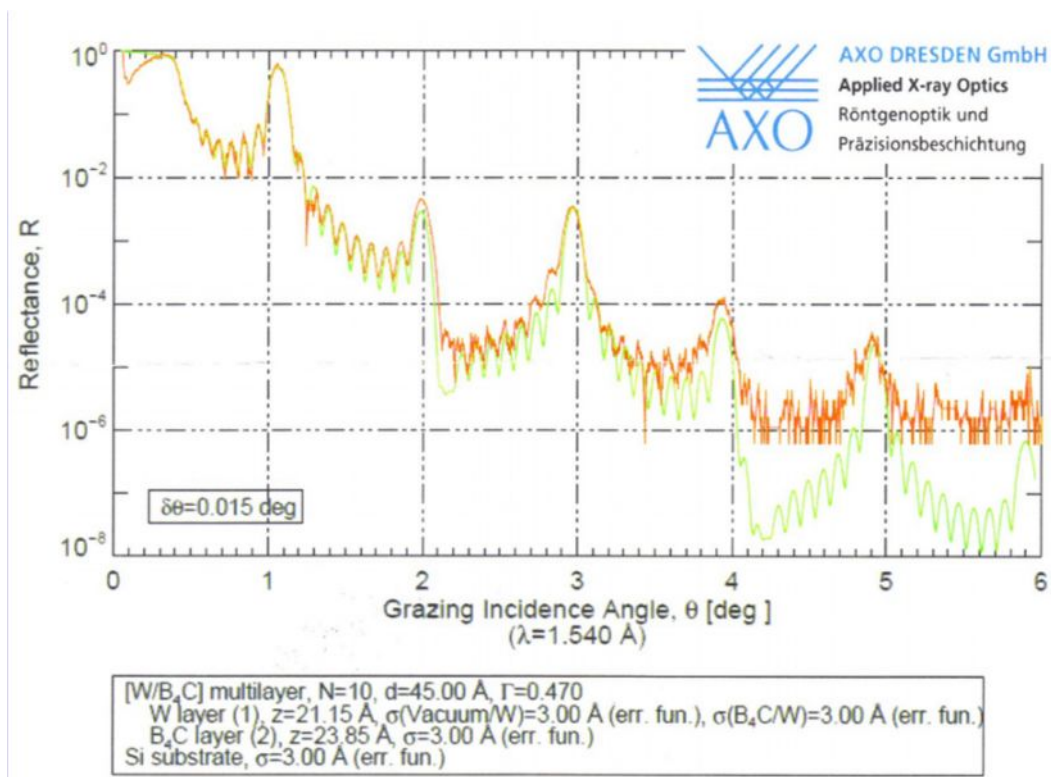


Fig.6.3 Experimental (red line) and fitted (green line) reflectivity curves for W/B₄C multilayers with 10 periods at wavelengths $\lambda=1.54\text{\AA}$.

6.3.2. Results of soft X-ray measurements

The reflection curves (the angle of incidence, Θ , equals to the angle of exit) were recorded in wide angular ranager for various energies. Far from the boron K-edge, the subsequent curves were recorded in energy steps of 1 eV, but closer to the edge in steps of 0.25 eV. The recorded intensities were normalized to the incident beam intensities to get the reflection curves. For seek of comparison, the angular values are transformed to the q -scale given by $q = cE\sin\Theta$, where E is the photon energy in keV, Θ the reflection angle and $c = 1.015 \cdot 10^{-3} (\text{\AA} \text{ eV})^{-1}$. Due to the large wavelength, the use of the 1st order Bragg peak of the ML is accessible only.

6.3.2.1. Boron K-edge

Fig.6.4 shows the measured reflectivity curves of MLs as a function of E (around the B K-edge) and the wave vector q (around the 1st Bragg peak). At energies lower than the boron K-edge ($\sim 188\text{eV}$), the peak profile doesn't show strong modifications due to the weak absorption, and the peak intensity increases with increasing photon energy. Beyond the edge, the intensity decays and the peak profile begins to show strong oscillations due to the high absorption. Fig. 6.4 shows the three different behaviours of reflectivity: (i) the low-absorption ML with a small number of periods (Ru/B₄C MLs with 10 and 17 periods); (ii) the low-absorption ML with a large number of periods (Ru/B₄C MLs with 60 and 63 periods) and (iii) the high-absorption ML with a small number of periods (W/B₄C with 10 periods).

All the measured surfaces demonstrate few important features: (i) the maximum intensity at 188eV (B K-edge), (ii) the secondary narrow peak near 194 eV due to the π^* -transition and (iii) the wide peak in 195–210 eV energy range due to the σ^* -transition (it is clearly shown for the low-periodical MLs). The antibonding orbitals are higher in energy (unstable) than the atomic orbitals from which it is composed (see, Fig. 5.5 for B₂). In addition, the Mo/B₄C ML has a set of weak peaks in a broad energy range during the interaction of atoms of boron with molybdenum at the surface layers. Even at room temperature, the deposited boron atoms penetrate into the neighbouring layers of molybdenum, thus changing its electronic structure, as shown by the dramatic transformation of the surface plasmon mode.

The B–Mo adsorbate system formed on the surface of ML is not stable at room temperature. It is dominated by the strong tendency of the boron atoms to diffuse into the bulk of the metal. The Auger uptake curve of the KLL boron line ($\sim 179\text{ eV}$) cannot be unambiguously drawn due to its strong intersection with the Mo MNV signal at 188 eV. The fact, that in this case, the shift of the B Auger line was not observed, is due at least to two reasons: (i) upon B–Mo chemical bond formation the B $1s$ and $2sp$ levels may shift simultaneously by about the same values, so the B KLL Auger transition energy does not change and (ii) the B KLL Auger line strongly intersects with the Mo MNV line, thus masking any possible changes of individual Auger lines.

On the other hand, the reflectivity W/B₄C ML shows a smooth profile, and the peak position slightly shifts near the B K-edge due to the high absorption of tungsten. In this case, the accuracy of the real part of refractive index will fall, and the absorption increases. (Fig. 6.4 *bottom*). In contrast with W/B₄C ML, the Ru/B₄C MLs consist of both low-absorption materials, and strongly sensitive to changes in the refractive index of boron carbide. In the case of a small number of period (Fig. 6.4 *top*), the refractive index can be determined by the described kinematical approach.

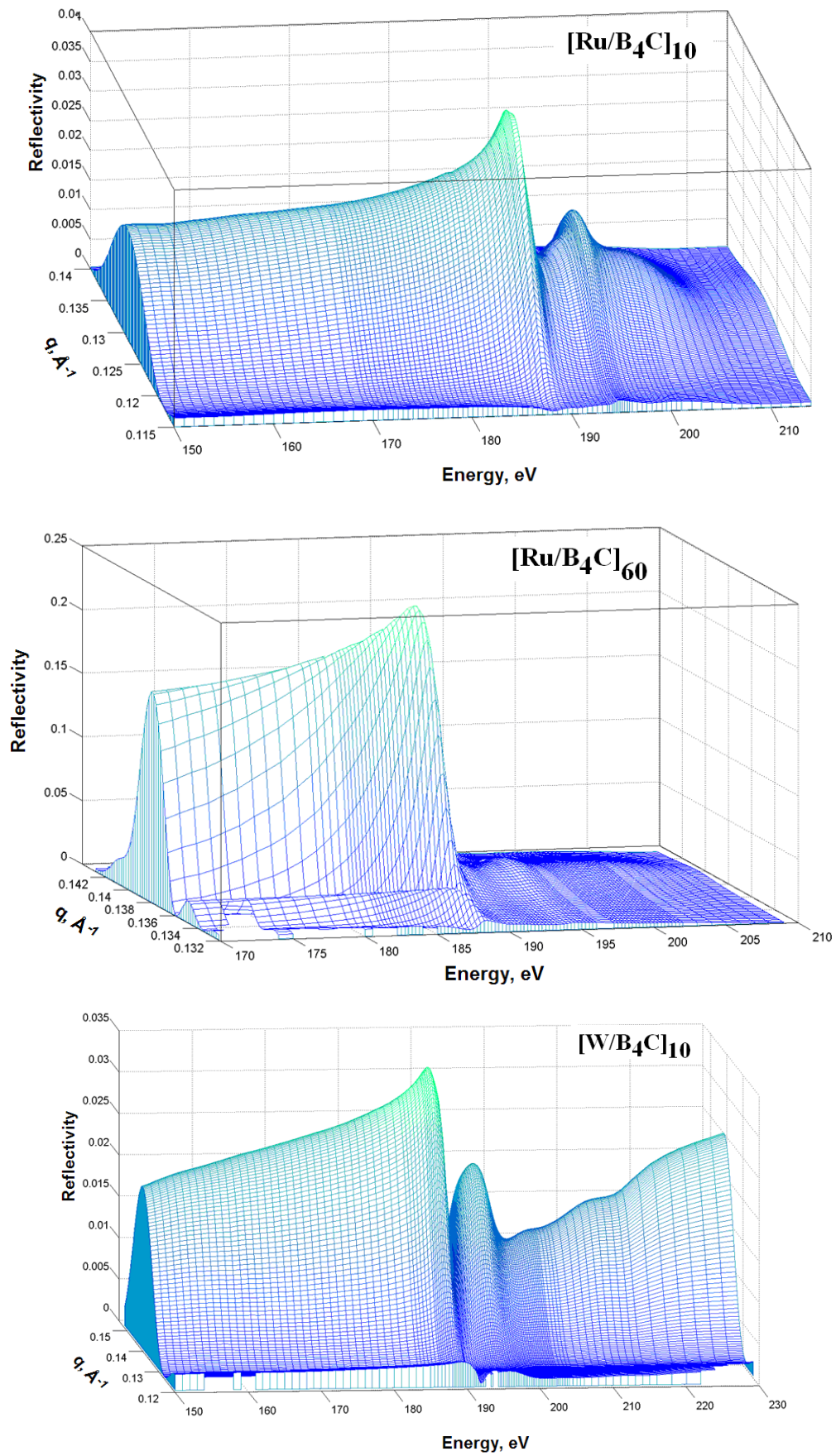


Fig.6.4 The reflectivity's surface of the Ru/B₄C multilayers with 10 periods (*top*) and 60 periods (*middle*), and W/B₄C ML with 10 period (*bottom*) via a function of incident energy (in eV) and the wavevector q_z (in \AA^{-1}).

The reflectance of Ru/B₄C MLs with periods 10, 17, 20, 60 and 63 periods at 1st Bragg peak are shown on Fig. 6.5, as function of the photon energy near B K-edge. All curves demonstrate two strong peaks corresponding Boron K-edge (188eV) and decreasing absorption in range between π^* - (194eV) and σ^* - transitions (195–210 eV).

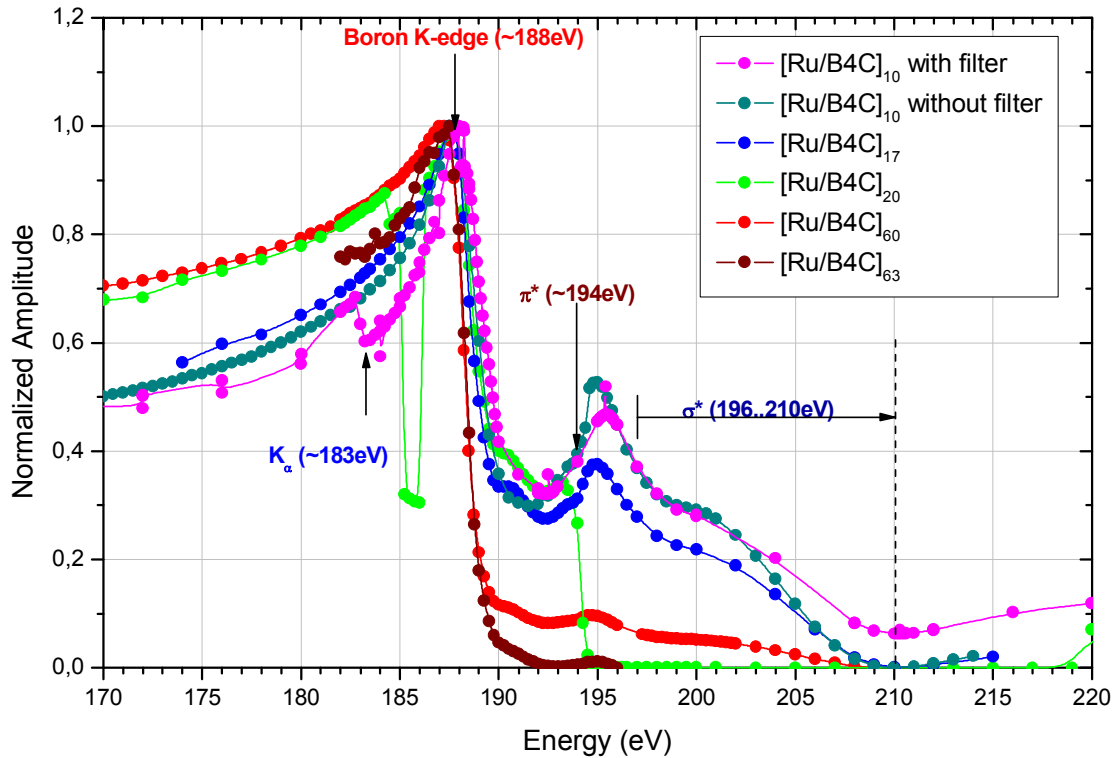


Fig. 6.5 The reflectance at the 1st Bragg peak as function of the photon energy E for different Ru/B₄C multilayers.

Fig. 6.6 shows the energy dependence of the angular position of 1st Bragg peak for these multilayers. To compare the obtained data, the all curves were subtracted on the respected value at 175 eV. The measured data demonstrated similar behaviour below the B Kedge and in range of π^* -transition (<194eV), although some curves had additional details, such as a peak near 185eV of the Ru/B₄C ML with 20 period, the weak peaks near 183 eV of the Ru/B₄C ML with 10 period. Below 195eV, the 10 periods ML has additional extremes due to the influence of the surface. The 20 periods of Ru/B₄C ML demonstrates a very weak scattering signal after 195eV (range of the σ^* - transition). At 60 and 63 periods MLs begin to play the role of multiply scattering of soft X-rays.

As mentioned earlier, the width of 1st Bragg peak can help to determine the absorption of B₄C material inside the multilayers. The behaviour of the FWHM of 1st Bragg peak near the B K-edge for various Ru/B₄C MLs is shown in Fig. 6.7. This parameter demonstrate the similar key details in a manner, as obtained for intensity (Fig. 6.5) and angular position (Fig. 6.6): the increasing at the B-Kedge (188eV), and the peaks at the π^* - and σ^* -transitions ranges.

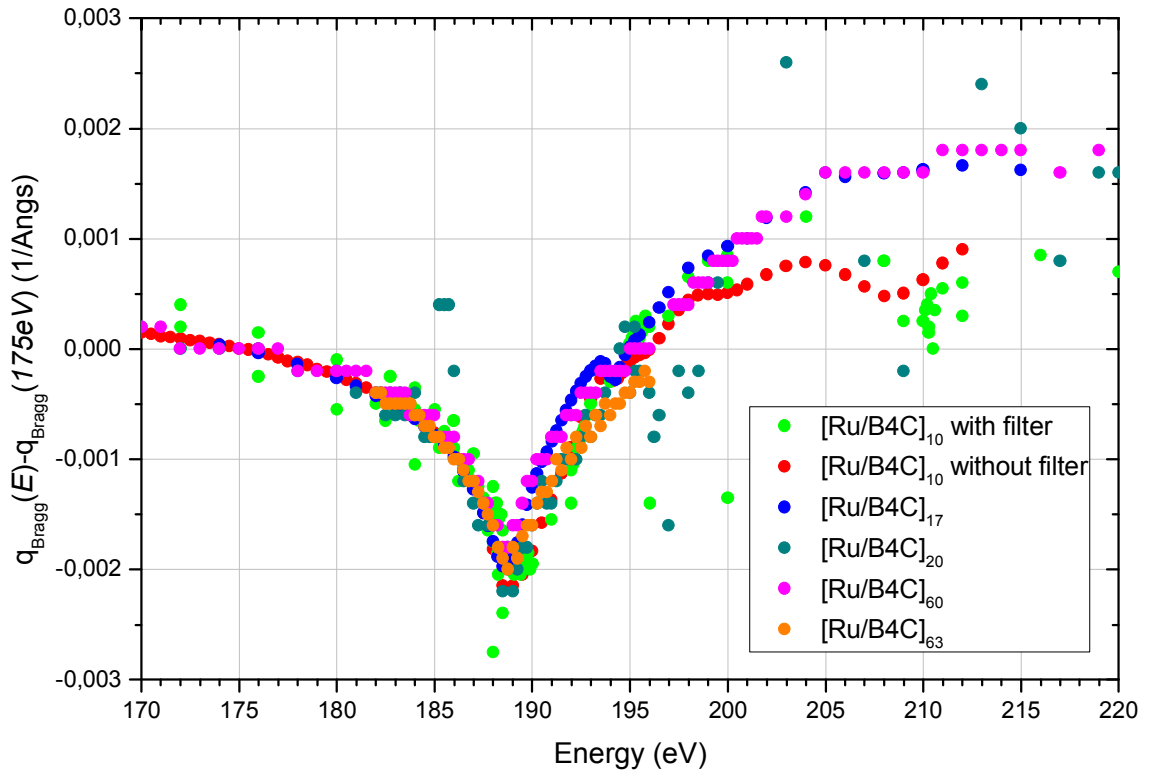


Fig. 6.6 The angular position of the 1st Bragg peak as function of the photon energy E for different Ru/B₄C multilayers.

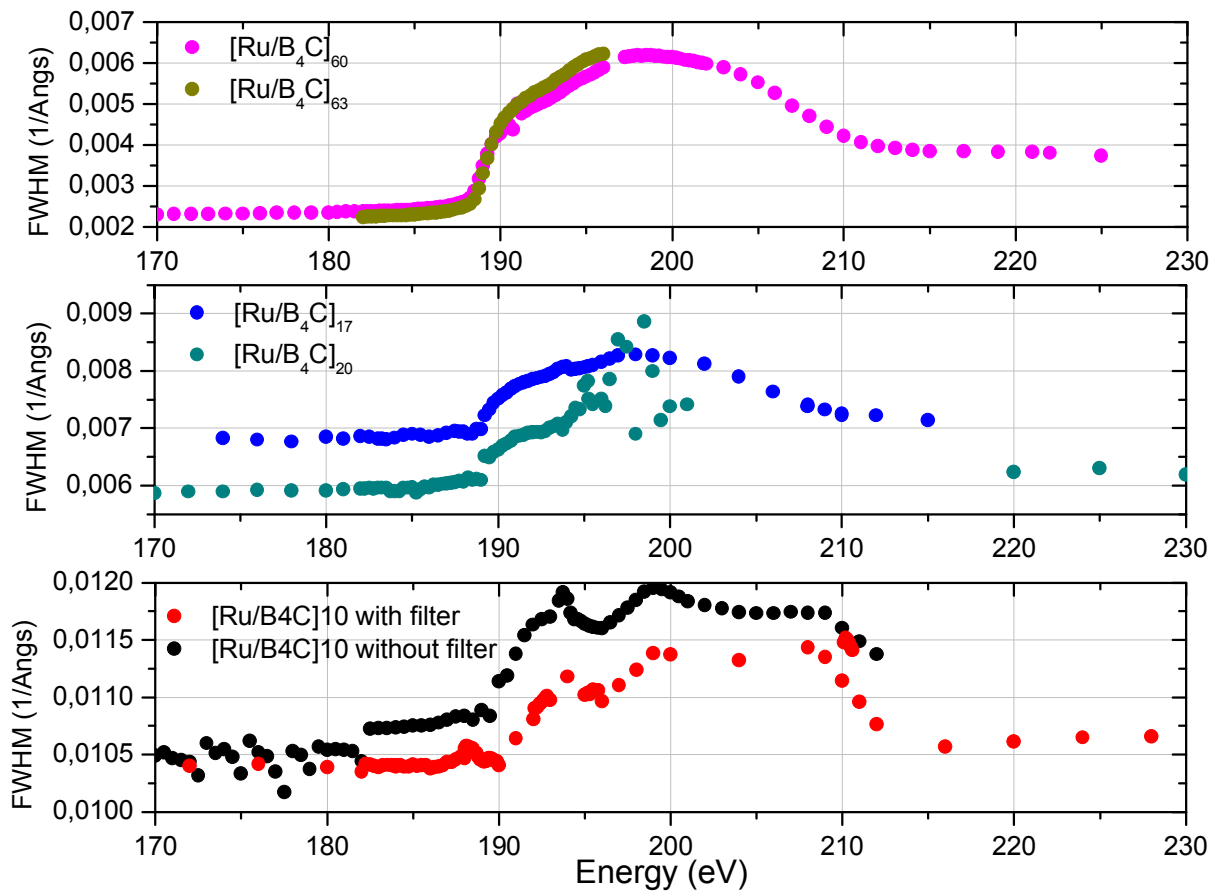


Fig. 6.7 The FWHM of 1st Bragg peak near B K-edge for the different Ru/B₄C multilayers.

There are also differences between the 10 and 60 (63) period Ru/B₄C MLs: (i) for the low period ML case, there is a weak peak near 188eV (atomic boron K-edge) and a strong peak at 190 eV (molecular boron K-edge), in the other case, the large period MLs have only a peak at 189eV (influence of the surface layers is negligible); (ii) the low period MLs demonstrate the separated peaks near 193eV during the π^* -transition, and a wide peak from 196 to 210eV during the σ^* -transition, whereas, the large period MLs showed the atomic-like behaviour during the multi-scattering of soft X-ray inside MLs and the influence of the surface layers is negligible. The FWHM of the 20 periods ML didn't be determined above 194eV in consequence of the weak scattering signal from this ML. Thus, the increase of the number of ML layers leads to a smooth function of the absorption without the additional features caused by surface effects.

To demonstrate the influence of the neighbouring metal layers and environment in the manufacturing process on the optical properties B₄C inside the MLs, we show the behaviour of various parameters, such as the intensity and the angular position at the 1st Bragg peak (Figs. 6.8 and 6.9, respectively), and the FWHM of 1s Bragg peak (Fig. 6.10) near B K-edge for the Ru/B₄C and W/B₄C MLs with 10 periods.

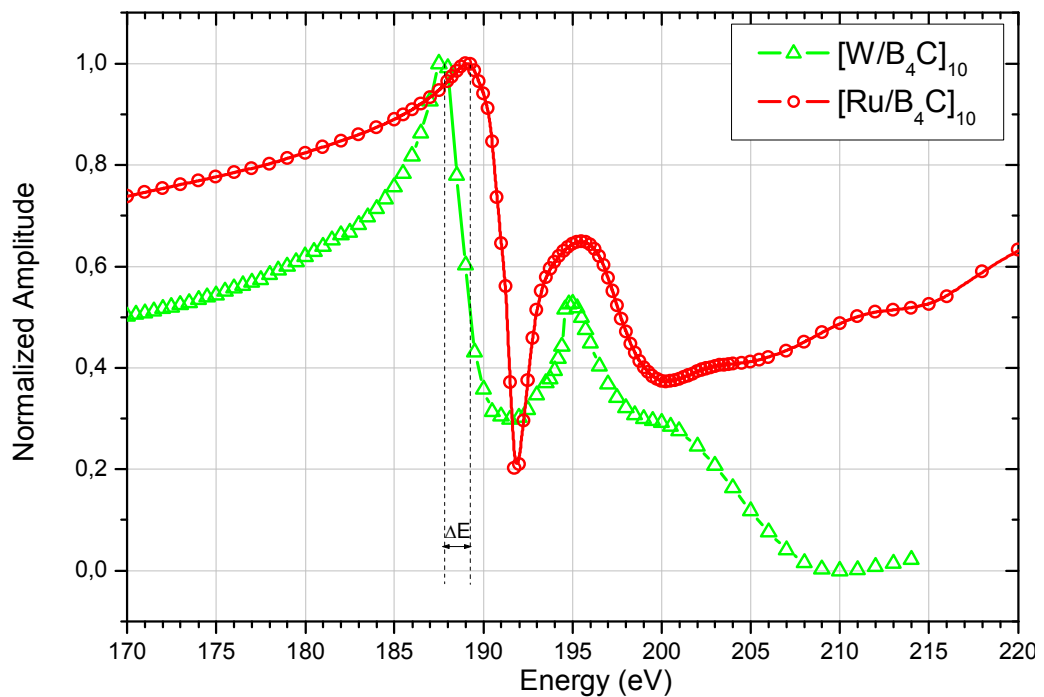


Fig. 6.8. The reflectance at the 1st Bragg peak as function of the photon energy E for different Ru/B₄C and W/B₄C MLs with 10 periods.

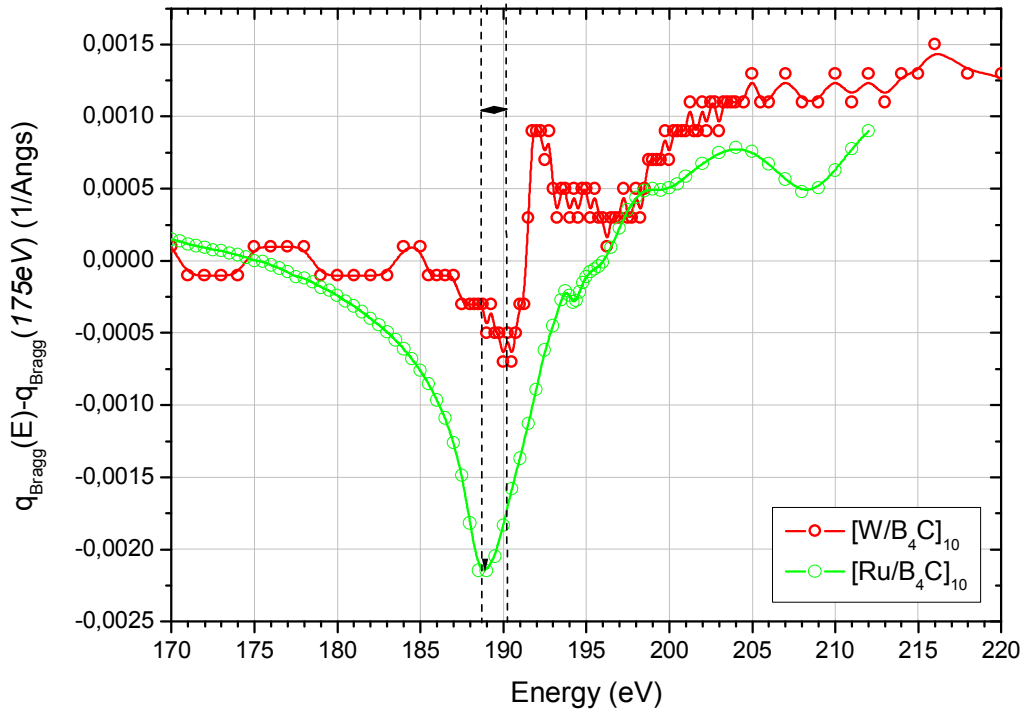


Fig. 6.9 The angular position of the 1st Bragg peak as function of the photon energy E for the W/B₄C and Ru/B₄C MLs with 10 periods.

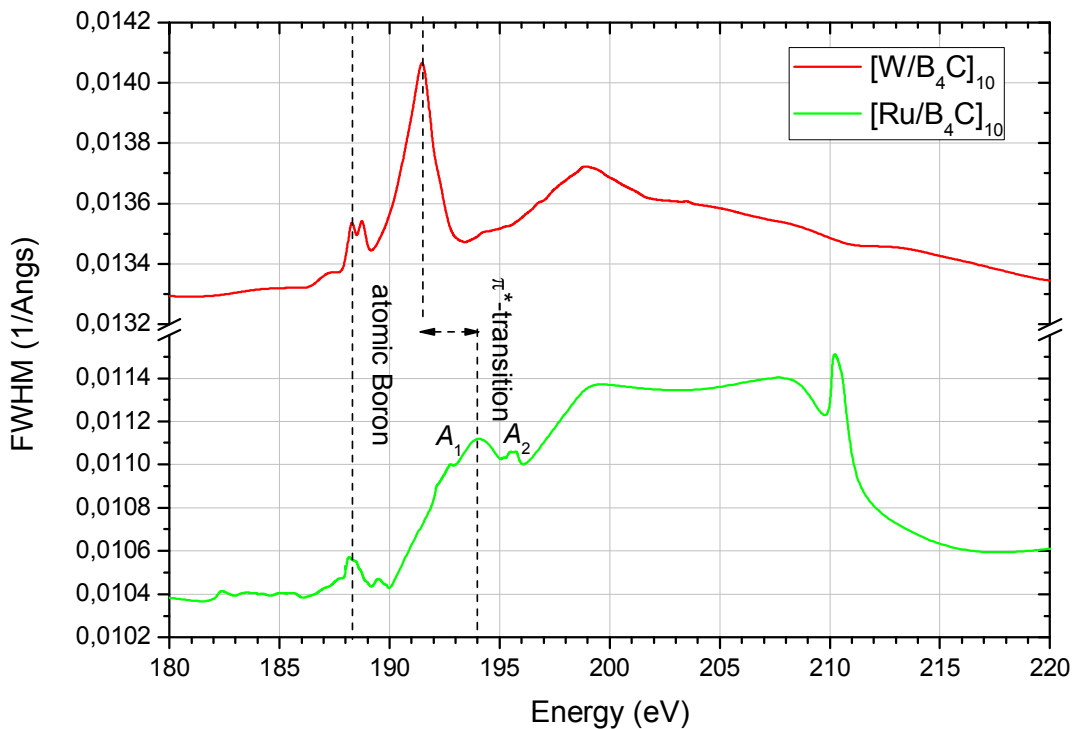


Fig. 6.10 The FWHM of 1s Bragg peak near B K-edge for the W/B₄C and Ru/B₄C MLs with 10 periods

Both MLs contain the atomic boron, and we obtained the corresponded peak at ~ 188 eV (Fig. 6.10). The maximum of reflectivity and minimum of the angular position of the 1st Bragg peak for the W/B₄C ML shift by of about 1eV to upper energies, relative to the these parameters for the Ru/B₄C ML (Figs. 6.8-6.9). In addition, in the case of the Ru/B₄C ML, we received

additional peaks (A_1 and A_2 in Fig. 6.10), corresponding to oxygen. On the other hand, the W/B₄C ML were fabricated using N₂ gas, and the layers may contain nitrogen. The peak corresponding to the π^* - transition of B₄C inside W/B₄C ML, is more obvious, and the energy shift is about 3 eV to the lower energies (Fig. 6.10). In this sample, the influence of oxygen is minimal (see, Fig. 5.7) due to the use of the N₂ gas in process of fabrication and the top layer is tungsten. It should be noted, that the replacement of oxygen into nitrogen can lead to the formation of B-N bonds.

The optical properties of boron carbide inside Ru/B₄C MLs we can determinate using the approach described in § 5.3.2. It is expected, that the density of the components of ML will differ from the bulk density. For example, the density of the lanthanum films in the La/B₄C multilayer corresponds to 5.0 g/cm³ ($d_{La} \approx 25\text{\AA}$) [127] and 5.5 g/cm³ ($d_{La} \approx 30\text{\AA}$) [128] which is less than the bulk density to be $\rho_{bulk}=6.17\text{ g/cm}^3$. On the other hand, the density of the boron carbide films can vary between 1.8 g/cm³ and 2.57 g/cm³, depending on the chemical composition as B_{15-x}C_x and the film thickness ($\rho_{bulk}=2.0\dots2.52\text{ g/cm}^3$). R. Soufli *et al.* [96] used the atomic composition of 74% of boron, 20% of carbon, and 6% of oxygen for the density of 2.28 g/cm³ to describe the optical properties of boron carbide inside the films with thicknesses from 50 to 100 nm. This means that the reflectivity and the other optical parameters of a ML strongly depend on the material density which is related to the use of the respective deposition technique. Also, the metallurgical transitions at the Ru-B₄C and B₄C-Ru interfaces can result in different values of interlayer-roughness evaluated from the hard and soft X-ray measurements.

Using the tabulated Henke's data for applied metals [118], the calculated β -values of B₄C for the various MLs are displayed in Fig.6.11. The most remarkable difference between the samples is that the onset of the increase in β for the low periods sample is shifted by about 2-3 eV to higher energies compared to the expectations made by Henke's table. In fact, the K-edge is separated on the weak peak near 188 eV (*atomic boron*) and the shifted K edge of molecular boron (B-C, B-B and B-O bonds). Also, the values of π^* -transition peak decreases with increasing number of ML period.

Above 190eV the scattering signal from the large period MLs is very weak (decreasing about two orders of magnitude) (Fig.6.4 *middle*, and Fig. 6.5). This means that the scattering signals are the measure of the first few tens of ML periods only. In this case, the absorption length is less than the thickness of the large period MLs. As a consequence, the rocking curves become very narrow and less intense, and the error in this range is larger than those determined at energies below the K-edge.

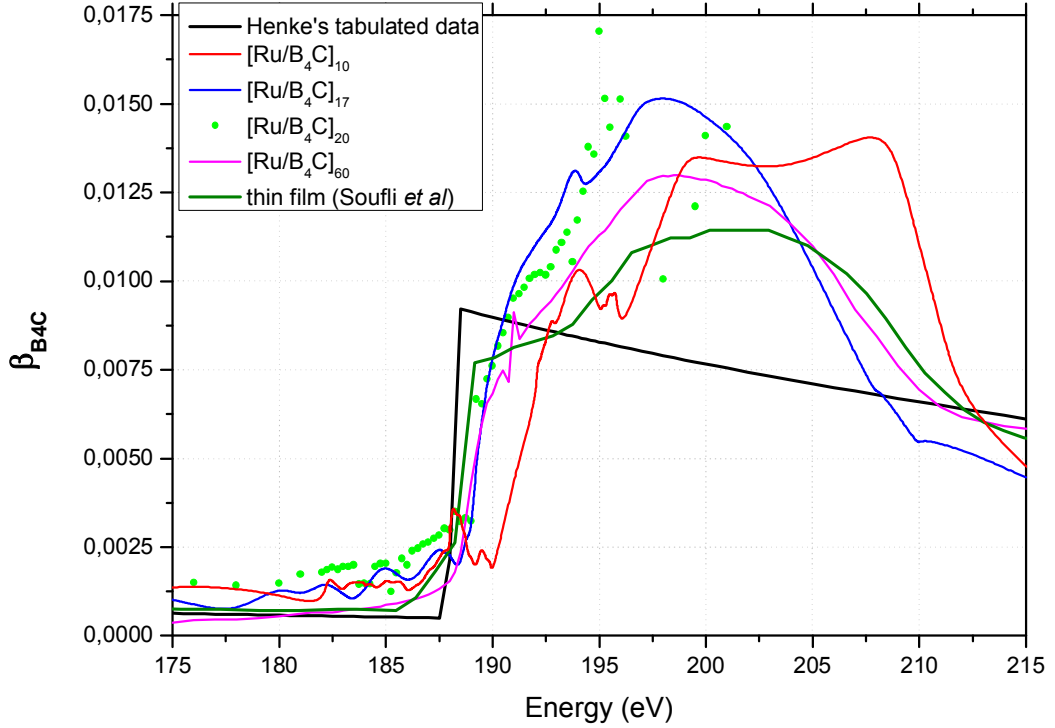


Fig. 6.11 Near-edge absorption spectra at the boron K-edge of B_4C calculated from the experimental diffraction spectra of Ru/B_4C ML for various fixed energies, and obtain from Henke's tabulated data (*black line*). To compare with obtained data, the values for B_4C thin film from work [96] also are present.

The additional peaks found for the 10 period ML can be explained: the K emission line of free atom of boron is found at 183eV, two different peaks centered at 188eV and 189.5eV are related to the $B(1s)$ peaks of pure boron atoms, B-B and B-C bonds of boron carbide. Two small peaks for $B(1s)$ observed at 192.7 eV and 195.5 eV could be associated with B-O and B=O bonds due to the presence of physisorbed oxygen at the surface and inside the first layers of our sample. Finally, a narrow edge peak ~ 194 eV, assigned to the transition of B 1s electrons to the unoccupied B 2p states (π^* - transition), and a wide peak of 198-210 eV to the transition of B 1s electrons to the unoccupied B 2p σ^* states (σ^* - transition) for B_4C .

The results demonstrate good agreement with experimental data of other authors. For example, in [129] the absorption spectra display the different functional behaviour above Boron K-edge measured in transmission and by detecting the photocurrent in the reflection due to the high surface sensitivity of the photocurrent measurements.

If the ML period is known, for example, from the experimental data for the hard X-rays (table 6.1), δ_{eff} follow from Eqs. (6.5 or 6.6-6.7), using the measured values of the wave vector q and energy E (see Fig. 6.6). The resonant δ_{B_4C} value can be determined by Eq. (6.5) using the structural parameters of the investigated ML and the non-resonant δ value for Ru. Since, δ_{Ru} varies linearly in the measured energy range it can be taken from the Henke's tables [118].

Fig. 6.12 shows the energy dependence of the δ_{B_4C} , determined from experimental data given in Fig.6.6. To fit with the tabulated data for B_4C , our values were rescaled at the two

extreme energies far below ($\sim 170\text{eV}$) and above ($>220\text{eV}$) the K-edge. The best data fitting for δ_{B_4C} are obtained if the densities of both multilayer materials (ruthenium and boron carbide) are reduced to a value of 80% compared to bulk density.

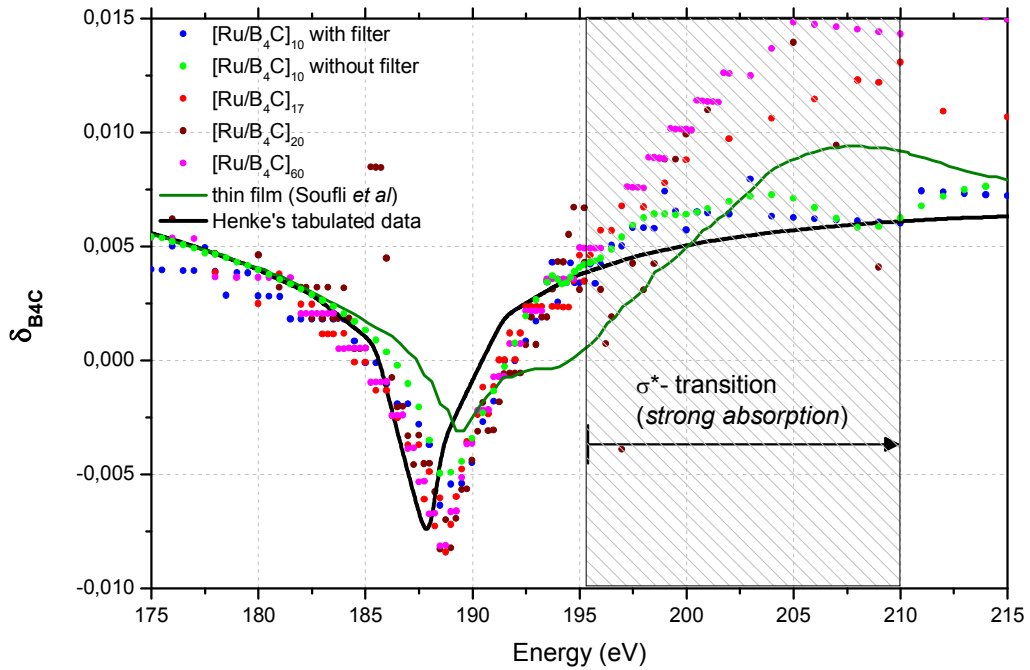


Fig.6.12 Refractive index $\delta=1-n$ for B_4C inside Ru/B_4C MLs with various periods (*circles*) and obtained from the measured data. *The black lines* are shown the tabulated δ values for B_4C from Henke's tables [118]. The obtained δ_{B_4C} (*red line*) for the magnetron-sputtered boron carbide thin films by transmittance measurements from work's R. Soufli *et. al.*[96]

As for $\beta_{B_4C}(E)$, comparing the tabulated data for the elemental boron with the experiment the minimum of $\delta_{B_4C}(E)$ is shifted by 1.2 eV to higher energies (from 187,8eV to 189eV). This shift is larger than the experimental uncertainty of 0.2eV. Assuming stoichiometric B_4C , this minimum is associated with the electron transition from B 1s state into the unoccupied B 2p π^* states. This transition energy can slight vary for the non-stoichiometric B_4C , especially boron-depleted boron carbide, or for boron oxides [96, 97]. In the case of the 10 periods Ru/B_4C ML there are additional local minima within the energy range between 183eV to 188eV probably originated by elemental boron (183eV is the transition from K- to L-shells; $\sim 187,8\text{eV}$ is the binding energy for pure boron). Additional features have been found close to 204 eV (maximum) and 210 eV (minimum) resulting from the transition of B 1s electrons into the unoccupied B 2p σ^* states. These features are not visible for the large period samples. Also during the strong absorption in the range σ^* -transition range (195...210eV) and multiply scattering, it is necessary to include the corrections on strong absorption effects for a large number ML (see Eqs. 6.5-6.6).

6.3.2.2. Carbon K-edge

In an analysis of the boron K-edge, we have found that in contrast to the oxygen Ru/B_4C MLs, the W/B_4C ML containing nitrogen due to the fabrication in N_2 gas. There is a question about the

interaction of carbon atoms with boron, and oxygen/nitrogen inside the B_4C material of ML. To answer this question, we can analyse the experimental data of these MLs near the carbon K-edge.

Fig. 6.13 shows the maximums of measured reflectivity curves of Ru/ B_4C and W/ B_4C MLs with 10 periods as a function of E (around the C K-edge) at the 1st Bragg peak. At energies lower than C K-edge (~ 284 eV) the peak profile doesn't show the strong modifications due to weak absorption and the peak intensity increase with increasing the photon energy. In this range the contrast between Ru and B_4C is very small and the Ru/ B_4C ML has weak reflectivity maximum ($<0.15\%$). On the other side, the maximum reflectivity of W/ B_4C ML is near 3%. In the both cases, the MLs demonstrate the similar features: the π^* -transition at 285 eV and a broad σ^* -transition centred at 290 eV.

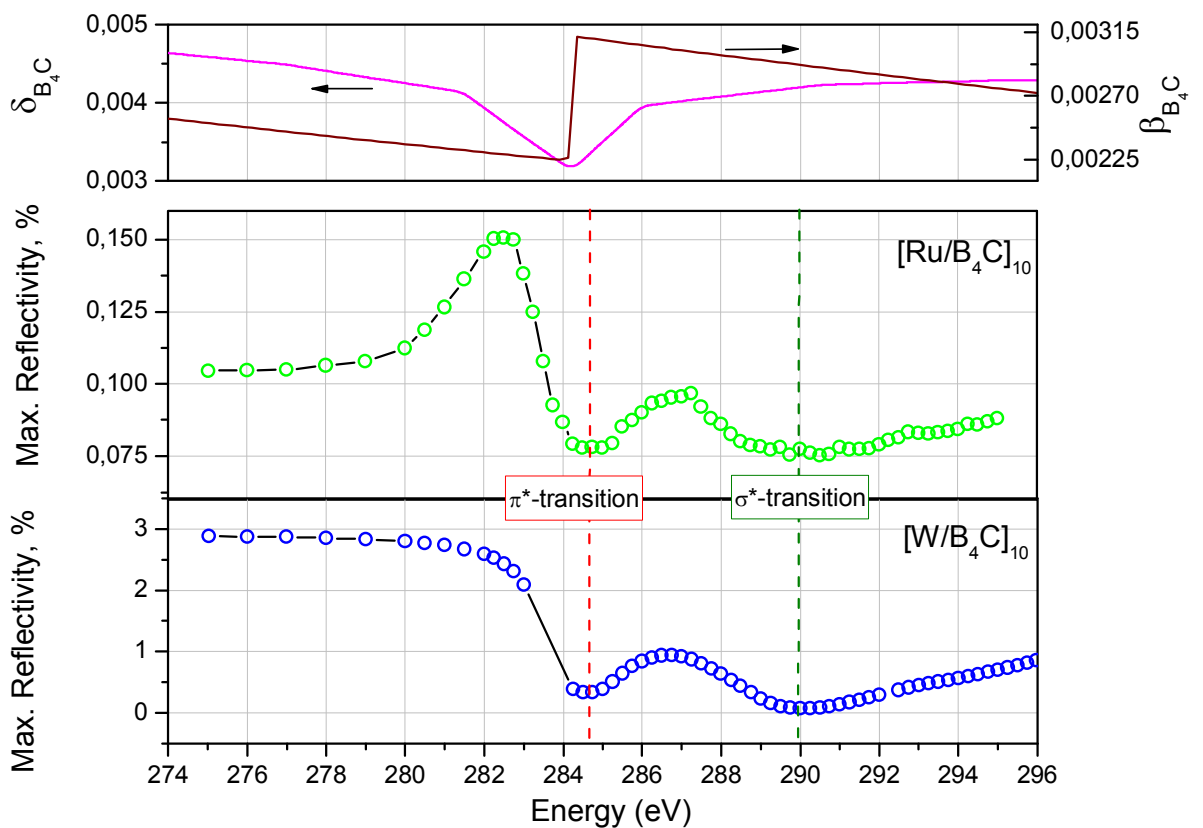


Fig.6.13 The maximums of reflectivity of the Ru/ B_4C (middle) and W/ B_4C MLs (bottom) with 10 periods near Carbon K-edge via a function of incident energy. The tabulated data of refractive index $n=1-\delta+i\beta$ for B_4C is presented also (top).

6.3.2.1. Nitrogen K-edge

We found the optical properties of the B_4C material inside the W/ B_4C ML are changed near the boron K-edge due to the formation of the B-N bond. Now we can investigate this sample near the nitrogen K-edge. Fig. 6.14 shows the maximum of reflectivity of the W/ B_4C ML with 10 periods as a function of E around the N K-edge at the 1st Bragg peak. The measured data demonstrated behaviour similar for B and C Kedges (see Figs 6.4 and 6.13): there is a π^* -

(~401eV) and σ^* -transitions (~405eV), but also it was obtaining the change at about 397 eV, attributed to N-B bonds. The maximum reflectivity of W/B₄C ML is near 4%.

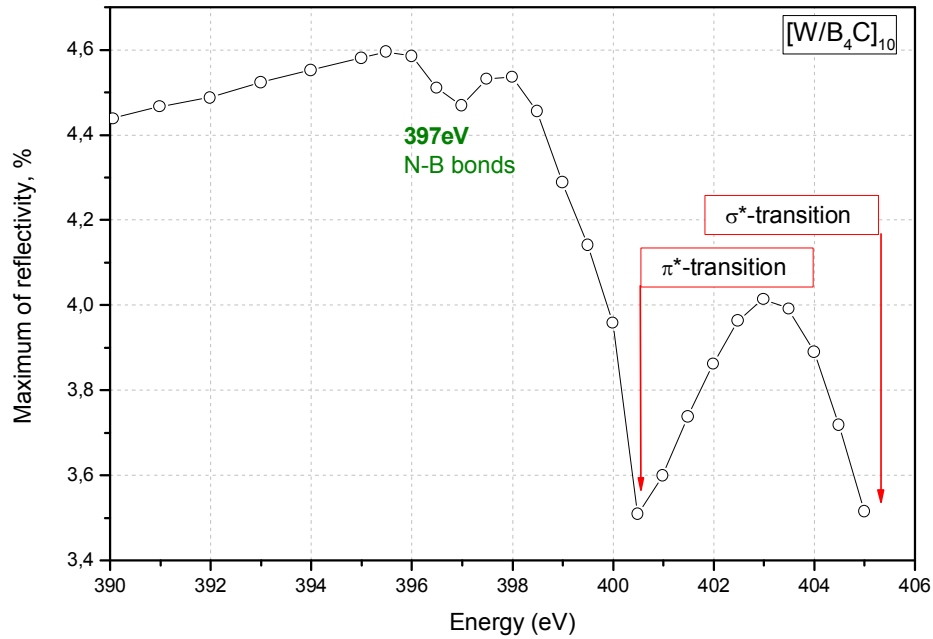


Fig.6.14 The maximum of reflectivity of the W/B₄C:N₂ ML with 10 periods near Nitrogen K-edge via a function of incident energy E .

In summary, the optical properties of boron carbide inside of Me/B_4C multilayers have been derived by an energy-resolved photon-in-photon-out method using Bragg reflection. In contrast to the hard X-ray measurements providing the mean values of the optical parameters only, the soft X-ray reflectivity can give detailed information for MLs with thickness up to several tens of nanometers. In addition, measurements close to the resonance edges probe the chemical state of the respective constituent accompanied with a high sensitivity of changes close to the sample surface. Our measurements clearly show that the fine structure of K-absorption edge changed due to the chemical nature of the absorber element.

The penetration depth of the MLs is strongly reduced beyond the B K-edge and reaches a few tens nanometers only. In this energy range we can use the kinematical approximation as long as the total thickness of the ML is small. In the case of the kinematic approximation δ and β can be derived independently from each other. In our case, this approach is valid for the low-period Ru/B₄C MLs. For thicker samples, the multiple scattering effects within the ML become important, requiring a full dynamical theory, like Parratt's recursive method. In the dynamical case the derivations of δ and β are no more strictly independent, because one has to know δ in order to find β from Δq .

The results for Ru/B₄C and W/B₄C MLs with 10 periods show the similar key features in the optical properties of the B₄C layers, such as (i) the atomic boron K-edge (~188eV), (ii) the π^* - and σ^* -transitions of boron, and (iii) the π^* - and σ^* -transitions of carbon. The W/B₄C ML,

fabricated using N₂ gas, show the additional details at about 397 eV, attributed to N-B bonds, the π^* - and σ^* -transitions of nitrogen, and the absorption peak of the π^* -transition of boron shifts by 2 eV to the lower energies compared to the Ru/B₄C ML. In turn, the results for the Ru/B₄C ML demonstrate the existence of certain amount of oxidized boron probably in the layers close to the surface.

In all chemical bonds the electronic charge density near the boron atom is reduced due to the higher electronegativity of the bonding partner's, as carbon, oxygen or nitrogen. The B 1s peak is shifted from ~188eV for the B-B bond to higher binding energies: with carbon (~189eV) and nitrogen (~191eV) as neighbour and to much higher energies with oxygen (~194eV) as neighbour. This shift to higher energies doesn't present in the large numbers ML samples. Here $\delta(E)$ and $\beta(E)$ are very close to the values of Henke's table predicted for elemental boron. Therefore we can conclude that the majority of boron and carbon are not bonded to stoichiometric B₄C. The films may be decomposed into metallic boron (seen at 188eV), oxide boron and the different compositions of boron carbide, such as the icosahedra B₁₁C (or B₁₂) with different bridges C-B-C, C-B-B and C-C-C.

The measurements clearly show the fine structure of K-absorption edges changed due to the chemical nature of the absorber element. The effect is seen in both parameters of the refraction index, δ and β but more pronounced in the absorption spectra. The evaluated energy dependencies of δ_{B_4C} and β_{B_4C} show Kramers –Kronig relation comparing features in Figs. 6.11 and 6.12. So the maximum found in δ_{B_4C} at about 205eV is related to a plateau in β_{B_4C} . On the other hand, the feature at 193eV in β_{B_4C} is accompanied by a slope in δ_{B_4C} . The relations are not so obvious in other energy ranges mainly caused by different sensitivities of both measurements.

Chapter 7

Reflection of soft X-ray FEL pulses by periodical multilayers

FLASH operates in the soft X-ray regime and the radiation from the FEL has the spontaneous nature, and can be described by the FEL theory. P. Hau-Riege *et. al* [39, 40] have shown that on the fs- timescale, the reflectivity of the multilayer excited by the FLASH pulses can be described by conventional approaches, as well as for continuous radiation. In the case of low intensive FLASH pulse, we can directly use the LORT (Chapter 3) with a frequency response function of ML calculated by one of the theoretical approaches (Chapter 4) or/and using the measured data for the continuous synchrotron radiation (Chapter 6). Effect of high-intensity of the FEL pulse leads to a time-dependent frequency response functions of the ML, and strongly complicate of the simulation because of the limited information about the processes in the matter during the interaction of the FEL pulse with ML.

The study of the time dependent response of the ML to the X-ray pulse can provide insights into the process of interaction of a highly intense FEL radiation with matter. Using an appropriate geometrical setup of the experiment, the time structure of the reflected pulse can be transformed into the spatial coordinates of the position-sensitive detector [131, 132].

7.1. Basic formalism

The approach, of describing of the time-space transformation of the incident pulse train of FEL at 6.4 nm, was introduced in [131]. Based on the LORT [33, 34] described in §3.2, the time-dependent interaction of an fs-FEL pulse with the interfaces inside the ML can be described. In the case of FEL radiation, the incident pulse consists of a train composed by ultra short sub-pulses. FLASH, for example, generates the FEL pulses with 20...50 fs pulse length and duration of sub-pulses of about 2-3 fs at an average wavelength of 6.4nm [31, 32]. The numbers of spikes in the spectrum is in average equal to the numbers of spikes (*coherent wave packets*) in the time domain [26]. Using this information, single incident pulse can be simulated by a combination of several Gaussian functions with various random-generated parameters. Coherent radiation with energies between 160...240 eV and 0.5...1.0% bandwidth (FWHM) as provided by FLASH [31, 32] has been considered.

This energy range requires the scattering object with lattice parameters in the range of a few nanometres, as provided by a periodical ML structure. ML response to the incident pulse train can be evaluated by the following steps: first, each incident sub-pulse ('spike') in time range is described by a Gaussian function, and subsequently, a pulse train by a combination of several Gaussian functions

$$E_{inc}(t) = \sum_{m=1}^M k_m \cdot \frac{1}{\sigma_m \sqrt{2\pi}} \exp\left(-\frac{(\tau - \tau_0^m)^2}{2\sigma_m^2}\right) \exp(-i\omega_m t), \quad (7.1)$$

where σ_m is the standard deviation, τ_m is the mean value, ω_m is frequency and k_m is amplitude for m -th Gaussian function. Next, the time structure of an incident pulse train is spectrally decomposed using Fourier transforms:

$$E_{inc}(\omega) = \frac{1}{\sqrt{2\pi}} \int_{-\infty}^{+\infty} E_{inc}(\tau) \exp(i\omega\tau) d\tau. \quad (7.2)$$

Finally, within the spectral range of emission each Fourier component of the incident pulse amplitude is multiplied with the complex reflection amplitude of the ML followed by inverse Fourier transformation in order to find the time response of reflected pulses

$$E_{ref}(t) = \frac{1}{\sqrt{2\pi}} \int_{-\infty}^{+\infty} r(\omega) \cdot E_{inc}(\omega) \exp(-i\omega t) d\omega. \quad (7.3)$$

In this energy range, the ML structures prepared by repetitions of thin layers of two different materials are well suited. Typical MLs for soft X-rays consist of a periodic stacking of a high-refracting (Mo, Ni, Cr, Fe, V) and low-refracting materials (C, Si, B₄C). By various combinations of these materials, one can tune the optical properties of the respective optical element in terms of transmission, absorption and reflection. The shape and the total scattering power at fundamental Bragg reflections are influenced by the number of stacked bi-layers [58, 120, 121]. In 200 eV range, the ML reflectivity is low for a few reasons. First, the optical constants for this wavelength are very similar (see Table 7.1) and the combination of the two materials does not provide a large scattering contrast. Secondly, the absorption coefficient is large for most materials. Both peculiarities limit the effective penetration depth into the ML. Thirdly, in order to tune the 1st order Bragg peak of the ML to a scattering angle 2Θ why the bi-layer period must be smaller than 10nm. Under these circumstances, the interface roughness of a few atomic layers can significantly reduce the reflectivity (*Debye-Waller factor*).

Usually, the combinations of the high-refracting and low-refracting materials are well suited as the MLs for a defined wavelength in the soft X-ray range. These MLs are optimized for high reflectivity and are widely used in X-ray optics. However, we applied other criteria to select the ML components. In order to generate larger penetration depth into the ML, both materials must be with minimal absorption in the energy range of application. The following table 7.1 and, particularly, the β -values, we selected two perspective materials - Ru and La for application at 194 eV. Results for La/C and La/B₄C MLs were already shown in [131, 132]. Using MLs with exceptional low absorption, the interaction length of the incident pulse with the ML is long and

after transformation into the spatial coordinates, the incident pulse can be visible at a spatially resolved detector. In particular, this scheme will be useful to probe a deviation from the reflectivity which is expected, when the energy density of the FEL pulse exceeds a certain level.

Table 7.1 Correction to refraction index ($n=1-\delta+i\beta$) for different materials at 193,75 eV with increasing absorption coefficient.

Element/Compound	δ	β
C	0.0079	0.00063
La	0.0138	0.00097
Sc	0.0065	0.00232
Nb	0.0084	0.00252
Mo	0.0113	0.00278
Ru	0.0167	0.00378
RhRu	0.0170	0.00393
Y	0.0016	0.00541
V	0.0159	0.00579
Cr	0.0197	0.00761
Si	0.0077	0.00838
B ₄ C	0.0028	0.00855
B	0.0010	0.00996
Fe	0.0222	0.01165
Ni	0.0237	0.01694
W	0.0152	0.01903

Fig. 7.1 shows the general setup of a reflectivity experiment. An incident FEL pulse hits the ML at a fixed incidence angle Θ and penetrated into the material. Because the pulse becomes partially reflected at each interface ones after another, the detected signal is stretched by a length, which equals the penetration depth into the material. This stretching effect can be optimized by the optical properties of the ML. For geometric reasons we prefer a scattering geometry with scattering angle of 90° at first scattering maximum of the ML. However, the degree of stretching can be increased by using an oblique scattering geometry, where the ML is cut by an angle α (see §4.2).

7.2. Numerical simulation of fs-pulse responses from multilayers

Now we consider two different types of MLs: (i) both low-absorption materials La and C and (ii) Ni and C as materials with high scattering contrast. La and Ni have the difference absorption proprieties in this energy range. For $\lambda=6.4$ nm (193,75eV) the ML period has to be $d=4.62$, that the first order diffraction maximum is appearing at $2\Theta =90^\circ$.

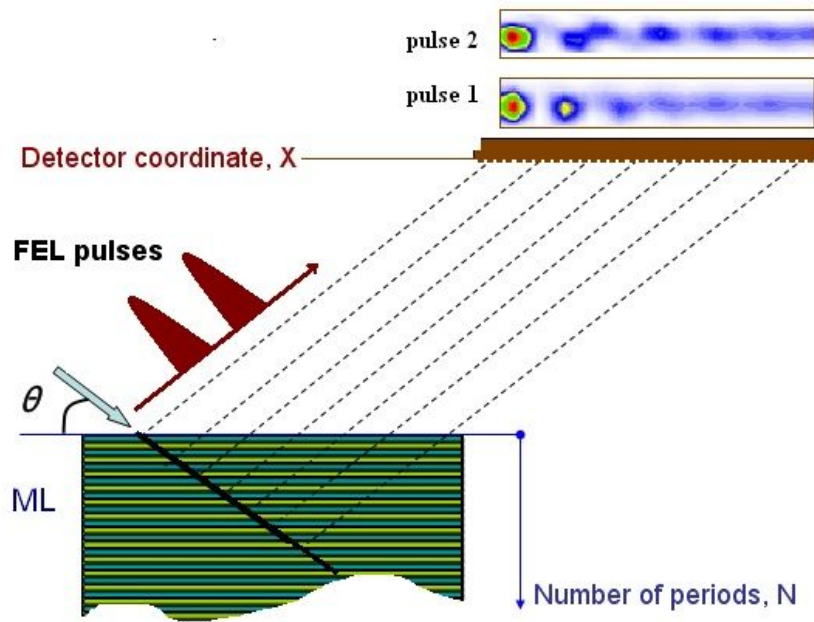


Fig. 7.1 Experimental set-up for time-space transformation of incident fs-pulses. The incident pulse is stretched accordingly to the absorption length of radiation. The spatially varying reflectivity of the ML is measured with the changes of intensity along the detector coordinate X.

The variations of the reflectivity spectra for both types of MLs are shown in Fig.7.2 as a function of the number of periods. The calculation has been performed by Parratt's recursive formalism (§ 4.1.1) considering a thickness ratio of 0.5 and a continuous, strictly parallel VUV radiation. Due to high absorption of Ni-layers, the reflectivity curves of the Ni/C MLs saturate after a penetration of about 40 periods at a maximum reflectivity of about 18 percent and don't show any internal structure.

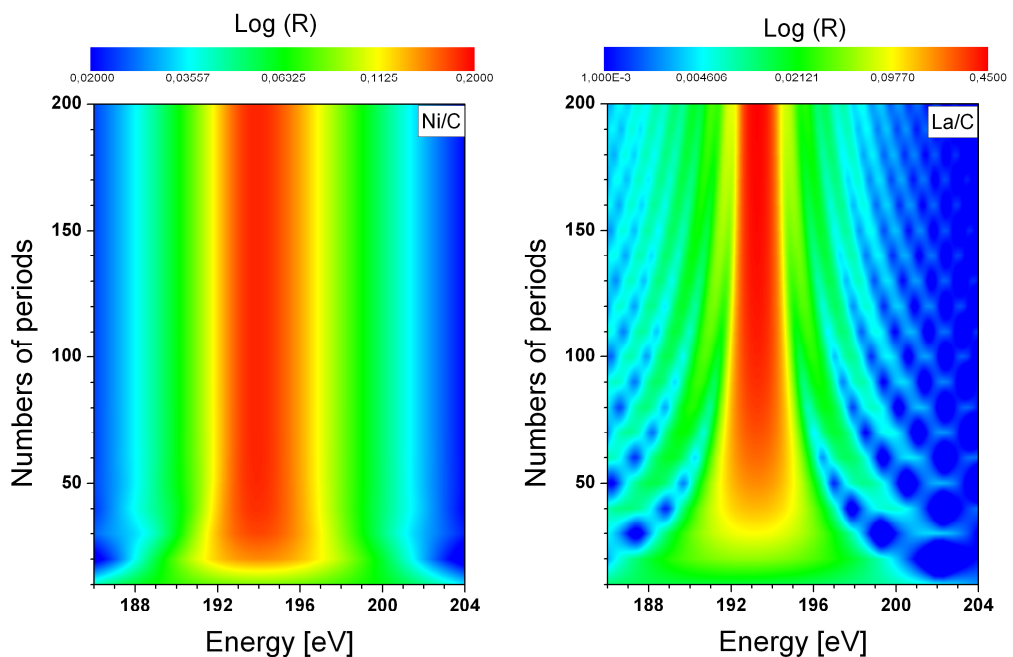


Fig. 7.2 Calculated reflectivity of MLs as a function of energy and number of bi-layers. High-absorbing Ni/C, *left* and low-absorbing La/C, *right*.

On the other hand, the La/C ML intensity increases with the number of periods reaching a maximum of about 40 percent for the MLs with more than 120 periods. In addition, the thickness oscillations decrease with increasing number of periods. The energy width of central maximum has a width of about 6 eV for Ni/C and about 1.5 eV for La/C ML at large numbers of bi-layers.

First, we consider the ML response to a Gaussian pulse of 2 fs duration (single spike of a FEL pulse) for La/C and Ni/C MLs as a function of the number of periods, N at a fixed incidence angle of $\theta = 45^\circ$. The low- and high-absorbing ML responses are shown in Fig.7.3. As in Fig.7.2, there are the essential differences in the response of these MLs seen (Fig.7.3b,c). When the initial pulse strikes the ML with different numbers of periods, the response quite fast $N=40$ for the high absorbing Ni/C MLs. Due to nearly complete absorption of the pulse within the first few layers, the duration of the reflected pulse is approximately the same as the initial one (fig.7.3a,b).

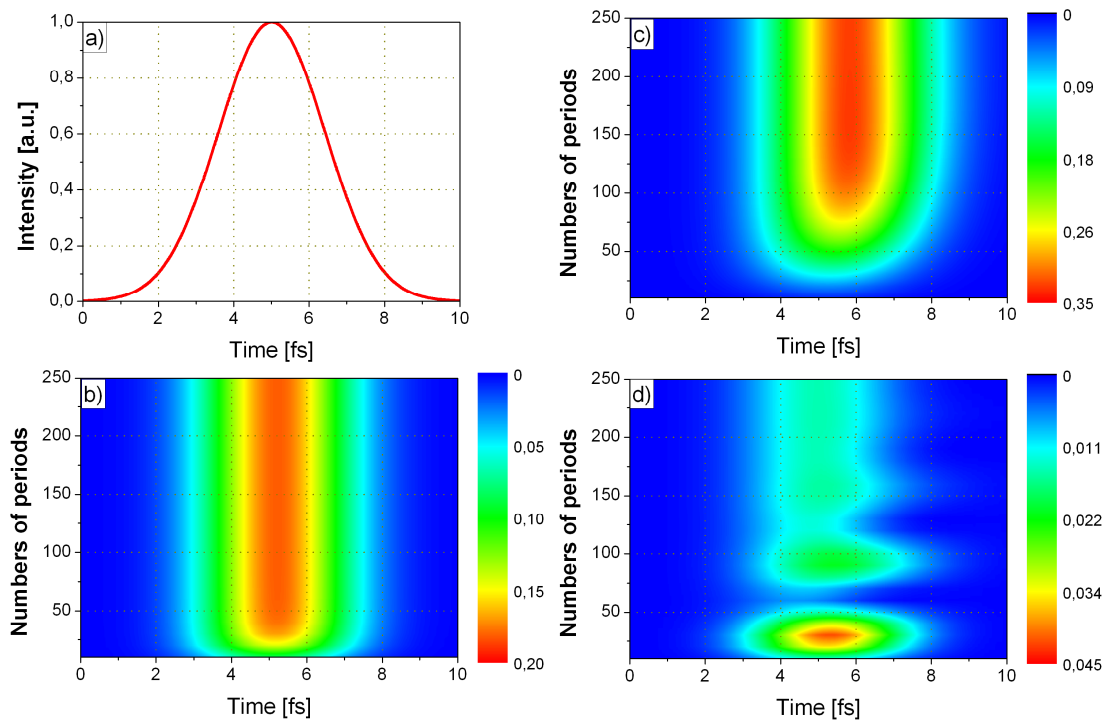


Fig. 7.3 Incident single pulse (a) and time-responses from various periodical Ni/C(b) and La/C (c,d) MLs. The duration of incident single Gaussian pulse is 2fs and the energies are 193,75eV (b,c), 191 eV (d).

In contrast to this the reflected pulse is expanded up to 2fs compared to the initial pulse for the low-absorbing La/C MLs. The pulse expansion increases with the number of periods, reaching certain saturation at $N=120$ for La/C ML. Maximum reflectivity of about 28% is reached at $N \approx 100$ (fig.7.3c). In all three cases shown in Fig. 7.3, the energy of the incident pulses coincides with the maximum of the 1st ML Bragg peak of the reflection curve at given angle of incidence. Changing the scattering angle or/and the energy of incident pulse, E_i , differs by $\Delta E = E_i - E_{max}$ from the energy of the central maximum of reflectivity, E_{max} . Fig.7.3d shows the time-

dependent response of the La/C ML for $\Delta E \approx 3 \text{ eV}$. Now, the reflectivity of La/C ML is reduced (to a few percents) but reveals a certain variation of the intensity as a function of N , which is not visible for Ni/C ML. This asymmetry increases for increasing ΔE (not shown). Moreover, for the longer pulses (4 fs and more) one finds an oscillatory behaviour of reflection intensity as a function of N (see later). These features can be explained by the fine structure of the scattering curves as schematically shown in Fig. 7.4.

By changing E_i relative to E_{max} one can excite different spectra: from the continuous to the oscillating features vs N . The ML response to a pulse is an integration of the scattering curve within a certain energy window. If $\Delta E \approx 0$, i.e. $E_i \approx 193,75 \text{ eV}$ as in present example (Fig.7.4c), the scattering phases between different interfaces is always constructive and the response is a smooth function for increasing N (see Fig. 7.4a). If energy shift ΔE is larger then the energy width of the total reflection curve (Fig. 7.4d) the phase shift might be constructive at certain N but destructive for another $N+\Delta N$. This oscillatory behaviour of scattering as a function of N is shown in Fig. 7.4b. Such effect can be used to identify the energy offset of the incident pulse with respect to the central reflection maximum fixed by a certain geometric setup.

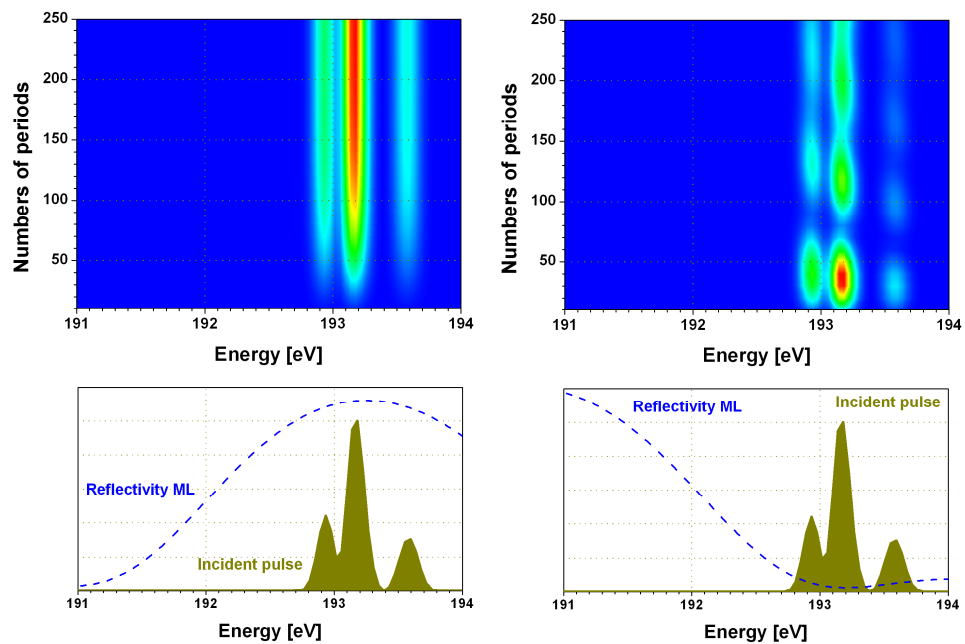


Fig. 7.4 The transition of energy spectra from continuous to oscillatory depending on energy shift ΔE ; (a) without energy shift $\Delta E = 0$, (b) energy shift $\Delta E \approx 3 \text{ eV}$. The energy relation between the incident pulse train and the reflection curve is shown in (c) and (d).

For simulation of an incident FEL pulse, every pulse is composed by several sub-pulses with duration of 2-3fs. Considering the SASE principle each of these sub-pulses (spikes) is statistically spaced to each other and described by Gaussian-functions with varying amplitude.

Additionally the spikes differ in energy within a certain energy window of about 2 eV as expected for FEL radiation. Using this approach one can change the shape of any incident pulse train by the change of spikes parameters such as the amplitude, frequency, location and duration of the Gaussian-shaped sub-pulses as shown in Fig.7.5a. The results of numerical calculation for the both MLs are illustrated in Fig. 7.5b-d. Since the mean energy of the incident pulse train coincides with the energy of maximum reflectivity of the ML the diffraction curves for both ML's show a mirror-like behaviour of the incident pulse structure where each sub-pulse is expanded (see Figs 7.3b and c).

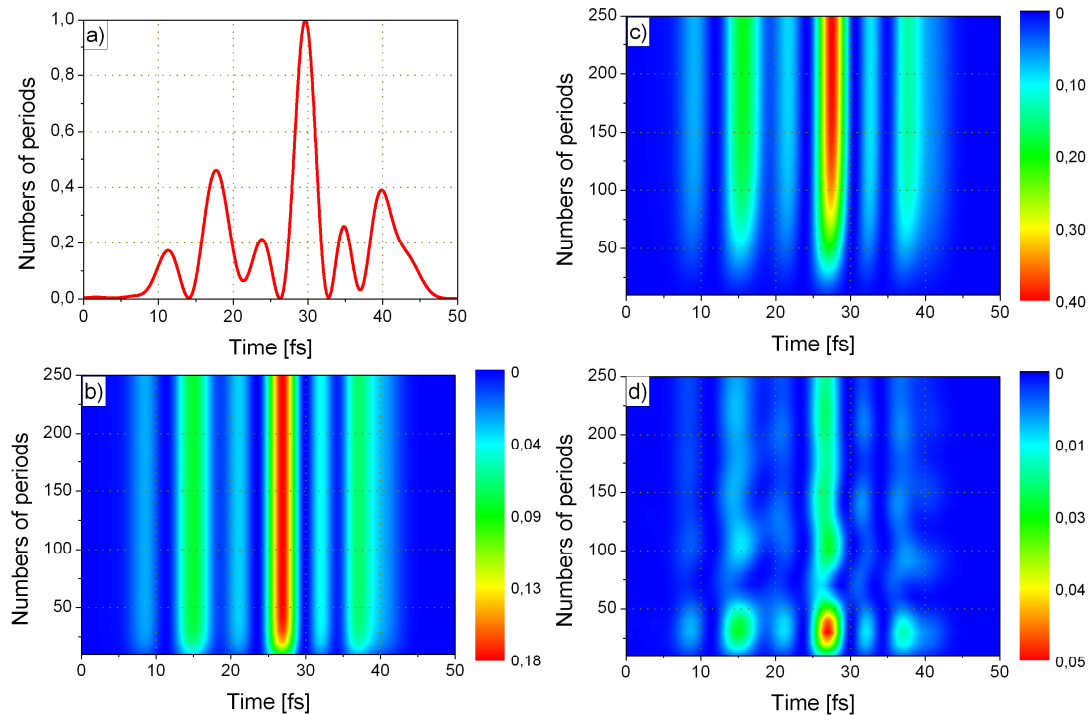


Fig. 7.5 Incident multiple pulse (a) and responses from periodical Ni/C (b) and La/C (c,d) MLs with different numbers of bi-layers. The incident pulses are described the combination of single-Gaussian function with different parameters: frequency, amplitudes, locations and durations in the time range (a). The responses from La/C ML with the energy shift of the incident pulse train of 3 eV (d)

Such behaviour was observed for Ni/C and La/C MLs shown on Fig. 7.5b, c, respectively. The response of La/C ML becomes changed if the mean energy of the pulse train differs by ΔE from the energy of reflection maximum. Fig. 7.5d shows the situation for the energy shift $\Delta E=3$ eV. In contrast to Fig.7.5c, an oscillatory behaviour of the response functions of Fig.7.5d is found in the time and the energy domain. The corresponding pictures in energy domain is shown in Fig. 7.4a,b. For different sub-pulses one finds a different response. One should mention that such redistribution of the response function can be achieved either by

detuning of energy or the incident angle or by changing the structural parameters of the ML. Therefore a careful structural analysis of the ML is mandatory before the FEL experiment

The results of numerical calculation for the Nb/C ML's are shown in Fig. 7.6. Since the mean energy of the incident pulse train coincides with the energy of maximum reflectivity of the ML the diffraction curves show a mirror like behaviour of the incident pulse structure (see Fig. 7.6a) but after reflection each sub-pulse is slightly expanded as shown in Fig. 7.6a. The responses of the ML become changed if the mean energy of the pulse train differs by ΔE from the energy of reflection maximum. To simulate this behaviour we have changed the incident angle from 45.0° to 45.5° which corresponds to the situation of an energy shift of $\Delta E=2.5$ eV (see Fig.7.6b). An oscillatory behaviour of the response functions is found in the time and the energy domain. Moreover, the structure of the response differs for the various sub-pulses.

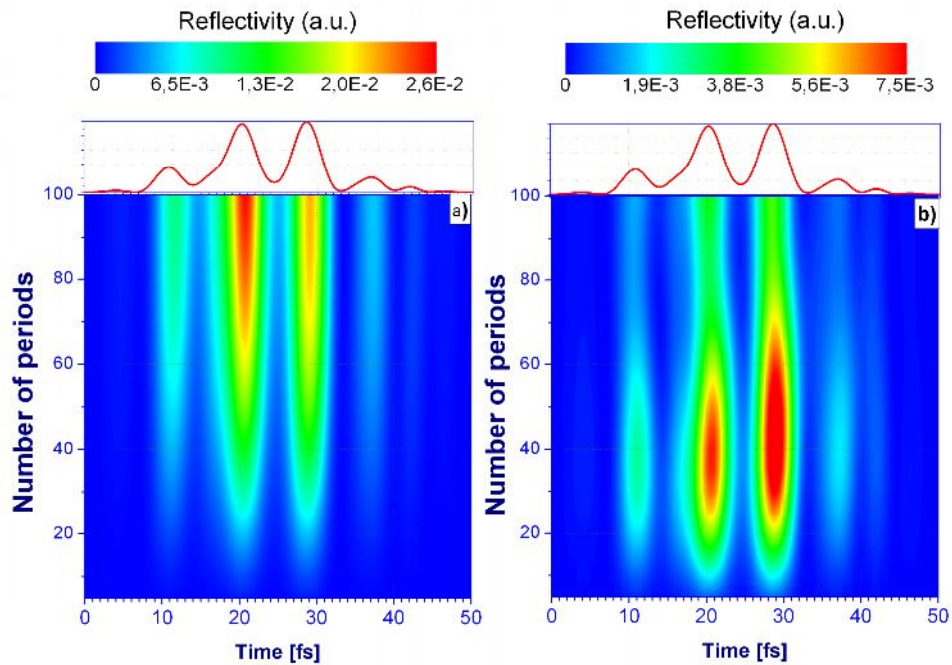


Fig. 7.6 Responses of a periodical Nb/C ML (bottom maps) to an incident pulse train. The incident pulses are described by the combination of single Gaussian functions with different parameters (top profiles). The responses of the ML for $\Delta E=0$ (a) and $\Delta E=2$ eV with respect to the central pulse of the train (b).

Fig.7.7 shows the time-dependent response of the La/B₄C ML for two different cases: (i) Bragg case ($\Delta E \approx 0$ eV) and (ii) ($\Delta E \approx 6$ eV). By changing E_{inc} relative to E_{max} one can excite different response functions varying from continuous to oscillating behaviour where the maximum or minimum appears at different positions N within the ML. If $\Delta E \approx 0$, i.e. $E_{inc} \approx 180$ eV, as shown in Fig. 7.7 (left), the scattering phases between different interfaces are always constructive and the response is a smooth function for increasing N . Otherwise, when ΔE is larger then the energy width of the total reflection curve (see Fig.7.4) the phase shift might be constructive at certain N_i but destructive for another $N_i+\Delta N$. This oscillatory behaviour of

scattering as a function of N is shown in Fig.7.7 (*right*). An oscillatory behaviour of the response functions is found in the time and the energy domain. Moreover, the structure of the response differs for the various sub-pulses.

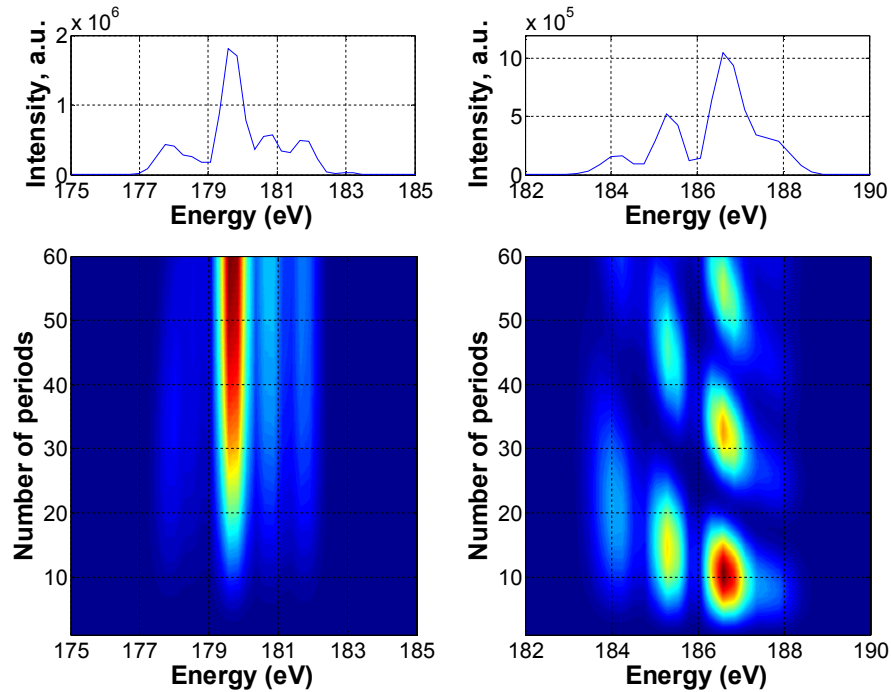


Fig. 7.7 Responses of a periodical La/B₄C ML (maps) to an incident pulse train. The incident pulses are described by the combination of single Gaussian functions with different parameters (profiles). The responses of the ML for $\Delta E=0$ (*left*) and $\Delta E=6$ eV with respect to the central pulse of the train (*right*).

7.3. Space-time transformation

A reasonable scenario of such a scattering experiment consists in the projection of the time-dependent response of the ML to the incident FEL pulse into the spatial coordinate which can be measured by the position-sensitive detector. Due to the pulse structure of the incident X-rays the whole ML response is not detected at the same time. As the incident pulse reaches the first bi-layer interface it provides a strong scattering signal towards the detector. On its passage through the ML the pulse becomes interacting with more and more bi-layers which modifies the intensity and the shape of the scattering signal in a fashion as shown in Fig.7.1. In this sense the vertical coordinate of figures 7.2 – 7.7 (the number of periods) can be transformed into a spatial coordinate seen by the detector.

Due to fs time-structure of irradiation all sub-pulses will coincide on the detector. However, using a scattering geometry where the mean energy of incident pulse is slightly detuned from the maximum of the reflectivity of the first order Bragg reflection the oscillatory behaviour can be maintained even after a overlapping of the all sub-pulses. This is shown in Fig. 7.8 for the case of low-absorbing (La/C) and high-absorbing (Ni/C) MLs. The spatial coordinate, x , reflects the evolution of the scattered signal as function of the increasing number of interfaces,

N , of the ML. The oscillatory behaviour is preserved for the low-absorbing ML and varies as a function of the detuning energy. In contrast, there is no such dependence in high-absorption case. It caused by the fact that the absorption length for radiation at a wavelength 6.4 nm is about 1.7 μm for La/C but only 0,1 μm for Ni/C. At the same time, the geometric length of a 2 fs pulse is 0,6 μm corresponding to $N=134$ periods of the ML.

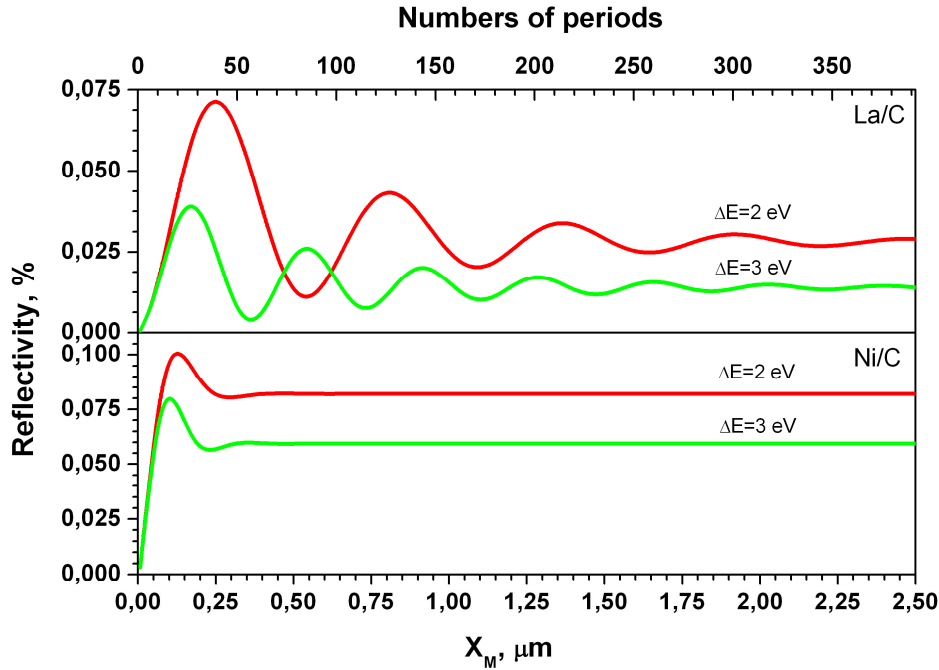


Fig. 7.8 Spatial variation of the reflected intensity for La/C and Ni/C ML as a function of the detuning energy $E_{\text{max}} - \Delta E$. The energy of central maximum reflection E_{max} is 193,75 eV.

Considering a ML with $N = 400$, for example, the interaction length within the ML and subsequently the length of the diffraction spot in the detector plane, x_M , is 2,5 μm . This length can be stretched in space by use of a ML where the surface has a sliced angle α with respect to the multilayer normal. If the incident pulse hits the ML interfaces at a scattering angle $\Theta \approx 45^\circ$ a grazing incident angle with respect to the ML surface of $\Theta - \alpha$ will enlarge the effective size of the reflected beam by $1/\sin(\Theta - \alpha)$. An additional enlargement of x_M can be achieved by oblique setting of the detector with respect to the reflected beam by an angle β of the detector normal with respect to the reflected beam.

To exploit the effect of La/C film the number of ML periods should be very large ($N > 1000$). SMG structures (§4.2) are well suited for this task and give rise to surface gratings in addition to the strong Bragg reflection. Whereas the Bragg reflection probes the bulk scattering of the ML the grating peaks is created by scattering at the surface relief. The latter ones can be used as independent probe for the energy of the sub-pulses without the interaction with the bulk of ML.

For these structures, the energy width of the diffraction pattern increases for increasing the sliced angle α and using grazing incidence geometry. The evolution of diffraction efficiency as a function of α and Θ (both parameters are coupling for resonance case) for La/C with $d=4.7$ nm and thickness ratio of 0.5 is shown in Fig. 7.9.

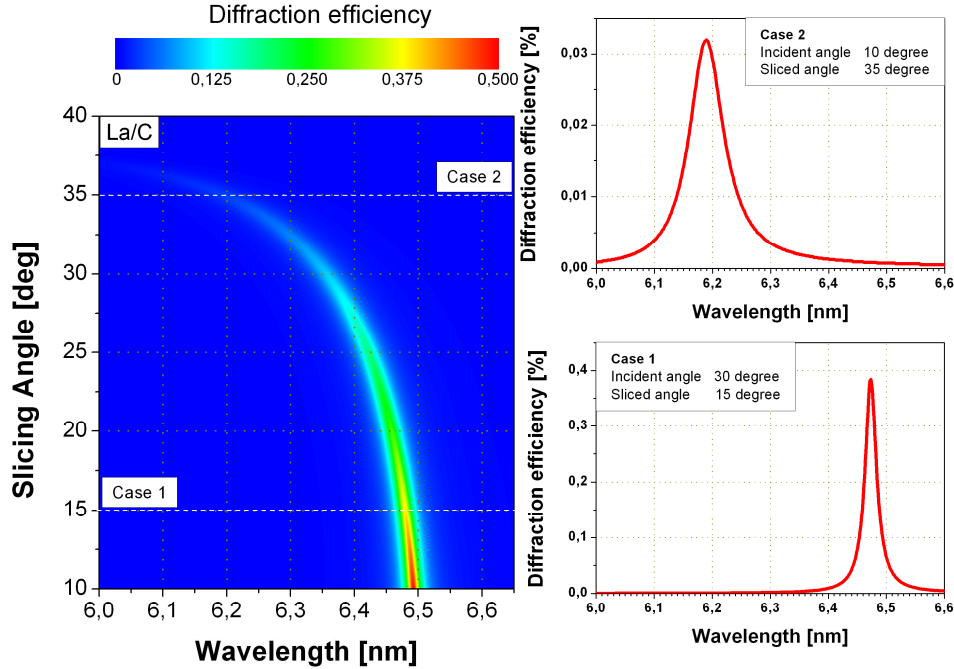


Fig. 7.9 Calculated diffraction efficiency as a function of wavelength, incident and slicing angles. Cases 1 and 2 correspond to relatively small and large slicing angle and reveal different broadening of the diffraction efficiency curves.

As shown on right hand of Fig.7.9 the FWHM of the diffraction maximum increases by a factor $\sqrt{\sin(\theta + \alpha)/\sin(\theta - \alpha)}$ increasing the sliced angle Θ and the energy position of scattering maximum is shifted to the lower wavelength accompanied by a reduction of total scattering power as known from x-ray dynamical theory. For comparison shown at $\Theta = 0$ the FWHM is increased by a factor of 1.32 and 2.38 for the cases 1 and 2 in Fig.7.9, respectively.

For ML period $d = 4.7$ nm and $\alpha = 35^\circ$ (and grazing angle is 10°) (case 2 on Fig. 7.9) the effective grating spacing $D = d/\sin\alpha = 8.2$ nm which gives the 1st order grating peak at $\Theta_m = 10^\circ$. However, due to the finite length of the incident sub-pulse (duration is 50 fs) the number of illuminated grating periods is large (here about 1600) resulting in a narrow grating peak. Therefore measurement of angular position and angular width of the grating peak is an independent and precise probe of the energy and the energy spread of the incident pulse.

7.4. Reconstruction of fs-pulses from spatially resolved ML response

Due to the SASE principle, the structure of a FEL pulse cannot be exactly predicted. Moreover, every pulse differs from each other. Therefore, there is a need for direct measurement of each

pulse. Exploiting the time-space-transformation of the incident pulse and using a scattering geometry where the mean energy of incident pulse train is slightly detuned from the energy of maximum reflectivity at 1st order ML Bragg peak, the spatially resolved scattering signal becomes a measure of the energy and pulse structure of the incident pulse train.

As shown in Figs.7.2-7.7 the particular response of a sub-pulse depends on its detuning energy with respect to the energy of maximum reflectivity of the ML. This peculiarity can be used as a probe of the pulse structure in the VUV-FEL experiments. Considering the detection scheme shown in Fig.7.1, the ordinate of Figs 7.2-7.7 (number of periods, N) becomes a the spatial coordinate, X , and the abscissa of Figs 7.2-7.7 is the time-integrated intensity after the pulse interaction. Moreover, for certain ΔE this time-integrated signal maintains the oscillatory behaviour as in the time resolved mode.

Fig.7.10 shows the scenario of these subsequent test pulses and the respective spatially resolved signal at the detector after reflection from the low-absorption ML as a function of detuning energy ΔE . The ML responses for both sets of test pulses with different detuning ΔE are clearly different. The visibility of oscillation is the best close to the energy of 1st order diffraction maximum of ML where the contrast is high (Fig. 7.10, *top curves*). This peculiarity seems to be essential for the pulse reconstruction and the possible detector images of the pulses 1 and 2 are shown on the Fig. 7.1.

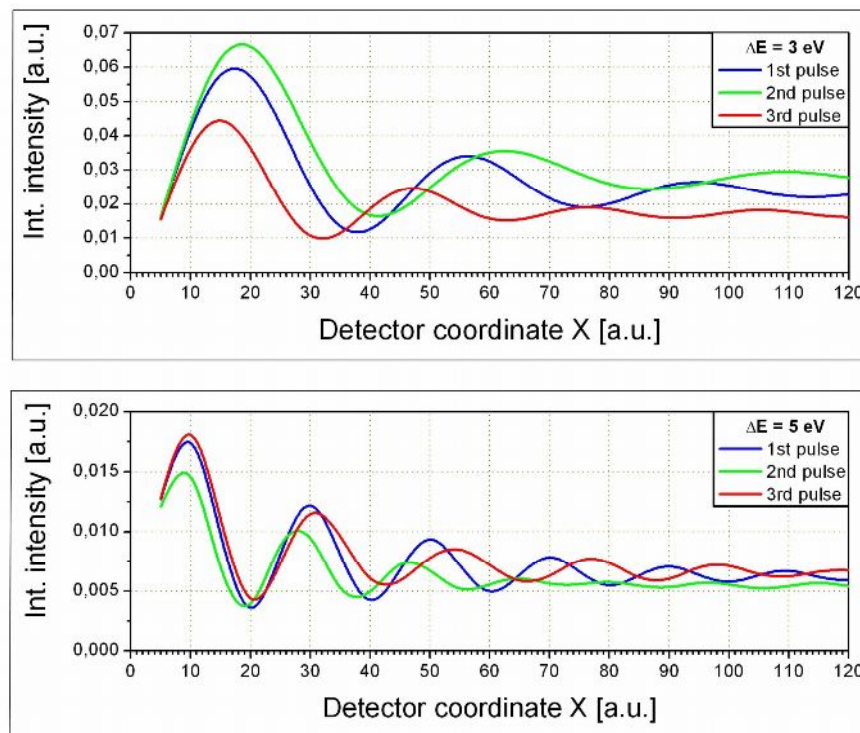


Fig. 7.10 The response function at the detector to different incident pulse trains after time integration of the time-resolved reflectivity pattern recorded at detuning energy of $\Delta E = 3$ eV (*top*) and 5 eV (*bottom*) with respect to E_{\max} .

A certain ΔE one can be define by particular setting of the incident angle, Θ , being different to the angle Θ_{max} which corresponds to the 1st order reflection maximum. Considering this, an incident pulse with an unknown energy distribution of the intensity interacts with the low-absorbing ML. As a result, we obtain a intensity distribution as a function of two parameters: the incidence angle Θ and detector coordinate X , where the last one is directly proportional to the numbers of periods, N . Subsequently, the function $g(N, \Theta)$ is the integrated intensity of the FEL pulse after reflection from the ML and can be measured by the detector. This function depends on the reflection properties of the ML, $R(N, \Theta, E)$, which, in turn, is a function of N , incident angle Θ and the energy of the incident radiation, E . Function $R(N, \Theta, E)$ is connected with the unknown energy distribution of the incident pulse $f(E)$ via *the Fredholm integral equations of the first kind*:

$$\int R(N, \Theta, E) \cdot f(E) dE = g(N, \Theta) \quad (7.4)$$

This integral equation can be solved under the assumption that the *kernel* is a stepwise smooth function and has positive values in the range $[E_{min}=E-\Delta E; E_{max}=E+\Delta E]$, where ΔE is small (0.5...1.0% bandwidth (FWHM) of the incident pulses energy). The *Fredholm integral equations of the first kind* play an important role in many problems like antenna design, astrometry, computer tomography, image restoration. Methods for solution of such kind of equations are described by Baker *et al.*[133] and Tikhonov.*et al* [134]. Eq. 7.4 can be transformed into a matrix problem simplified by $A \cdot x = b$. Therefore Fredholm integral equations can be expressed by

$$\int R(N, \Theta, E) \cdot f(E) dE \quad g(N, \Theta) \cong \sum_j w_j \cdot R(N_i, \Theta_{fix}, E_j), \quad (7.4')$$

where w_j is a weight factor of each component $f(E_j)$.

Eq. (7.4') in the matrix form can be numerically solved using the reliable functions. To demonstrate the procedure we have used function $g(N, \Theta)$ as a vector, consisting of 31 discrete values, such as the CCD pixel values shown in Fig. 7.11a. The ML consists of 91 periods, which disredized with step, $\Delta N=3$. To test the reconstruction procedure we calculated the reflectivity of the ML within a band pass of $\Delta E = \pm 1$ eV and at $\Theta = 41^\circ$ for an initial pulse shown as a dotted line in Fig.7.11b. The test pulse consists of five spikes with the different energy widths. Reflectivity $R(N, \Theta, E)$ is calculated in discrete steps of $dE=0.004$ eV as a function of the energy and the numbers of periods for a fixed incident angle. Finally, the reconstructed pulse train is shown as a smooth curve in Fig.7.11b.

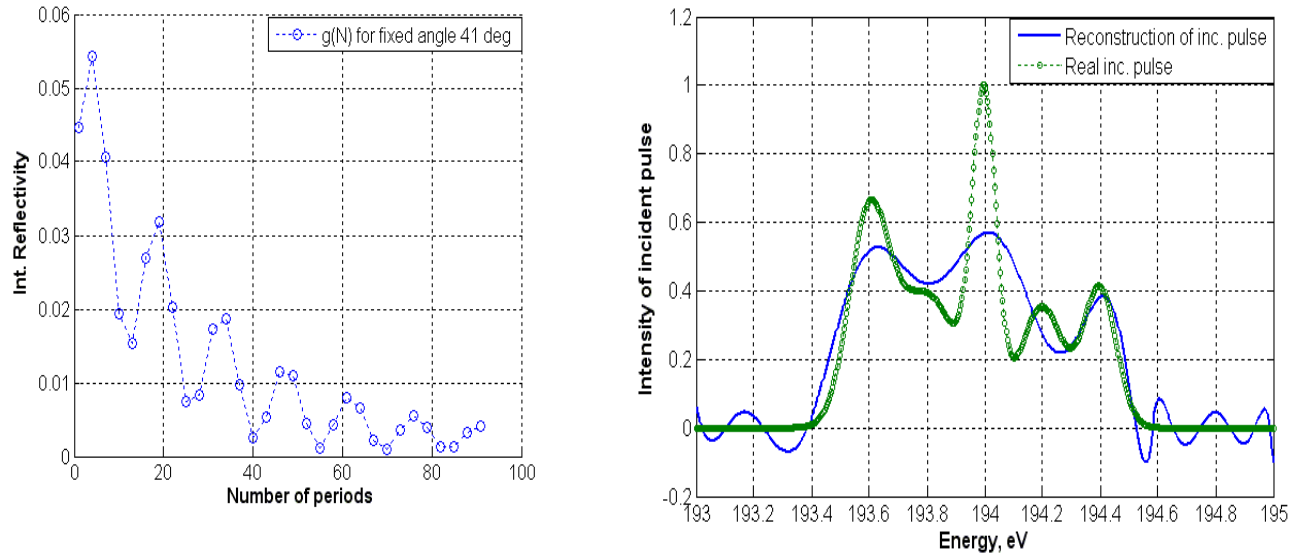


Fig. 7.11 Detector response function $g(N, \Theta)$ (left) consisting of 31 points; the test pulse (dotted line, right) and reconstruction (smooth curve, right) using the detector response function $g(N, \Theta)$.

From the Fig.7.11b we can conclude that the reconstruction of sub-peaks with a narrow energy distribution is more difficult than for smooth ones. The resolution limit of sub-peaks is about 0.1 eV and does not strongly depend on the numbers of the detector pixels (minimal amount is about few tens) and the numbers of ML periods (more than hundred). In addition, there is only a small improvement of resolution increasing the contrast of the reflectivity function.

The quality of reconstruction at different incidence angles Θ , corresponding to different energy offsets ΔE , are shown in Fig 7.12. Also we added a detector noise of 1% and a detector threshold of (10^{-3}) . In this case, the pulse reconstruction approach is effective in a range of detuning angles of few degrees, respectively $\Delta E = 0 \dots 10 \text{ eV}$. In addition, it depends on detector characteristics (accuracy of detection and dynamical range of detector).

Summarize, it was found that at least 30...50 points (CCD pixels) are necessary at least. However, the energy resolution of the method is limited to about 0.1 eV and narrow ($\leq 0.1 \text{ eV}$) and broader peaks can not be reconstructed simultaneously due to mathematical reasons. Subsequently the quality of reconstruction cannot be increased by a higher number of CCD pixels in data recording. Considering the penetration depth of the X-ray beam into the ML material the lateral width of the detector signal is $X = T / \sin \Theta = 2.5 \mu\text{m}$ which is less than the size of a CCD pixel. In work [131] authors have shown that this length can effectively be increased by using a sliced ML structures. If the slicing angle is α , and the incident pulse hits the ML interfaces at a grazing incident angle $\Theta - \alpha$ the effective lateral extension of the reflected beam will be enlarged by a factor $1 / \sin(\Theta - \alpha)$. An additional enlargement of X can be achieved by oblique setting of the detector with respect to the reflected beam by an angle β of the detector

normal with respect to the reflected beam. For Nb/C ML and using $\Theta - \alpha \approx 2^\circ$ and $\beta \approx 5^\circ$ X becomes enlarged to about $800 \mu\text{m}$ which gives more than 50 points at a CCD with pixel size of $25 \mu\text{m}$. As shown in [131] the intensity decreases and the energy of first order reflection peak increases for increasing the α . This variation will not change the general applicability of our approach.

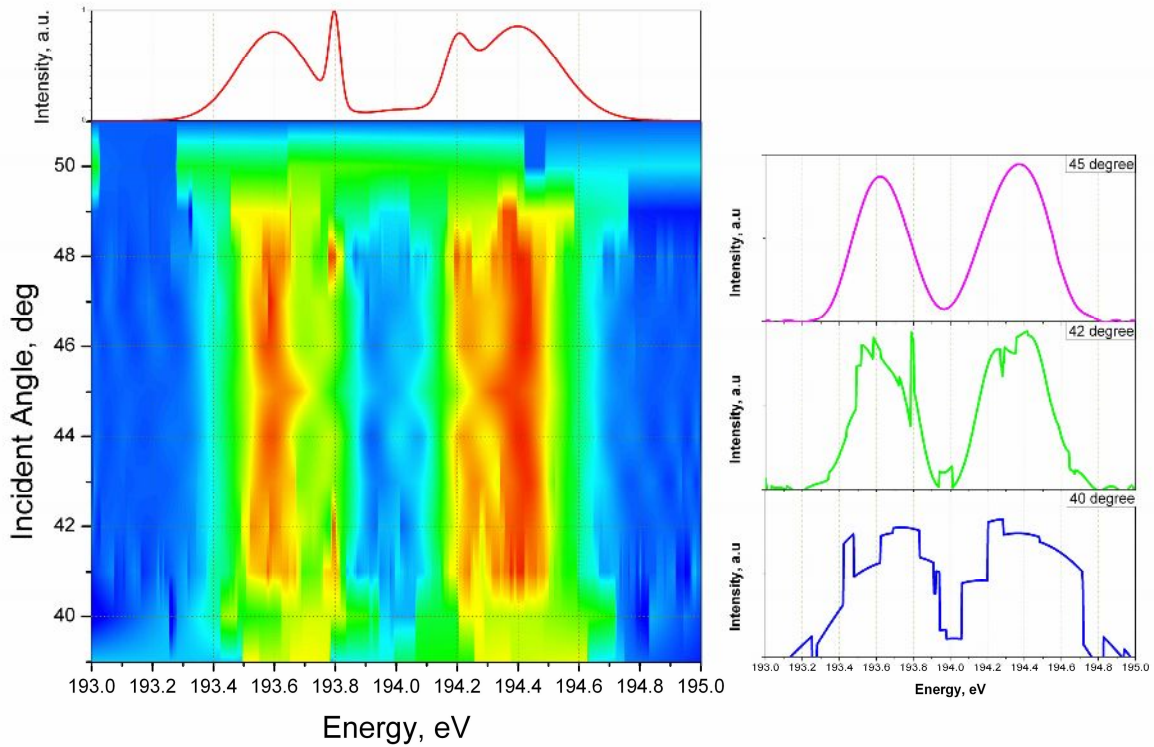


Fig. 7.12 Pulse reconstruction (map) of incident signal (*top left profile*) as a function of different incident angles Θ . The selected line scans (*top, middle, bottom*) correspond to $\Theta = 45^\circ, 42^\circ, 40^\circ$. Maximum reflectivity appears at $\Theta = 45^\circ$.

7.5. Processes of the ionization: influence of high intensity

Considering the available energy range of FLASH, the K-electron excitation processes and Auger recombination are expected for low-Z elements such as boron and carbon atoms. Properties of Me/B_4C MLs in this energy range for continuous VUV radiation have been described in Chapter 6. Boron K-edge is chosen due to its high sensitivity to the phase of the virtual transition state interfering with the phase of the incident pulse. Close to the B K-edge the real part of anomalous dispersion shows a sign reversal above and below the edge, and we expect the major changes in reflectivity, depending on the intensity of the incident FEL pulses.

Using the time- space conversation of the experimental setup (Fig. 7.1), it will be able to study under which experimental conditions major deviation from the our experimental data for continuous synchrotron radiation in this energy range take place, and which corrections are necessary to describe the processes. To describe the role of the ionization of atoms inside the

ML, we can use the optical properties of ionic boron. These data can be applied for calculating the scattering properties of MLs near K-edge by high-intensity FEL radiation.

7.5.1 Calculation of Anomalous Scattering for Ions and Atoms

Elastic scattering of photons by atoms, ions or molecules is important in many fields such as crystallography, plasma physics and astrophysics. In the range of high photon energy (i.e., well above the K-shell threshold energy of the atom or ion), form factor (FF) or modified form factor (MFF) approximations are widely used and at least moderately successful, in estimating the scattering cross sections. For neutral atoms the anomalous scattering factors have been calculated over a wide range of photon energy for most elements, as in the work by Cromer and Liberman [135] and Henke et al. [118]. But for ions systematic studies are not yet available. On the other side, Hartree-Fock (HF) wave functions for atoms and atomic ions may be computed numerically by standard methods [136]. Roothaan-Hartree-Fock (RHF) wave functions are algebraic approximations to HF wave functions in which the Roothaan procedure [137-139] is used to expand the radial orbitals in a basis set of, say, Slater-type functions (STF's). RHF wave functions are in great demand because they are more convenient than numerical HF ones. RHF wave functions for the atoms from He to Xe were tabulated by Clementi & Roetti [140-141] and Bunge et al. [142], and for heavy atoms by Delavega and Miguel [143].

The form factor $f(q)$ for a spherically symmetric charge number density $\rho(r)$ and a momentum transfer $\hbar q$ is defined as

$$f(q) = 4\pi \int_0^{\infty} \rho(r) r^2 \text{sinc}(qr) dr. \quad (7.5)$$

Because the atom are describing in a single-electron model, the charge distribution $p(r)$ may be decompose and also the form factor $f(q)$ into a sum of terms corresponding either to individual electrons or to a particular sub-shell (all electrons of fixed principal quantum number n and total angular momentum quantum number j) or a particular shell (all electrons of fixed n) (*Appendix D*). The anomalous scattering factors g' and g'' can be calculated, utilizing a dispersion relation and the optical theorem, as

$$\begin{aligned} g'(E) &= f'(E) - f'(\infty) = \frac{2}{\pi} P \int_0^{\infty} \frac{E' g''(E')}{E'^2 - E^2} dE' \\ g''(E) &= f''(E) - \left(\frac{\alpha}{4\pi} \right) \left(\frac{E}{mc^2} \right) \left(\frac{\sigma_{PE}(E) - \sigma_{BPP}(E)}{r_0^2} \right) - \\ &\quad - \frac{\pi}{2} \sum_{m,n} E_{mn} f_{mn} \delta(E - E_{nm}) \end{aligned} \quad (7.6)$$

Here σ_{PE} is the sum of sub-shell photo effect cross sections; f_{mn} is the oscillator strength for the transition from the occupied bound state, m to unoccupied state n and E_{mn} the difference between the binding energies of the two bound states m and n . The quantity σ_{BPP} is the sum of sub-shell bound pair production cross sections, with the creation of an electron-positron pair in an ion with a sub-shell vacancy with the electron filling that vacancy; it must be included in order to make the principal value integration converge at high energies.

In work [144] Zhou *et al.* proposed the simple computational schemes to calculate angle-independent anomalous scattering factors for ions in the X-ray regime, utilizing sub-shell photo effect cross sections of the neutral atom and dispersion integral. Eq. 7.6 can be re-written as:

$$\begin{cases} g'' = \sum_m g_m''(E) \\ g' = \sum_m g_m'(E) \end{cases} \Rightarrow \begin{cases} g''(E) \\ g'(E) \end{cases} = g_0'(E) + \sum_m \Delta g_m'(E) \quad (7.6a)$$

for inner shells:

$$\Delta g_m'(E) \approx \left(\frac{a}{2\pi^2}\right) \left(\frac{1}{mc^2}\right) \left(\frac{1}{r_0^2}\right) \sigma_{PE}^m(E_0^m) \times \left\{ \Delta E_m + \frac{E}{2} \ln \left[\frac{[(E_0^m + \Delta E_m)^2 - E^2] E_0^{m2}}{(E_0^m + \Delta E_m)^2 (E_0^{m2} - E^2)} \right] \right\} \quad (7.6b)$$

for outer and intermediate shells:

$$\Delta g_m'(E) \approx \left(\frac{a}{2\pi^2}\right) \left(\frac{1}{mc^2}\right) \left(\frac{1}{r_0^2}\right) \left(\frac{E_0^{m3}}{2E^2}\right) \sigma_{PE}^m(E_0^m) \times \ln \left[\frac{[(E_0^m + \Delta E_m)^2 - E^2] E_0^{m2}}{(E_0^m + \Delta E_m)^2 (E_0^{m2} - E^2)} \right] \quad (7.6c)$$

Total cross-section for atomic (BI) and ionic boron (BII and BIII) ground states are shown on Fig. 7.13. In process of ionization, the K-edge will be shift to higher energy from 188eV to 235eV. For light elements, the shift of K-shell can be described next approximation [144]:

$$\Delta E_K = E_i^K - E_0^K = \left(\frac{Z_i}{Z}\right)^2 (E_C^K - E_0^K) \quad (7.7)$$

where E_C^K is Coulombic binding energy and Z_i is the degree of ionization.

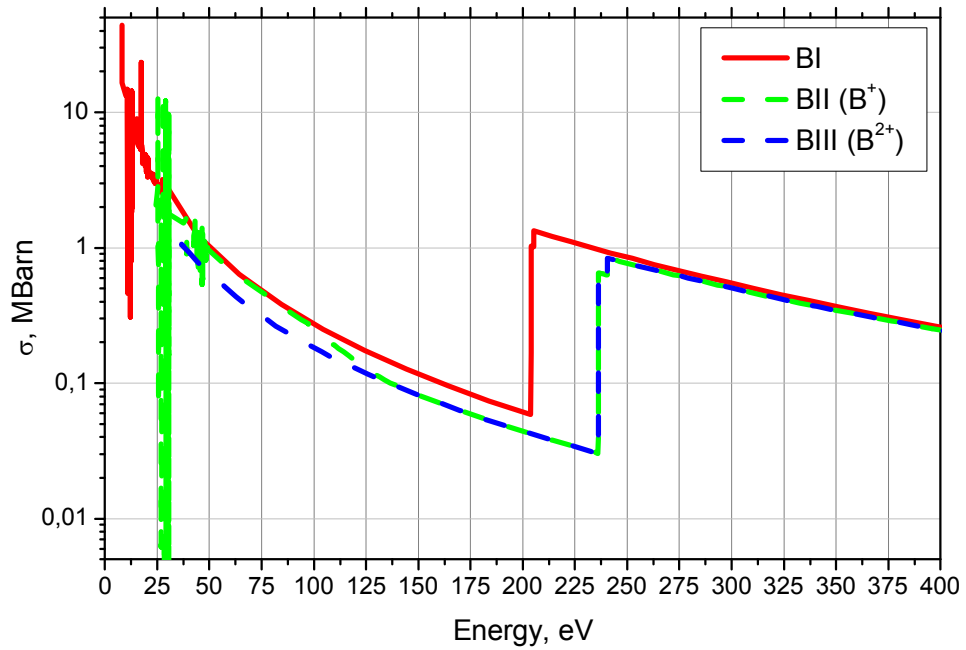


Fig. 7.13 Photoionization cross sections of atomic (BI) and ionic boron (BII and BIII) in ground states 2P_0 , 1S and 2S , respectively as a function of photon energy (from database “TIPTOPbase” <http://cdsweb.u-strasbg.fr/topbase>).

These data can be use in the simulation of the processes of interaction fs X-ray pulses with the multilayer including the process of ionization. On Fig. 7.14 are shown the calculated optical properties of boron carbide, containing neutral atom or ion of boron.

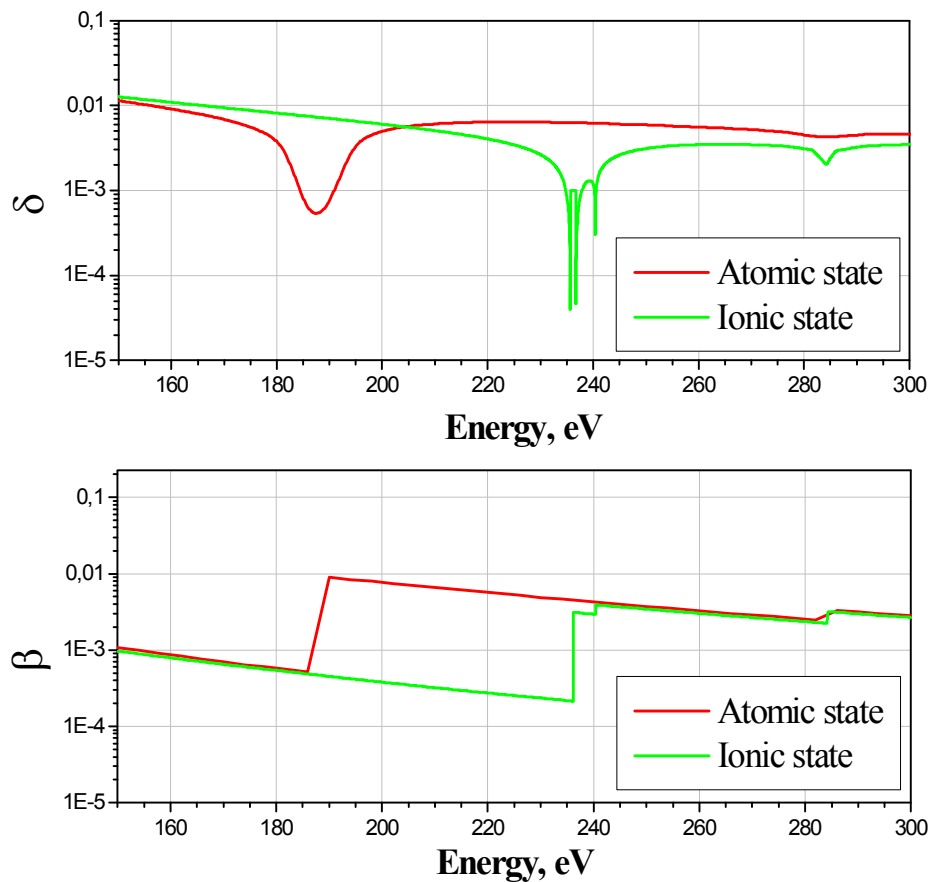


Fig. 7.14 Refractive index $n=1-\delta+i\beta$ of B_4C with atom (red line) and ion of boron (green line)

7.5.2. Temporal evolution of the optical properties of boron carbide

The scattering behaviour of the matter will change without any change of the crystal lattice during the interaction FEL pulse with matter. Figure 7.15 shows the time evolution of the opacity as a function of B₄C material depth for the incident energy of 210eV and a fluence of 200 J/cm², and Gaussian pulse with duration 15fs, which calculated Bergh *et al* in work [51] using *non-local thermodynamic equilibrium* (NLTE) simulations of the heating of solids by femtosecond VUV and X-ray lasers at different fluencies. This material contains from both low-Z elements, and in process of the interaction their electron structure will be strong changed.

At this energy the photons are energetic enough to ionize the boron K shell directly, but not the carbon K shell. The incident photons interact mainly with the core electrons in boron, with photoionizations followed by fast impact ionization of the valence electrons of both boron and carbon. The free electrons are heated to a temperature of about 40eV, which is too low to significantly impact excitation or ionization of the K-shell electrons. Also, it was noted in work of Bergh *et al* [51], that in the resonant region of the absorption spectrum, there will be line contributions from bound-bound transitions in the plasma, further complicating the absorption mechanisms, as well as a considerable broadening of the lines at solids.

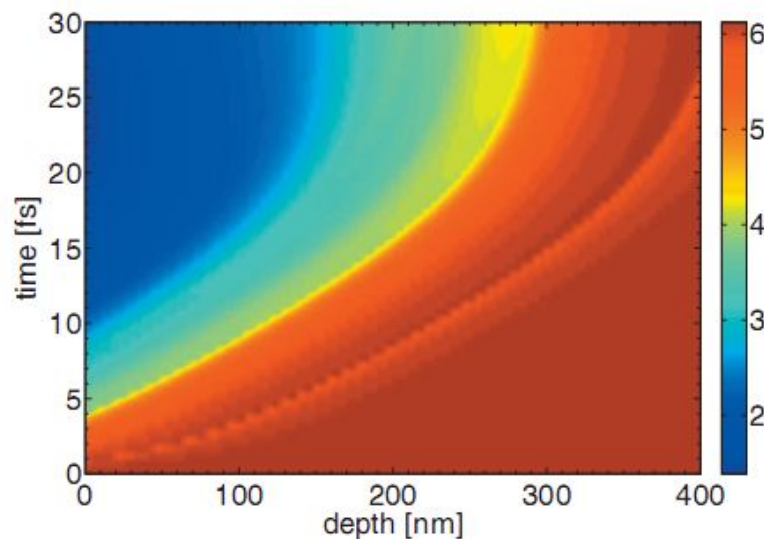


Fig. 7.15 Temporal evolution of the opacity as a function of material depth for B₄C [51]. The pulse has a wavelength of 5.9 nm, a fluence of 200 J/cm², and a pulse length of 15fs. The opacity decreases by almost a factor of 4 due to the weak inverse bremsstrahlung.

7.6. Possible experimental setup of the experiment at FLASH

Preliminary simulations considering form factors of boron atoms and ions have shown that due to ionization pronounced changes in the reflectivity curve are expected. Comparing neutral and ionic boron both energy position and peak shape of 1st order Bragg peak of ML is changed. Depending on degree of ionization the position of the B K-edge is shifting from ~188eV (for atomic state) to ~235eV (for ionic state) (see Figs.7.13 and 7.14). Boron edge is chosen due to its

high sensitivity to the phase of the virtual transition state interfering with the phase of the incident pulse. Close to the B K-edge the real part of anomalous dispersion shows a sign reversal below and above the edge. The present theory of anomalous dispersion is restricted to “free” atoms and low excitation, it can be expect major changes in reflectivity as a function of incident intensity, which can be effectively probed measuring the entire Bragg reflection curve.

In order to measure the reflectivity curve over a wide angular range using “single shot” exposure the sample will be *cylindrically bended multilayer* and illuminated through a set of parallel arranged guiding pinholes acting as a *transmission grating* (Fig. 7.16). The reflection from the grating is used to determine the energy of the respective FEL pulse with high resolution CCD (*Detector 1*). The diffracted beams will be absorbed by a second grating with same parameters set behind the first one. Selected from one and the same incident pulse with intensity below the threshold of damage each partial beam passed through the pinhole grating will hit the multilayer under a different angle of incidence and subsequently reflect at different angular positions. Therefore, the broadening of reflection curve will occur with expanded range of different reflected angles. The latter ones allow a spatial separation of each of individual scattering position on a pnCCD (*Detector 2*) which allows both spatial and energy resolution at same time including the fluorescence radiation in background. Using ML with bending radius of around ten of centimetres, the spatial separation of neighboured beam will fit with the pixel size of pnCCD (256×256 sensitive pixels with $75 \mu\text{m} \times 75 \mu\text{m}$ pixel size)

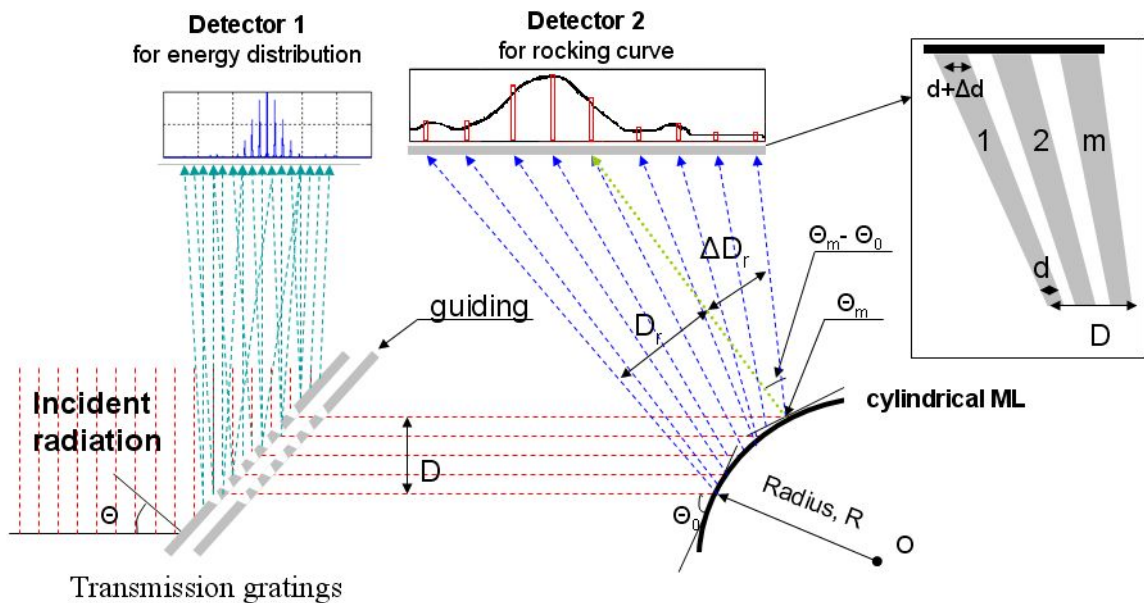


Fig.7.16 Experimental scheme to measure the ML reflectivity using single shot experiments. Second pinhole grating will be use optionally as guiding grating to cut scattering figures from individual pinholes.

In order to study the effect of excitation and recombination at the ML, the incident pulse energy will be tuned close to the B K-edge. The average angle of incidence, Θ , of the FEL beam

with respect to the ML normal is fixed in such a way that a certain angular range, $\Delta\Theta$, is simultaneously excited by several partial beams. The average angle Θ can easily be changed to cover different ranges within the reflection curve. Preliminary simulations considering form factors of boron atoms and ions, have shown that the maximum changes in reflectivity curve due to ionization are expected, if Θ is close to the 1st order multilayer Bragg peak due to the shift of B K-edge from $\sim 188\text{eV}$ (for atomic state) to $\sim 235\text{eV}$ (for ionic state) (see Fig.7.17). The resolution of obtained peaks can be tuned by using ML with different numbers of periods.

Using a mean incidence angle of 32° the angular separation between reflected peaks from initial B and almost ionized B^+ is more than 1° (Fig. 7.17). Higher shifts are expected for higher ionization states. The effect found for ML's at ground state after chemical modifications is expected to appear in similar manner after FEL induced ionization.

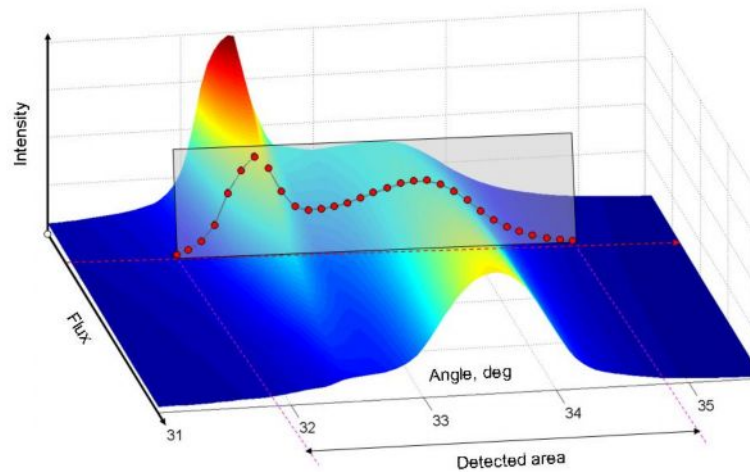


Fig. 7.17 The integrated intensities per single pulse for the multilayer with different degree of ionization vs the flux and grazing angle of incident pulse (*on set* it is demonstrated a presumptive result from detector).

Due to depth dependent absorption excitation processes will be most effective close to the surface but will decay in probability for deeper region within the ML. Using the time- space conversation of the experimental setup, one will be able to measure major deviations from experimental conditions compared to continuous synchrotron radiation in this energy range, and which corrections are necessary to describe the processes under FEL conditions. Following proposed experimental setup we will be able to measure the whole reflection curve close to the 1st order ML Bragg peak and to determine the optical properties of boron and carbon material under condition of high intense fs- pulses of FLASH at energies close to K-edges.

Summary

The VUV FEL FLASH operates in soft X-ray range and produces ultra short pulses with high intensity. The radiation from FEL has spontaneous nature and can be described the Rice's theory. In case of pulse generation in the SASE regime the FEL will produce a pulse train from ten to few hundreds fs duration at soft (e.g., FLASH) to hard X-ray range (European XFEL) which is nearly fully coherent in the transverse direction. The transversely fully coherent beam with pulse duration of a few femtoseconds will open new experiments in solid state physics which can not be studied with present radiation sources.

Till now the interaction of intense, ultra short X-ray pulses with solids is not very well understood. In particular there is no rigorous treatment of the response of crystalline matter to highly intense fs- X-ray pulses. From first experiments with the FLASH one knows that direct illumination of a crystalline solid with an FEL pulse results in complete destruction of the material. On the other hand there are interesting scientific questions in solid state physics which can be elucidated by fs-diffraction only, for example, the investigation of the time-structure of electron-phonon interaction in solids.

The influence of electronic excitation to the X-ray scattering process is very important. In particular, one has to know an intensity threshold which does not change the optical properties of the matter and can be tolerated by the matter without major damage or fluence dependent absorption. In this work the scattering of X-ray radiation in soft X-ray range from MLs based on B₄C was analysed and the possible experimental scheme was proposed to study the interaction of soft X-ray FEL pulses with a periodical multilayers. The boron-containing MLs made for the use in the wavelength range near K-edge of boron (~188eV) are of great interest for X-ray fluorescence analysis of boron doped semiconductors for plasma diagnostics, astronomy and lithography. Moreover, these structures composed by metal and low Z elements like B₄C or carbon are wide-used as optical elements in soft X-ray spectral range. This also holds for application at FELs like FLASH.

For a ML the effective penetration depth corresponds to a certain number of layers probed by the incident radiation. In this thesis was shown that the shape of the reflection curve will change during the time of propagation of the pulse through the ML structure due to the interaction of the beam with an increasing number of periods. The study of the time dependent response of the ML to the X-ray pulse can provide insights into the process of interaction of highly intense FEL radiation with matter. There are various approaches as kinematic and dynamical theory of X-ray diffraction, describing the scattering properties of MLs with a continuous synchrotron radiation. These theories have been extended to describe of the

interaction of short optical pulses with matter. However, these approaches can not be applied to describe the interaction of short intense X-ray FEL pulse with multilayer, because they are based on the consideration of constant optical properties during the interaction of X-ray photons with the solids.

It is expected that during the propagation through the ML the FEL pulse excites many electrons from the ground state of atom into a vacuum and excited states. At the same time, the several recombination processes take place, such as Auger recombination. All these interaction processes cannot be described by a time-constant atomic form factor. Therefore, the theory, which considers the time evolution of electron population during the interaction of the FEL pulse with matters, is required. The experiments at FEL can help to reformulate the X-ray scattering theory, and give additional information to propose various approaches in the description of time-dependent optical properties.

To test the influence of electron excitation on the optical properties of boron carbide, the dispersion and absorption coefficient of B₄C were measured near boron K-edge by energy-resolved photon-in-photon-out method in the soft X-ray range probing a Bragg reflection from periodical multilayers. The measured data clearly show that the variation of the fine structure of the K-absorption edges due to the chemical nature of the absorber element. As in the NEXAFS a higher ionic charge of the absorber atom results in a shift of the absorption edge towards higher energies. In terms of the kinematic approximation δ and β can be simply derived independently from each other using an energy-resolved photon-in-photon-out method. For thicker samples multiple scattering effects ML become important requiring a full dynamical theory. The samples show similar key features as K _{α} line (~183eV), the K-edge of atomic boron (~188eV), π^* - (~194 eV) and σ^* -transitions (198...210eV) of the boron carbide. The obtained differences between the samples we explain by the different chemical environment of boron. Also we obtain additional information from similar measurements taken near the carbon and nitrogen K-edges.

The knowledge obtained from experiments with continuous radiation was used to design the respective experiments with pulse from the FEL. The whole information about the scattering process has to be obtained by single short (single pulse) experiments. In my thesis, it is proposed that the geometrical setup, where the incident pulse arrives from the FEL under the angle close to the 1st order ML Bragg peak, provides the most valuable information. Using MLs composed by two different low-absorbing materials for this energy range, the evolution of the multilayer response can be analyzed as a function of the penetration depth of the incident pulse due to the finite length of a pulse. The evolution of ML reflectivity as a function of the number of interfaces becomes visible, if the mean energy of the incident pulse differs by a small amount, ΔE , from the energy of maximum reflectivity at the 1st order Bragg peak. Using ML as a

monochromator for the following experiment such detuned scattering geometry can be an option to tailor the reflection intensity. Here, the spatial extension of the reflected pulse at the detector is the direct measure of the absorption length within the sample.

In this scheme, any effect of a modified interaction, due to nonlinear absorption or electronic excitation, which would result in a reduction of the effective absorption length, becomes directly measurable by such a scattering experiment. Various phenomena of excitation may play an important role in process of the interaction of FEL radiation with the materials and may change the reflectivity and its time structure eventually. Preliminary simulation considering form factors of neutral and ionized boron showed that due to ionization, pronounced changes in the reflectivity curve are expected. Comparing neutral and ionic boron, both energy position and peak shape of 1st order Bragg peak of ML are changed.

In summary, the proposed scheme can be the powerful tool to study the various processes within the electronic sub-system of the FEL pulse interaction with matter. This type of investigations gives a deep understanding of the nature of the electronic excitation and the recombination at the femtosecond scale.

Appendix A

Kramers-Kronig relations

The *Kramers–Kronig relations* are mathematical properties, connecting the real and imaginary parts of any complex function which is analytic in the upper half plane. These relations are often used to relate the real and imaginary parts of response functions in physical systems because causality implies the analyticity condition is satisfied, and conversely, analyticity implies causality of the corresponding physical system. The relation is named in honour of Ralph Kronig and Hendrik Anthony Kramers.

For a complex function $\chi(\omega) = \chi_1(\omega) + i\chi_2(\omega)$ of the complex variable ω , analytic in the upper half plane of ω and which vanishes faster than $1/|\omega|$ as $|\omega| \rightarrow \infty$, the Kramers–Kronig relations are given by

$$\chi_1(\omega) = \frac{1}{\pi} \mathcal{P} \int_{-\infty}^{\infty} \frac{\chi_2(\omega')}{\omega' - \omega} d\omega'$$

and

$$\chi_2(\omega) = -\frac{1}{\pi} \mathcal{P} \int_{-\infty}^{\infty} \frac{\chi_1(\omega')}{\omega' - \omega} d\omega',$$

where \mathcal{P} denotes the Cauchy principal value. We see that the real and imaginary parts of such a function are not independent, so that the full function can be reconstructed given just one of its parts.

An important example of the application of Kramers - Kronig relations in physics is an expression of the dispersion relations in classical electrodynamics. In this case, $\varepsilon(\omega) = \varepsilon'(\omega) + i\varepsilon''(\omega)$ - relative dielectric constant, ω - frequency.

$$\varepsilon'(\omega) - 1 = \frac{1}{\pi} \mathcal{P} \int_{-\infty}^{\infty} \frac{\varepsilon''(x)}{x - \omega} dx$$

and

$$\varepsilon''(\omega) = -\frac{1}{\pi} \mathcal{P} \int_{-\infty}^{\infty} \frac{\varepsilon'(x) - 1}{x - \omega} dx.$$

The real and imaginary parts of permittivity, respectively, determine the refractive indices and absorption of the medium, so these figures are not independent of each other.

Appendix B

Fourier transforms

In mathematics, *the Fourier transform* (often abbreviated FT) is an operation that transforms one complex-valued function of a real variable into another. In such applications as signal processing, the domain of the original function is typically time and is accordingly called *the time domain*. That of the new function is frequency, and so the Fourier transform is often called *the frequency domain* representation of the original function. It describes which frequencies are present in the original function.

There are several common conventions for defining the Fourier transform of an integrable function $f: \mathbb{R} \rightarrow \mathbb{C}$:

$$\hat{f}(\xi) = \int_{-\infty}^{+\infty} f(x) \exp(-2\pi i x \xi) dx, \text{ for every real number } \xi.$$

When the independent variable x represents time (with SI unit of seconds), the transform variable ξ represents frequency (in hertz). Under suitable conditions, f can be reconstructed from by the inverse transform:

$$f(x) = \int_{-\infty}^{+\infty} \hat{f}(\xi) \exp(2\pi i x \xi) dx, \text{ for every real number } x.$$

Appendix C

Z-transform

In mathematics, *the Z-transform* converts a discrete time-domain signal, which is a sequence of real or complex numbers, into a complex frequency-domain representation. The Z-transform, like many integral transforms, can be defined as either a one-sided or two-sided transform.

Bilateral Z-transform

The bilateral or two-sided Z-transform of a discrete-time signal $x[n]$ is the function $X(z)$ defined as

$$X(z) = \mathcal{Z}\{x[n]\} = \sum_{n=-\infty}^{\infty} x[n]z^{-n}$$

where n is an integer and z is, in general, a complex number:

$$z = Ae^{j\varphi} = A(\cos \varphi + j \sin \varphi)$$

where A is the magnitude of z , and φ is the complex argument (also referred to as angle or phase) in radians.

Unilateral Z-transform

Alternatively, in cases where $x[n]$ is defined only for $n \geq 0$, the single-sided or unilateral Z-transform is defined as

$$X(z) = \mathcal{Z}\{x[n]\} = \sum_{n=0}^{\infty} x[n]z^{-n}.$$

In signal processing, this definition is used when the signal is causal.

The inverse Z-transform is

$$x[n] = \mathcal{Z}^{-1}\{X(z)\} = \frac{1}{2\pi j} \oint_C X(z)z^{n-1}dz$$

where C is a counterclockwise closed path encircling the origin and entirely in the region of convergence.

Appendix D

Slater-type orbital expansions and expectation values boron

In the one electron theory, the following approximation is made for wave function in general, Ψ :

$$\Psi = \Psi(\vec{r}_1, \vec{r}_2, \vec{r}_3, \dots, \vec{r}_N) = \Psi_1(\vec{r}_1)\Psi_2(\vec{r}_2)\Psi_3(\vec{r}_3)\dots\Psi_N(\vec{r}_N) \quad (D.1)$$

which is a separation ansatz and named "The Hartree Approximation". $\Psi_i(r_i)$ are the one electron wave functions, the orbital functions. In the frame of this approach the one electron functions are

$$\Psi(r) = \sum_j C_j \cdot S_{nl}(\alpha_j, r) \cdot Y_{l,m}(r) \quad (D.2)$$

where l indicates the shell, C_j is the expansion coefficient for the j 'th basis function, m (magnetic quantum number) represents the subspecies of the symmetry n ; $Y(r)$ and $S(\alpha, r)$ are the radial and the angular part of the basis function, respectively. These data was calculated and tabulated for different elements and for different state [145, 146]. For example, the values of these coefficients for atomic and ionic boron are present:

atomic state:

j	S _{nl} (α _j ,r)		C _j	
	nlj	a _j	2s-electron	1s-electron
1	1s	4.445610	-0.194840	0.927050
2	1s	7.917960	-0.012540	0.077800
3	2s	0.867090	0.069410	0.000880
4	2s	1.219240	0.752340	-0.002000
5	2s	2.072640	0.318560	0.004330
6	2s	3.443320	-0.126420	0.002700
j	S _{nl} (α _j ,r)		C _j	
	nlj	a _j	2p-electron	
1	2p	0.874810	0.536220	
2	2p	1.369920	0.403400	
3	2p	2.322620	0.116530	
4	2p	5.594810	0.008210	

Ionic state:

j	S_{nl}(a_j,r)		C_j	
	<i>nlj</i>	<i>a_j</i>	<i>2s-electron</i>	<i>1s-electron</i>
1	1s	4.429940	-0.202880	0.928010
2	1s	7.863360	-0.019420	0.080630
3	2s	1.592410	0.734900	0.003200
4	2s	4.010220	-0.092180	-0.000810
5	2s	1.250210	0.345270	-0.001980

References

- [1] Jackson J.D., *Classical electrodynamics*. 3rd ed., New York: Wiley. (1999)
- [2] Als-Nielsen J. and D. McMorrow, *Elements of modern X-ray physics*. New York: Wiley (2001)
- [3] Chasman R. and Green G.K., *Preliminary design of a dedicated synchrotron radiation facility*. IEEE Trans. Nucl. Sci., NS-22, 1765-1767 (1975).
- [4] Chen L., *Some aspects of the design study on a fourth-generation-like VUV/SXR light source*. J. Elec. Spec. Rel. Phen, 80, 505-508 (1996)
- [5] Poole M.W. and Mc Neil B.W.J., *FEL options for the proposed UK fourth generation light source (4GLS)*. Nucl. Instr. Meth. Phys. Res.A, 507, 489-493 (2003)
- [6] Winick H., *The linac coherent light source (LCLS): A fourth-generation light source using the SLAG linac*. J. Elec. Spec. Rel. Phen, 75, 1-8 (1995)
- [7] Madey J.M.J., *Stimulated emission of bremsstrahlung in a periodic magnetic field*. J. Appl. Phys., 42, 1906 (1971)
- [8] Chattopadhyay S., *Physics of, and science with, the X-ray free-electron laser: 19th Advanced ICFA Beam Dynamics Workshop, Arcidosso, Italy, 10-15 September 2000*, Melville, N.Y.: AIP. (2001)
- [9] Dattoli G., A. Renieri, and A. Torre, *Lectures on the free electron laser theory and related topics*, Singapore; River Edge, NJ: World Scientific., (1993)
- [10] O'Shea P.G. and H.P. Freund, *Laser technology - Free-electron lasers: Status and applications*. Science, 292, 1853-1858 (2001)
- [11] Courant E.D., Pellegrini C., and Zakowicz W., *High-Energy Inverse Free-Electron-Laser Accelerator*. Phys. Rev. A, 32, 2813-2823 (1985)
- [12] *The European X-ray Free-Electron Laser*, in *Technical Design Report DESY*: Hamburg, Germany (2006)
- [13] Ayvazyan V., *et al.*, *First operation of a free-electron laser generating GW power radiation at 32 nm wavelength*. Europ. Phys. J. D, 37, 297-303 (2006)
- [14] Ackermann W, *et al.*, *Operation of a free-electron laser from the extreme ultraviolet to the water window*. Nat. Photon, 1, 336-342 (2007)
- [15] Sorokin A.A., Bobashev S. V., Feigl T., Tiedtke K., Wabnitz H., and Richter M., *Photoelectric effect at ultrahigh intensities*. Phys. Rev. Lett., 99, 213002 (2007)
- [16] *LCLS: First experiments*, in *Technical Design Report SLAC*: Stanford, USA (2000)
- [17] Rice S.O., *Mathematical Analysis of Random Noise*. Bell System Technical Journal, 24, 46-156 (1945)
- [18] Krinsky S. and Yu L.H., *Output Power in Guided Modes for Amplified Spontaneous Emission in a Single-Pass Free-Electron Laser*. Phys. Rev. A, 35, 3406-3423 (1987)
- [19] Saldin E.L., Schneidmiller E.A., and Yurkov M.V., *The Physics of Free-Electron Lasers - an Introduction*. Phys. Rep. Rev. Sect. Phys. Lett., 260, 187-327 (1995)
- [20] Saldin E.L., Schneidmiller E.A., and Yurkov M.V., *A simple method for the determination of the structure of ultrashort relativistic electron bunches*. Nucl. Instr. Meth. Phys. Res. A, 539, 499-526 (2005)

- [21] *SASE FEL at the TESLA Facility, Phase 2*, in *Technical Design Report DESY*. Hamburg, Germany (2006)
- [22] Saldin E.L., Schneidmiller E.A., and Yurkov M.V., *Statistical properties of the radiation from VUVFEL at DESY operating at 30 nm wavelength in the femtosecond regime*. Nucl. Instr. Meth. Phys. Res A, 562, 472-486 (2006)
- [23] Saldin E.L., Schneidmiller E.A., and Yurkov M.V., *Coherence properties of the radiation from X-ray free electron laser*. Optics Communications, 281, 1179-1188 (2008)
- [24] Yu L.H. and S. Krinsky, *Amplified Spontaneous Emission in a Single Pass Free-Electron Laser*. Nucl. Instr. Meth. Phys. Res A, 285, 119-121 (1989)
- [25] Yu L.H. and S. Krinsky, *Analytical theory of intensity fluctuations in SASE*. Nucl. Instr. Meth. Phys. Res A, 407, 261-266 (1998)
- [26] Krinsky S. and Li Y., *Statistical analysis of the chaotic optical field from a self-amplified spontaneous-emission free-electron laser*. Phys. Rev. E, 73, 066501 (2006)
- [27] Rice J.A., *Mathematical statistics and data analysis*. 3rd ed., Belmont, CA: Thomson/Brooks/Cole. (2007)
- [28] Hogg R.V., McKean J.W., and Craig A.T., *Introduction to mathematical statistics*. 6th ed., Upper Saddle River, N.J.: Pearson Education. (2005)
- [29] Goodman J.W., *Statistical optics*, New York: Wiley. (2000)
- [30] Saldin E.L., Schneidmiller E.A., and Yurkov M.V., *FAST: a three-dimensional time-dependent FEL simulation code*. Nucl. Instr. Meth. Phys. Res A, 429, 233-237 (1999)
- [31] Schreiber S., Faatz B., and Honkavaara K., *Operation of FLASH at 6.5nm wavelength*. Proc. EPAC08, Genoa, Italy, (2008)
- [32] Rossbach J., *First lasing below 7 nm wavelength at FLASH/DESY, Hamburg* Proc. FEL08, Gyeongju, Korea, (2008)
- [33] Eilbeck J.C., *Reflection of short pulses in linear optics*. J. Phys. A: Gen. Phys., 5, 1355-1363 (1972)
- [34] Eilbeck J.C. and Bullough R.K., *Method of characteristics in theory of resonant or nonresonant nonlinear optics*. J. Phys. A: Gen. Phys., 5, 820-829 (1972)
- [35] Bullough R.K., Ahmad F., and Eilbeck J.C., *Nonlinear radiation reaction, superradiance, and coherent optical pulse propagation*. IEEE J. Quant. Electr., 8, 568-569 (1972)
- [36] Gase R. and Schubert M., *On the determination of spectral properties of nonstationary radiation*. Optica Acta, 29, 1331-1347 (1982)
- [37] Gase R., *Action of nonstationary linear-systems on the time-dependent spectrum of ultrashort light-pulses*. Optic.& Quant. Electr., 16, 117-123 (1984)
- [38] Dorrer C. and Walmsley I.A., *Concepts for the temporal characterization of short optical pulses*. Eurasip. J. Appl. Sign. Proc., 2005, 1541-1553 (2005)
- [39] Hau-Riege S.P., et al., *Subnanometer-scale measurements of the interaction of ultrafast soft X-ray free-electron-laser pulses with matter*. Phys. Rev. Lett., 98, 145502-4, (2007)
- [40] Hau-Riege S.P., et al., *Soft-x-ray free-electron-laser interaction with materials*. Phys. Rev. E 76, 046403-12 (2007)
- [41] More R.M., *Electronic energy-levels in dense plasmas*. J. Quant. Spectrosc. Radiat. Transfer, 27, 345-357 (1982)

- [42] Page C.H., *Instantaneous power spectra*. J. Appl. Phys., 23, 103-106, (1952)
- [43] Brenner, K.H. and K. Wodkiewicz, *The Time-Dependent Physical Spectrum of Light and the Wigner Distribution Function*. Optics Communications, 43, 103-106 (1982)
- [44] Meyer M., et. al. *Two-color photoionization in xuv free-electron and visible laser fields*, Phys. Rev. A 74, 011401 (2006)
- [45] C. Gahl et al., *A femtosecond X-ray/optical cross-correlator: FLASH X-ray pulse induced transient changes of the optical reflectivity*, Nature Photonics 2, 165-169 (2008)
- [46] Makris, M.G., Lambropoulos P., and Miheli A., *Theory of Multiphoton Multielectron Ionization of Xenon under Strong 93-eV Radiation*. Phys. Rev. Lett., 102, 033002 (2009)
- [47] Rohringer, N. and Santra R., *X-ray nonlinear optical processes using a self-amplified spontaneous emission free-electron laser*. Phys. Rev. A, 76, 033416 (2007)
- [48] Moribayashi, K., et al., *X-ray emission from multi-inner-shell excited states produced by high-intensity short-pulse X-rays*. Laser Phys., 16, 322-324 (2006)
- [49] Rohringer, N. and R. London, *Atomic inner-shell x-ray laser pumped by an x-ray free-electron laser*. Phys. Rev. A, 80, 013809 (2009)
- [50] Nagler, B., et al., *Turning solid aluminium transparent by intense soft X-ray photoionization*. Nature Phys., 5, 693-696 (2009)
- [51] Bergh, M., et al., *Interaction of ultrashort x-ray pulses with B4C, SiC, and Si*. Phys. Rev. E, 77, 026404 (2008)
- [52] Hau-Riege, S.P., et al., *Damage threshold of inorganic solids under free-electron-laser irradiation at 32.5 nm wavelength*. Appl. Phys. Lett., (2007). 90, 173128
- [53] Mantsyzov, B.I., *Laue soliton in a resonantly absorbing photonic crystal*. Opt. Comm., 189, 275-280. (2001)
- [54] Chukhovskii, F.N., Teubner U., and Forster E., *Ultrashort x-ray pulse propagation through resonant attenuating media*. Phys. Rev. B, 55, 3419-3425 (1997)
- [55] Allen, L. and Eberly J.H., *Optical resonance and two-level atoms*. New York: Dover. (1987)
- [56] Scully, M.O. and Zubairy M.S., *Quantum optics*. Cambridge University Press. (1997)
- [57] Rohringer, N. and Santra R., *Resonant Auger effect at high x-ray intensity*. Phys. Rev. A, 77, 053404 (2008)
- [58] Born, M. and E. Wolf, *Principles of optics : electromagnetic theory of propagation, interference and diffraction of light*. 7th expanded ed., Cambridge University Press. (1999)
- [59] Hao Y. and Mittra R., *FDTD modeling of metamaterials: theory and applications*, Norwood, MA: Artech House. (2009)
- [60] Sullivan D.M., *Electromagnetic simulation using the FDTD method*. IEEE Press series on RF and microwave technology. New York: IEEE Press. (2000)
- [61] Yu W., *Electromagnetic simulation techniques based on FDTD method*, Hoboken, Wiley (2009)
- [62] Yee K., *Numerical solution of initial boundary value problems involving Maxwell's equations in isotropic media*. Antennas and Propagation, IEEE Transactions. 14, 302-307 (1966)

- [63] Johnson C., *Numerical solution of partial differential equations by the finite element method*. Mineola, N.Y.: Dover Publications. (2009)
- [64] Meunier G., *The finite element method for electromagnetic modeling*. Hoboken, Wiley (2008)
- [65] Thijssen J.M., *Computational physics*. 2nd ed., Cambridge University Press. (2007)
- [66] Feranchuk I.D., et al., *Description of x-ray reflection and diffraction from periodical multilayers and superlattices by the eigenwave method*. Phys. Rev. B, 68, 235307 (2003)
- [67] Sammar A., et al., *Theoretical and experimental-study of soft X-ray diffraction by a lamellar multilayer amplitude grating*. J. Opt.-Nouv. Rev. D Opt., 24, 37-41 (1993)
- [68] Sammar A. and Andre J.M., *Diffraction of multilayer gratings and zone plates in the X-Ray region using the Born approximation*. J. OSA A, 10, 600-613 (1993)
- [69] Fechtchenko R.M., Vinogradov A.V., and Voronov D.L., *Optical properties of sliced multilayer gratings*. Optics Communications, 2002. 210(3-6): p. 179-186.
- [70] Levashov V.E. and Vinogradov A.V., *Resonance diffraction efficiency enhancement in sliced multilayers*. Appl. Optics, 32, 1130-1135 (1993)
- [71] Levashov V.E., et al., *Sc-Si normal incidence mirrors for a VUV interval of 35-50 nm*. X-Ray Lasers 1998, 159, 593-599 (1999)
- [72] Levashov V.E., et al., *High-Throughput and Resolution Compact Spectrograph for the 124-250 a Range Based on Mosi₂-Si Sliced Multilayer Grating*. Optics Communications, 109, 1-4 (1995)
- [73] Blumenstock G.M. and Keskiuha R.A.M., *Ion-Beam-Deposited Boron-Carbide Coatings for the Extreme-Ultraviolet*. Applied Optics, 33, 5962-5963 (1994)
- [74] Lartigue S. and Male G., *Contribution to the Study of Tetragonal Compounds in the Boron Carbon System*. J. Mat. Sci. Lett., 7, 153-156 (1988)
- [75] Sezer A.O. and Brand J.I., *Chemical vapor deposition of boron carbide*. Materials Science and Engineering B, 79, 191-202 (2001)
- [76] Clark K.H. and Hoard J.L., *The Crystal Structure of Boron Carbide* J. Am. Chem. Soc., 65, 2115 (1943)
- [77] Duncan T.M., *The Distribution of Carbon in Boron-Carbide - a C-13 Nuclear Magnetic-Resonance Study*. J. Am. Chem. Soc., 106, 2270-2275 (1984)
- [78] Kwei G.H. and Morosin B., *Structures of the boron-rich boron carbides from neutron powder diffraction: Implications for the nature of the inter-icosahedral chains*. J. Phys. Chem., 100, 8031-8039 (1996)
- [79] Tallant D.R., et al., *Boron-Carbide Structure by Raman-Spectroscopy*. Phys. Rev. B, 40, 5649-5656 (1989)
- [80] Lee S., et al., *Characterization of Boron-Carbide Thin-Films Fabricated by Plasma Enhanced Chemical Vapor-Deposition from Boranes*. J. Appl. Phys., 72, 4925-4933 (1992)
- [81] Li D. and Ching W.Y., *Fundamental studies on the structures and properties of some B-12-based crystals*. Phys. Rev. B, 52, 17073-17083 (1995)
- [82] Aydin S. and Simsek M., *Hypothetically superhard boron carbide structures with a B11C icosahedron and three-atom chain*. Phys. Stat. Sol. B, 246, 62-70 (2009)
- [83] Werheit H., *Present knowledge of electronic properties and charge transport of icosahedral boron-rich solids*. J. Phys.: Conf. Ser., 176, 012019 (2009)

- [84] Jimenez I., et al., *Photoemission and x-ray-absorption study of boron carbide and its surface thermal stability*. Phys. Rev. B, 57, 13167-13174 (1998)
- [85] Li D., Bancroft G.M., and Fleet M.E., *B K-edge XANES of crystalline and amorphous inorganic materials*. J. Electr. Spectr. Rel. Phen., 79, 71-73 (1996)
- [86] Matkovich V.I., *Boron and refractory borides*. Springer-Verlag. (1977)
- [87] Wells A.F., *Structural inorganic chemistry*. 5th ed., Oxford University (1984)
- [88] Howard I.A., Beckel C.L., and Emin D., *Bipolarons in Boron-Rich Icosahedra - Effects of Carbon Substitution*. Phys. Rev.B, 35, 9265-9270 (1987)
- [89] Aselage T.L. and Tissot R.G., *Lattice-Constants of Boron Carbides*. J. Am. Cer. Soc., 75, 2207-2212 (1992)
- [90] Thevenot F., *Boron carbide-A comprehensive review*. J. Europ. Cer. Soc., 6, 205-225 (1990)
- [91] Konovalikhin S.V. and Ponomarev V.I., *Carbon in Boron Carbide: The Crystal Structure of B₁₁C₃*. Rus. J. Inorg. Chem., 54, 197-203 (2009)
- [92] Bisgaard P., et al., *Measurement of Free-Atom K-Shell Binding-Energies of Light-Elements*. Phys. Scr., 17, 49-52 (1978)
- [93] Caretti I., et al., *Boron carbides formed by coevaporation of B and C atoms: Vapor reactivity, B_xC_{1-x} composition, and bonding structure*. Phys. Rev. B, 77, 174109 (2008)
- [94] Jimenez I., et al., *Soft x-ray emission and absorption study of boron carbides*. (online version of the Advanced Light Source) (1998)
- [95] Shirai K., et al., *Infrared Study of Amorphous B_{1-x}C_x Films*. J. Appl. Phys., 78, 3392-3400 (1995)
- [96] Soufli R., et al., *Optical constants of magnetron-sputtered boron carbide thin films from photoabsorption data in the range 30 to 770 eV*. Applied Optics, 47, 4633-4639 (2008)
- [97] Jia J.J., et al., *Soft x-ray absorption spectroscopy in 100-1000 eV region at the ALS*. J. Electr. Spectr. Rel. Phen., 80, 509-512 (1996)
- [98] Andreev S.S., et al., *Multilayered mirrors based on La/B₄C(B₉C) for X-ray range near anomalous dispersion of boron ($\lambda \approx 6.7$ nm)*. Nucl. Instr. Meth. Phys. Res. A, 603, 80-82 (2009)
- [99] Andreev S.S., et al., *Short-period multilayer X-ray mirrors*. J. Synchrotr. Rad., 10, 358-360 (2003)
- [100] Morawe C., et al., *Design and performance of graded multilayers as focusing elements for x-ray optics*. Rev. Scient. Instr., 70, 3227-3232 (1999)
- [101] Ferrari C., Armani N., and Verdi N., *Thin film composition determination by means of integrated intensity measurements*. J. Phys. D, 38, A143-A146 (2005)
- [102] Fukamachi T., et al., *Measurements of Integrated Intensity near Absorption-Edge with Synchrotron Radiation*. J. Appl. Cryst., 10, 321-324 (1977)
- [103] Bonse U., Hartmannlotsch I., and Lotsch H., *The X-Ray-Interferometer for High-Resolution Measurement of Anomalous Dispersion at Hasylab*. Nucl. Instr. Meth. Phys. Res., 208, 603-604 (1983)
- [104] Raunio G. and Svensson O., *X-Ray Total Reflection Studies of Germanium Gold and Glass by Means of a 3-Crystal Spectrometer*. Arkiv for Fysik, 35, 149 (1968)

- [105] Martens G. and Rabe P., *EXAFS Studies on Superficial Regions by Means of Total Reflection*. Phys. Stat. Sol. A, 58, 415-424 (1980)
- [106] Mertins H.C., et al., *Soft X-ray magneto-optical constants at the Fe 2p edge determined by Bragg scattering and Faraday effect*. J. Magnet. Magnetic Mat., 240, 451-453 (2002)
- [107] Mertins H.C., Schafers F., and Gaupp A., *Soft-X-ray magneto-optical Faraday effect on Fe and Co films*. Europhysics Letters, 55, 125-131 (2001)
- [108] Kunes J., et al., *X-ray Faraday effect at the L-2,L-3 edges of Fe, Co, and Ni: Theory and experiment*. Phys. Rev. B, 6417, 174417 (2001)
- [109] Chen K., et al., *Soft X-ray magneto-optical faraday effect around Ni M-2,M-3 edges*. Chin. Phys. Lett., 25, 1110-1112 (2008)
- [110] Yamamoto Y., et al., *High-sensitive measurement of uranium L-III-edge X-ray absorption near-edge structure (XANES) for the determination of the oxidation states of uranium in crustal materials*. Appl. Geochem., 23, 2452-2461 (2008)
- [111] Chen K., Cui M.Q., and Zheng L., *Transmission measurement of photo-absorption cross section of aluminum in soft X-ray region of 50 to 250 eV*. Chin. Phys. C, 32, 673-676 (2008)
- [112] Chantler C.T., *Development and applications of accurate measurement of X-ray absorption The X-ray extended range technique for high accuracy absolute XAFS by transmission and fluorescence*. Europ. Phys. J.-Spec. Top., 169, 147-153 (2009)
- [113] Muramatsu Y., et al., *Total-electron-yield X-ray standing-wave measurements of multilayer X-ray mirrors for interface structure evaluation*. Jap. J. Appl. Phys. I, 41, 4250-4252 (2002)
- [114] Ejima T., Harada T., and Yarnazaki A., *Phase change observation in reflection multilayers by total electron yield and reflection spectra*. Appl. Phys. Lett., 89, 021914 (2006)
- [115] Brizard C., Pizzini S., and Regnard J.R., *Total Electron Yield Exafs Studies of (001) Au/Co Monocrystalline Multilayers*. Solid State Communications, 90, 147-149 (1994)
- [116] Seve L., Tonnerre J.M., and Raoux D., *Determination of the anomalous scattering factors in the soft-X-ray range using diffraction from a multilayer*. J. Appl. Cryst., 31, 700-707 (1998)
- [117] Spiller E., *Refractive-Index of Amorphous-Carbon near Its K-Edge*. Appl. Opt., 29, 19-23 (1990)
- [118] Henke B.L., Gullikson E.M., and Davis J.C., *X-Ray Interactions - Photoabsorption, Scattering, Transmission and Reflection at E=50-30,000 Ev, Z=1-92 (Vol 54, Pg 181, 1993)*. At. Data and Nucl. Data Tabs., 55, 349-349 (1993)
- [119] Rosenbluth A.E. and Lee P., *Bragg Condition in Absorbing X-Ray Multilayers*. Appl. Phys. Lett., 40, 466-468 (1982)
- [120] Vinogradov A.V. and Zeldovich B.Y., *Multilayer Mirrors for X-Ray and Far UV Radiation*. Optics and Spectroscopy (Rus), 42, 709-714 (1977)
- [121] Vinogradov A.V. and Zeldovich B.Y., *X-Ray and Far UV Multilayer Mirrors - Principles and Possibilities*. Appl. Opt., 16, 89-93 (1977)
- [122] Braun C., *Parratt32 program for reflectivity analysis*. HMI Berlin (1997)
- [123] Windt D.L., *IMD - Software for modeling the optical properties of multilayer films*. Computers in Physics, 12, 360-370 (1998)

- [124] *Center for X-Ray Optics*. <http://www-cxro.lbl.gov>
- [125] Borel C., et al. *Reflectivity and stress responses of multilayers upon isothermal treatment*. in *Advances in X-Ray/EUV Optics, Components, and Applications*. San Diego, USA: SPIE (2006)
- [126] Borel C., et al. *In situ study of multilayer reflectivity upon heat treatment under synchrotron radiation*. in *Laser-Generated, Synchrotron, and Other Laboratory X-Ray and EUV Sources, Optics, and Applications II*. San Diego, USA: SPIE (2005)
- [127] Andre J.M., et al., *La/B4C small period multilayer interferential mirror for the analysis of boron*. X-Ray Spectrometry, 34, 203-206 (2005)
- [128] Sobczak', E. and Persy K., *XPS, SXS and Isochromat Investigations of Electronic Structures of Evaporated Boron*. Physica Scripta, 22, 88-90 (1980)
- [129] Walton C.C. and J.B. Kortright, *Evolution of Boron K Near Edge Structure in Ultra-Short Period W/B4C Multilayers: Differences in Transmission and Photocurrent Measurements*. (online version from <http://www-als.lbl.gov/als/compendium/AbstractManager/uploads/Evolution.pdf>)
- [130] Bearden J.A., *X-Ray Wavelengths*. Rev. Mod. Phys., 39, 78-124 (1967)
- [131] Ksenzov D., Grigorian S., and Pietsch U., *Time-space transformation of femtosecond free-electron laser pulses by periodical multilayers*. J Synchr. Rad., 15, 19-25 (2008)
- [132] Ksenzov D., et al., *Reflection of femtosecond pulses from soft X-ray free-electron laser by periodical multilayers*. Phys. Stat. Sol. A, 206, 1875-1879 (2009)
- [133] Baker C.T.H., et al., *Numerical-Solution of Fredholm Integral-Equations of First Kind*. Computer Journal, 7, 141 (1964)
- [134] Tikhonov A.N. and Arsenin V.I.A., *Solutions of ill-posed problems*. Winston (1977);
- [135] Cromer D.T. and Liberman D., *Relativistic Calculation of Anomalous Scattering Factors for X-Rays*. J. Chem. Phys., 53, 1891 (1970)
- [136] Froese Fischer C., *The Hartree-Fock method for atoms: a numerical approach*, Wiley (1977)
- [137] Roothaan C.C.J., *Self-Consistent Field Theory for Open Shells of Electronic Systems*. Rev. Modern Phys., 32, 179-185 (1960)
- [138] Roothaan C.C.J. and Detrich J.H., *General Quadratically Convergent Multiconfiguration Self-Consistent-Field Theory in Terms of Reduced Matrix-Elements*. Phys. Rev. A, 27, 29-56 (1983)
- [139] Roothaan C.C.J. and Weiss A.W., *Correlated Orbitals for the Ground State of Heliumlike Systems*. Rev. Modern Phys., 32, 194-205 (1960)
- [140] Roetti C. and Clementi E., *Simple Basis Sets for Molecular Wavefunctions Containing Atoms from Z=2 to Z=54*. J. Chem. Physics, 1974. 60(12): p. 4725-4729.
- [141] Roetti C. and Clementi E., *Analytical Hartree-Fock Wavefunctions for Neutral Atoms from Helium to Xenon*. J. Chem. Physics, 60, 3342-3342 (1974)
- [142] Bunge C.F., Barrientos J.A., and Bunge A.V., *Roothaan-Hartree-Fock Ground-State Atomic Wave-Functions - Slater-Type Orbital Expansions and Expectation Values for Z=2-54*. At. Data and Nucl. Data Tabs, 53, 113-162 (1993)
- [143] Delavega J.M.G. and Miguel B., *Roothaan-Hartree-Fock Momentum Expectation Values for Heavy-Elements (Z=55-92)*. At. Data and Nucl. Data Tabs, 58, 307-315 (1994)

- [144] Zhou B., Kissel L., and Pratt R.H., *Simple Computational Schemes for X-Ray Anomalous Scattering Factors for Ions*. Nucl. Instrum. Meth. Phys. Res. B, 66, 307-312 (1992)
- [145] Koga T., et al., *Roothaan-Hartree-Fock Wave-Functions for Ions with N-Less-Than-or-Equal-to-54*. J. Phys. B, 26, 2529-2532 (1993)
- [146] Koga T., Tatewaki H., and Thakkar A.J., *Roothaan-Hartree-Fock Wave-Functions for Atoms with Z-Less-Than-or-Equal-to-54*. Phys. Rev. A, 47, 4510-4512 (1993)
- [147] Ksenzov, D., Panzner T., Schlemper C., Morawe C., and Pietsch U., *The optical properties of boron carbide near boron K-edge evaluated by soft x-ray reflectometry from Ru/B₄C multilayer*. Appl. Opt., 35, 6684-6691 (2009)

List of Publications

Interaction of X-ray radiation with periodical multilayer structures

1. D. Ksenzov, S. Grigorian and U. Pietsch. *Time-space transformation of femtosecond free-electron laser pulses by periodical multilayers*. J. Synchrotron Rad. 15, 19-25 (2008)
2. D. Ksenzov, S. Grigorian, S. Hendel, F. Bienert, M.D. Sacher, U. Heinzmann and U. Pietsch. *Reflection of femtosecond pulses from soft X-ray free-electron laser by periodical multilayers*. Physica Status Solidi A 206, 1875 (2009)
3. D. Ksenzov, T. Panzner, C. Schlemper, C. Morawe, and U. Pietsch. *Optical properties of boron carbide near the boron K edge evaluated by soft-x-ray reflectometry from a Ru/B4C multilayer*. Applied Optics, 48, 6684-6691 (2009)

The other publication:

1. Ksenzov, D.A. and E.P. Petrov, *Photonic crystals for soft x-ray*. Proc. SPIE, 2001. 4242: p. 243.
2. E.P. Petrov, D.A. Ksenzov, T.A. Pavich, M.A. Samoilovich, and A.V. Gur'yanov, *Time-resolved luminescence of europium complexes in bulk and nanostructured dielectric media*, in: Physics, Chemistry and Application of Nanostructures, V.E. Borisenko, S.V. Gaponenko, and V.S. Gurin, Eds., World Scientific, Singapore, 2003, pp. 43-46.

Acknowledgements

During the last few years I have met many people who helped me to work on my thesis. And I would like to acknowledge them for their support during my time in Siegen.

I would like to thank

- my research advisor Prof. Dr. Ullrich Pietsch for his continuous guidance and support during the four years I have spent in his group. I appreciate the always open door and numerous, long, vivid discussions which provided not only clear insight into physical processes, but also advice for the organized work. There is still a long way to reach the latter, but the light at the end of the tunnel is bright and I would like to thank him for the patience.
- Dr. Souren Grigorian for the actual discussions of main and ancillary questions and especially for deep handling into problem during my research work. Also I am grateful for spending time together during poster sections.
- Dr. Stefan Hendel, Dr. Tobias Panzner and Christoph Schlemper for participation in the measurements at BESSY II.
- Dr. Fred Senf and Dr. Franz Schäfers from the Optics Beamline (BESSY) for their experimental assistance and BESSY for the beam time.
- Dr. Christian Morawe from the X-ray Optics Group (ESRF) for design and fabrication of the multilayer structures based on B₄C materials.
- The special thanks are to all present and former members of solid state physics group of Prof. Dr. Ullrich Pietsch for the nice atmosphere in the group. Dr. Semen Gorfman is especially acknowledged for adaptation to life in Siegen.

In the end I would like to thank all my family for all of their support and for their ability to keep everything in perspective. I am grateful to my wife for her patience and her absolutely necessary language corrections, and my four-years old son, who did not delete the electronic version of my thesis during his exploration of laptop facilities.

Curriculum vitae:

Eidesstattliche Erklärung

Ich versichere hiermit an Eides statt, dass ich die vorliegende Arbeit ohne fremde Hilfe und ohne benutzung anderer als der angegebenen Hilfsmittel angefertigt habe. Alle Ausführungen, die wortlich oder singemäß aus fremden Quellen übernommen wurden sind als solche gekennzeichnet. Dier Arbeit wurde bisher in gleicher oder ähnlicher Form noch keiner anderen Jury vorgelegt und wird noch nicht komerziell genutzt.

Ich bin bewusst dass eine falsche Erklärung den Ausschluss aus dem Wettbewerb zur Folge haben wird.

Siegen,
Ort/Datum

Unterschrift